

DISS. ETH NO. 21978

Search for Physics Beyond the Standard Model in the Opposite-Sign Same-Flavor Dilepton Final State with the CMS Detector

A thesis submitted to attain the degree of

Doctor of Sciences

(Dr. sc. ETH Zurich)

presented by

Marco – Andrea Buchmann

MSc ETH Zurich Physics

born June 1st, 1985

citizen of Emmen LU and Inwil LU, Switzerland
and Montechiarugolo (PR), Italy

accepted on the recommendation of

Prof. Dr. Rainer Steffen Wallny	examiner
Prof. Dr. Günther Dissertori	co-examiner

2014

Abstract

The Standard Model of particle physics has been remarkably successful in describing results of generations of collider and fixed-target experiments. Despite the model's success, many open questions remain; an extension will be necessary at the very least at the Planck scale, where quantum gravity must be incorporated into the theory. An excellent candidate for a possible extension of the Standard Model is supersymmetry, which predicts a partner particle for each particle of the Standard Model and solves several of the shortcomings of the Standard Model.

In this thesis, a search for supersymmetry in the final state with two opposite-sign same-flavor leptons, jets, and missing transverse energy is presented. This final state is very common in scenarios of physics beyond the Standard Model, and many models contain decay chains producing correlated lepton pairs and therefore feature a kinematic edge in the dilepton mass distribution. The present search uses 19.4 fb^{-1} of integrated luminosity of proton-proton collisions at a center-of-mass energy of $\sqrt{s} = 8 \text{ TeV}$, collected by the Compact Muon Solenoid detector at CERN's Large Hadron Collider. Two different approaches are used: a counting experiment at low invariant dilepton mass to detect a generic same-flavor signal, and a fit in a broader dilepton mass range to find a kinematic edge. The search is performed separately for central leptons (i.e. lepton pairs where both leptons are in the barrel region) and non-central leptons (where at least one of the leptons is outside the barrel region). The dominating background consists of flavor symmetric processes, i.e. processes which produce same-flavor and opposite-flavor lepton pairs with equal probability. Smaller contributions arise from $Z + \text{jets}$ events, non-prompt leptons, and rare backgrounds. The backgrounds are predicted using data

control samples, with each main background being determined by various independent methods.

A 2.5σ excess over the Standard Model expectations was found for central lepton pairs (0.2σ for non-central lepton pairs) in the counting experiment. In the case of the fit, a mass edge position of 78.7 ± 1.4 GeV was found, and the significance was determined to be 2.96σ . The results were used to establish exclusion limits on the number of signal events in a model-independent way.

Zusammenfassung

Das Standardmodell der Teilchenphysik ist ausserordentlich erfolgreich in der Beschreibung experimenteller Resultate von Generationen von Collider- und Fixed-Target-Experimenten. Es verbleiben allerdings mehrere offene Fragen und das Modell wird mindestens an der Planckskala erweitert werden müssen, da bei diesen Energien die Quantengravitation in die Theorie einbezogen werden muss. Ein hervorragender Kandidat für eine solche Erweiterung des Standardmodells ist die Supersymmetrie, welche einen sogenannten Superpartner für jedes Teilchen des Standardmodells vorhersagt und verschiedene Mängel behebt.

In dieser Dissertation wird eine Suche nach Supersymmetrie im Endzustand mit zwei Leptonen gegensätzlichen Vorzeichens und gleichen Flavors, Jets sowie fehlender transversaler Energie vorgestellt. Es handelt sich dabei um einen sehr häufigen Endzustand in Modellen jenseits des Standardmodells, wobei viele dieser Modelle Zerfallsketten mit korrelierten Leptonenpaaren enthalten (welche eine kinematische Kante im Leptonenpaarmassenspektrum verursachen).

Die präsentierte Suche verwendet einen Datensatz mit 19.4 fb^{-1} integrierter Luminosität, welcher vom Compact Muon Solenoid Detektor am Large Hadron Collider des CERN bei einer Schwerpunktenenergie von $\sqrt{s} = 8 \text{ TeV}$ in Proton-Proton Kollisionen aufgezeichnet wurde. Zwei verschiedene Ansätze werden verwendet: ein Zählexperiment bei niedriger Leptonenpaarmasse um ein allgemeines Signal in diesem Endzustand zu finden, sowie ein Fit in einem breiteren Bereich der Leptonenpaarmasse zum Auffinden einer kinematischen Kante. Die Suche wird separat ausgeführt für zentrale Leptonenpaare (bei welchen beide Leptonen in der

Barrelregion sind) und nicht-zentrale Leptonenpaare (bei welchen sich mindestens ein Lepton ausserhalb der Barrelregion befindet). Der grösste Untergrundbeitrag kommt von Flavor-symmetrischen Prozessen; dies sind Prozesse, welche Leptonenpaare gleichen und ungleichen Flavors mit identischer Wahrscheinlichkeit produzieren. Kleinere Beiträge stammen von $Z + \text{jets}$ Ereignissen, nicht-prompten Leptonen sowie seltenen Untergrundprozessen. Diese Untergrundprozesse werden durch Verwendung von statistisch unabhängigen Kontrollregionen vorhergesagt, wobei jeder Untergrund anhand mehrerer unabhängigen Methoden bestimmt wird.

Für zentrale Leptonenpaare wurde eine Abweichung von 2.5σ gegenüber der Standardmodellvorhersage gefunden (0.2σ für nicht-zentrale Leptonenpaare). Im Falle des Fits wurde eine Kantenposition von $78.7 \pm 1.4 \text{ GeV}$ gefunden, wobei die Signifikanz 2.96σ beträgt. Die Resultate wurden verwendet um obere Grenzen für die Anzahl Signalereignisse in einer modellunabhängigen Weise zu berechnen.

Acknowledgments

I would like to thank all those who have contributed in one way or another to this analysis.

First and foremost I'd like to thank my supervisor, Rainer Wallny, for offering me the great opportunity to work on such a fascinating analysis and in such an amazing team. I am also very thankful for Günther Dissertori's support and leadership concerning CMS management decisions.

I'd also like to thank the JZB team leader, Frédéric Ronga, for his leadership, his detailed feedback, and for his patience in answering an uncountable number of questions. The analysis would definitely not have been the same without him and his many contributions.

I'm also deeply indebted to Konstantinos Theofilatos (or Kostas for short) for his many ideas and inputs and the many fruitful discussions. He was the one who got the JZB ball rolling with his thesis and he has continued to provide invaluable input to the analysis. I particularly enjoyed his fiery speeches and the energy with which he defended his position, no matter the adversaries, which sometimes landed him in very hot water.

Last but by no means least, I'd like to thank Pablo Martínez Ruiz del Árbol for his countless contributions and his encouraging feedback as well as the many, many, many useful discussions we had - working with him has been a privilege and a pleasure. His perseverance and dedication are truly one of a kind, and he has

become a dear friend of mine, and the best man at my wedding.

Furthermore, I'd also like to express my appreciation to all the unsung heroes at CERN, all the great minds behind the CMS detector and the LHC, and all those that have contributed in one way or another on the long way which starts with Hydrogen atoms and ends with a dilepton mass distribution.

I am also indebted to all the people outside the experiment who have helped me in so many different ways. This thesis would definitely not have been possible without the unwavering support from my family, particularly my parents, who have not only provided me with tons of snacks, but have always been an enormous source of inspiration and have always been there for me – I would not be where I am and who I am today without them.

A special "thank you" also goes to my incredible wife who has also always been there for me and even contributed to the analysis with her keen eye and sense of style. She has been my personal cheerleader, sharing not only joyous moments but also putting up with my occasional rants and frustration. I consider myself incredibly lucky to have found her, my personal 5σ discovery!

I am very much looking forward to future results from the LHC and particularly CMS, and hope that supersymmetry is around the corner probed by LHC's Run II.

Contents

1	Introduction	1
2	Theoretical Foundations	3
2.1	The Standard Model	3
2.2	Shortcomings of the Standard Model	6
2.3	The Supersymmetric Extension of the Standard Model	8
2.3.1	Implications of the MSSM	10
2.3.2	The Phenomenological Minimal Supersymmetric Standard Model (pMSSM)	10
2.3.3	Simplified Models of Supersymmetry (SMS)	12
2.4	Particle Production and Decay	13
2.4.1	The Dilepton Final State	14
3	Experimental Apparatus	19
3.1	The Large Hadron Collider (LHC)	20
3.2	The Compact Muon Solenoid (CMS)	22
3.2.1	The CMS Coordinate System	24
3.2.2	Inner Tracking Detectors	24
3.2.3	Electromagnetic Calorimeter	26
3.2.4	Hadronic Calorimeter	27
3.2.5	Muon System	28
3.2.6	Magnet	30
3.2.7	Trigger and Data Acquisition Systems	30

3.2.8	Software and Computing	31
4	Reconstruction	33
4.1	The Particle Flow Algorithm	33
4.2	Muon Reconstruction and Identification	35
4.3	Electron Reconstruction and Identification	36
4.4	Tau Reconstruction and Identification	37
4.5	Photon Reconstruction and Identification	37
4.6	Jet Reconstruction and Identification	38
4.6.1	Jet Energy Corrections	39
4.7	Missing Transverse Energy Reconstruction	42
4.8	Pile-Up	44
4.8.1	Jet Area Correction	45
4.8.2	Effective Area Correction	46
4.8.3	Pile-Up Correction for Muons	47
5	Search for Physics Beyond the Standard Model in the Opposite-Sign Same-Flavor Dilepton Final State	49
5.1	Samples and Event Selection	51
5.1.1	Event Preselection	51
5.1.2	Data Sample	52
5.1.3	Simulated Events	54
5.2	Signal and Control Regions	56
5.3	Background Estimation	59
5.3.1	Overview	59
5.3.2	Flavor Symmetric Backgrounds	59
5.3.3	SM Z + jets	75
5.3.4	Fake Leptons	96
5.3.5	Rare Backgrounds	101
5.3.6	Summary of Backgrounds	103
5.4	Kinematic Edge Fit	104
5.4.1	Background Model	104
5.4.2	Procedure	111
5.4.3	Application to Monte Carlo Simulation	116
5.4.4	Comparison with Previous Searches for a Kinematic Edge	122
5.5	Results	123
5.5.1	Counting Experiment	123
5.5.2	Search for a Kinematic Edge	124
5.6	Interpretation	128
5.6.1	Limit Setting Procedure	128
5.6.2	Limit Calculation Results	130

6 Summary and Conclusions	133
List of Figures	137
List of Tables	145
References	149

1

Introduction

The search for the description of the most fundamental building blocks of the universe and their interactions started over 2000 years ago with the Greek philosopher Democritus hypothesizing that there exist a number of smallest, indivisible building blocks of matter. The picture of these building blocks has changed significantly over the past two millennia and has culminated in the 20th century in the so-called “Standard Model” of particle physics. The Standard Model has been remarkably successful in accurately predicting experimental results from generations of accelerator experiments, most recently the Large Hadron Collider (LHC) at the European Organization for Nuclear Research (CERN), which has observed a new boson [1, 2] consistent with the last missing particle predicted by the Standard Model—the Higgs boson.

Many open questions remain despite the Standard Model’s success: astrophysical and cosmological observations provide strong evidence for the existence of a “dark matter” particle [3–5], for which the Standard Model does not provide any viable candidate. Furthermore, the mass of the Higgs boson is very sensitive to any physics beyond the Standard Model. Additionally, the Standard Model does not explain the non-zero neutrino masses necessary to explain neutrino oscillations, and does not allow for gauge coupling unification. An extension will be necessary, at the very latest, at the Planck scale ($\Lambda_{\text{Planck}} \approx 10^{19}$ GeV), where quantum gravitational effects become important; the Standard Model can therefore only be a low

energy approximation to a more fundamental theory.

Many extensions have been proposed to address the shortcomings of the Standard Model; one of the most promising extensions consists of including an additional symmetry, the so-called “supersymmetry” (or SUSY for short), which relates bosons and fermions. For every particle of the Standard Model there exists a “supersymmetric partner”, differing in half a unit in spin but otherwise sharing the same quantum numbers. These additional particles do not only provide a solution to the Higgs mass problem but they may also provide a dark matter candidate. Furthermore, they open the door to gauge coupling unification at very high energies in the so-called Grand Unified Theory (GUT). If the symmetry is broken at energies beyond those currently probed by experiment, the supersymmetric particles would be much heavier than their Standard Model counterparts, explaining their elusiveness. The advantages of the extension, however, could still hold.

In this thesis, a search for physics beyond the Standard Model in the final state with two opposite-sign same-flavor leptons, jets, and missing transverse energy is presented; the search uses 19.4 fb^{-1} of collision data collected by the Compact Muon Solenoid detector [6]. The final state is very common in physics beyond the Standard Model scenarios, such as supersymmetry. Two different approaches are taken to search for a generic opposite-sign same-flavor dilepton signal as well as specifically for models containing a kinematic dilepton mass edge.

The thesis is structured as follows: a short summary of the Standard Model as well as the supersymmetric extension to the Standard Model is presented in Chapter 2. Chapter 3 describes the experimental apparatus of the Large Hadron Collider and the Compact Muon Solenoid (CMS) detector at CERN, while the reconstruction of physics objects within CMS is described in Chapter 4. In Chapter 5, a search for supersymmetry in pp collisions with the CMS detector is presented. The contents of the thesis are summarized in Chapter 6.

2

Theoretical Foundations

2.1 The Standard Model

The Standard Model of particle physics is a remarkably successful theory describing the constituents of the universe and their interactions. The particles of the Standard Model can be divided into two groups: fermions with half-integer spin, and bosons with integer spin, the former being the constituents of matter and the latter (in the case of the gauge bosons) acting as force carriers.

Each particle has an antiparticle (denoted with a bar on the symbol) which is identical to its partner particle except for its charge, which is opposite.

Fermions

Fermions, named after Italian physicist Enrico Fermi, can be subdivided into quarks and leptons, each having three different “generations” that contain doublets of particles sharing similar properties. Quarks and leptons mainly differ in their electric charge and in their interactions: quarks have fractional electric charge (in units of e), and interact not only weakly and electromagnetically, but also strongly. Each quark generation consists of one “up type” quark (with charge $+\frac{2}{3}$) and one “down type” quark (with charge $-\frac{1}{3}$). Leptons on the other hand do not interact strongly and have integer electric charge (in units of e); each lepton generation consists of

Table 2.1: Electric charges (in units of e) and masses (in MeV) of the fermions [7].

Quarks (spin: $s=\frac{1}{2}$)				
	first generation	second generation	third generation	interaction
particle	up (u)	charm (c)	top (t)	strong, EM weak
charge	$+\frac{2}{3}$	$+\frac{2}{3}$	$+\frac{2}{3}$	
mass	$2.3^{+0.7}_{-0.5}$	$(1.275 \pm 0.025) \cdot 10^3$	$(173.5 \pm 0.6 \pm 0.8) \cdot 10^3$	
particle	down (d)	strange (s)	bottom (b)	
charge	$-\frac{1}{3}$	$-\frac{1}{3}$	$-\frac{1}{3}$	
mass	$4.8^{+0.7}_{-0.3}$	95 ± 5	$(4.18 \pm 0.03) \cdot 10^3$	

Leptons (spin: $s=\frac{1}{2}$)				
	first generation	second generation	third generation	interaction
particle	e-neutrino (ν_e)	μ-neutrino (ν_μ)	τ-neutrino (ν_τ)	weak
charge	0	0	0	
mass	$< 2 \cdot 10^{-6}$	< 0.19	< 18.2	
particle	electron (e)	muon (μ)	tau (τ)	EM, weak
charge	-1	-1	-1	
mass	0.511	105.658	1776.82 ± 0.16	

one particle with charge -1 and a neutral particle, which, due to the lack of electric charge, only interacts weakly.

The fermionic particle content of the Standard Model is summarized in Tab. 2.1.

Bosons

Bosons (with spin 1), named after Indian physicist Satyendra Nath Bose, are the quanta of gauge fields. They mediate the electromagnetic, weak, and strong interactions between particles:

- (i) The electromagnetic interaction has infinite range; it is mediated by the massless photon, which couples to electromagnetic charge. Atoms and molecules, for example, are held together by the electromagnetic force.
- (ii) The weak interaction is mediated by the massive W and Z bosons. Due to the large mass of the mediating particles, the range of the weak nuclear interaction

Table 2.2: Electric charges (in units of e) and masses of the gauge bosons [7].

Gauge bosons (spin = 1)					
Symbol	Charge	Mass (GeV)	Force	Coupling	Range [m]
photon, γ	0	0	EM	$\alpha \approx 10^{-2}$	∞
W^\pm	± 1	80.385 ± 0.015	Weak	$G_F \approx 10^{-5}$	10^{-18}
Z	0	91.1876 ± 0.0021			
gluon, g	0	0	Strong	$\alpha_s \approx 1$	10^{-15}

is very short ($\sim 10^{-18}$ m). The weak interaction is responsible for the β decay (a nuclear decay).

- (iii) The gluons are the mediating particles of the strong force, and couple to the so-called color quantum number. A peculiarity of the strong force lies in its coupling strength, which decreases with increasing energy (“asymptotic freedom”) and therefore becomes small for short-distance interactions. The strong force also leads to increasing binding energy between a separating quark-antiquark pair until sufficient potential energy is attained to produce another quark-antiquark pair. More pairs are produced until their kinetic energy has degraded, leaving a collection of particles moving in approximately the same direction (a so-called “jet”).
- (iv) Gravity does not play an important role at the particle level and is not part of the Standard Model; its coupling strength is significantly smaller than that of the strong force (by a factor of approximately 10^{-39}), and therefore negligible at typical collider energies. Quantum gravity effects only become strong at the Planck scale ($\Lambda_{\text{Planck}} \sim 10^{19}$ GeV).

The gauge bosons of the Standard Model, along with their electric charge and mass, are summarized in Tab. 2.2.

Quarks are subject to all three forces, strong, weak, and electromagnetic, whereas leptons do not have a color charge and therefore only interact weakly and electromagnetically. The neutrinos do not have an electric charge and therefore only interact weakly.

The weak and electromagnetic interactions can be unified; the resulting gauge bosons of the electroweak interaction are three W bosons (W^0, W^1 , and W^2) and the B^0 boson. These gauge bosons, however, are massless and not physically observable. By breaking the electroweak symmetry, the B^0 and W^0 mix via the

weak angle (Weinberg angle) to form the previously mentioned γ and Z bosons,

$$\begin{pmatrix} \gamma \\ Z \end{pmatrix} = \begin{pmatrix} \cos \theta_W & \sin \theta_W \\ -\sin \theta_W & \cos \theta_W \end{pmatrix} \begin{pmatrix} B^0 \\ W^0 \end{pmatrix}, \quad (2.1)$$

and the W^\pm are superpositions of the W^1 and W^2 bosons. The electroweak symmetry breaking does not only lead to the W^\pm and Z bosons acquiring mass, but it also leads to an additional particle in the Standard Model, the Higgs boson. This additional particle was the last missing particle of the Standard Model. In 2012, the CMS [1] and ATLAS [2] collaborations at the LHC reported the discovery of a boson with properties consistent with those of the Standard Model Higgs boson, completing the Standard Model's particle spectrum.

2.2 Shortcomings of the Standard Model

Despite its striking success, the Standard Model of particle physics will have to be extended at the latest at energies around the Planck scale ($\Lambda_P \approx 10^{19}$ GeV), where gravity is expected to become comparable to other forces and therefore needs to be incorporated into the theory. The particles discovered thus far range in mass from about an eV to more than a hundred GeV; it seems intuitive that particles are not restricted to these eleven orders of magnitude but that there are more particles in the eight orders beyond. In fact, several experimental measurements today already provide powerful clues as to what lies ahead as the frontiers of high energy physics are pushed even further:

Dark Matter in the Universe

Astrophysical and cosmological measurements have provided clear evidence [3–5] that there is additional matter, referred to as “dark matter”, and that this matter is corpuscular in nature. In fact, baryonic matter accounts only for about 4% of the mass-energy in the universe, whereas non-luminous, non-baryonic matter makes up approximately 23% [8]. Dark matter would most likely [9, 10] require a weakly interacting, massive particle (WIMP), which does not exist in the Standard Model, indicating the need for the Standard Model to be extended.

Neutrino Masses

The Standard Model also fails to explain the oscillations observed between neutrinos, which imply non-zero mass of at least two neutrinos, in direct contradiction to the Standard Model (where neutrinos have zero mass). While the mass must be very small (see Tab. 2.1), the neutrino masses cannot be degenerate as the oscillation frequency is proportional to the mass difference.

Gauge Couplings

The gauge couplings can be evolved to very high energies based on the current highly precise measurements at lower energies. In the framework of the Standard Model, the gauge couplings do not meet at the same point and a unification is therefore not possible.

Higgs Mass

The Higgs boson does not only complete the Standard Model, it also opens the door to physics beyond the Standard Model by being highly sensitive to any contribution from new particles (this sensitivity is related to the “hierarchy problem”). The contributions at one-loop level are shown in Fig. 2.1. For a Higgs field coupling to a fermion via $-\lambda_f H \bar{f} f$ (Yukawa coupling), the correction is

$$\Delta m_H^2 = -\frac{|\lambda_f|^2}{8\pi^2} \Lambda_{UV}^2 + \dots, \quad (2.2)$$

where Λ_{UV} is an ultraviolet momentum cutoff to regulate the loop integral. The largest contribution comes from the top quark, for which $\lambda_f \approx 1$. If the momentum cutoff is on the order of Λ_{Planck} , the correction would be some 30 orders of magnitude larger than the required value of m_H . The introduction of a heavy complex scalar particle S with mass m_S , coupling with a term $-\lambda_S |S|^2 |H|^2$, leads to a correction due to the diagram shown in Fig. 2.1b of

$$\Delta m_H^2 = \frac{\lambda_S}{16\pi^2} [\Lambda_{UV}^2 - 2m_S^2 \ln(\Lambda_{UV}/m_S) + \dots], \quad (2.3)$$

which has an opposite sign with respect to the correction from fermionic contributions. The fermionic and bosonic corrections are very different in the Standard Model, leading to a large total correction. A comparison of the two correction terms directly leads to the idea of relating fermions and bosons: if a theory provides two complex scalars for each fermion, and $\lambda_S = |\lambda_f|^2$, then the corrections proportional to Λ_{Planck}^2 cancel; such a theory is introduced in the next Section.

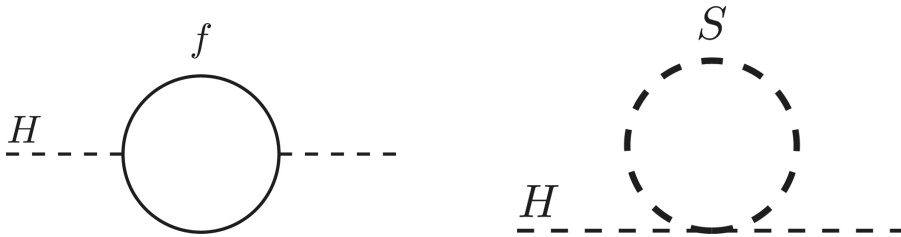


Figure 2.1: One-loop quantum corrections to the Higgs squared mass parameter m_H^2 , due to (a) a Dirac fermion f , and (b) a scalar S . [11]

2.3 The Supersymmetric Extension of the Standard Model

Supersymmetry is an extension of the Standard Model which postulates a relation between fermionic and bosonic states through an operator Q ,

$$Q|\text{Boson}\rangle = |\text{Fermion}\rangle, \quad Q|\text{Fermion}\rangle = |\text{Boson}\rangle. \quad (2.4)$$

In its simplest form, supersymmetry doubles the particle spectrum, with the new superpartners having a spin difference of half a unit with respect to their Standard Model counterparts, but sharing all other quantum numbers. At the time of writing, no supersymmetric particles have been discovered, which implies that the Standard Model particles and their superpartners must have different masses, and the symmetry must therefore be broken.

The supersymmetric partners are commonly referred to as sparticles, with the supersymmetric partners of the fermions being prefixed an *s* (stemming from the word “scalar”, hinting at the scalar nature of the superpartners), such as squarks and sleptons. The supersymmetric partners of Standard Model gauge bosons, referred to as gauginos, carry the suffix “ino”. All supersymmetric partners use their Standard Model partner’s symbol, and a tilde is added to distinguish them (for instance, the smuon’s symbol is $\tilde{\mu}$).

In the following, the minimal supersymmetric extension of the Standard Model is considered¹ (abbreviated as MSSM, Minimal Supersymmetric Standard Model). The physically observable mass eigenstates are superpositions of the gauge eigenstates (which are listed in Tab. 2.3): the superposition of the neutral gauge bosons and the neutral higgsinos are the four neutral gauginos ($\tilde{\chi}_i^0, 1 \leq i \leq 4$), which are commonly referred to as neutralinos. Similarly, the charged gauge bosons and the charged higgsinos mix to give four charged gauginos ($\tilde{\chi}_1^\pm$ and $\tilde{\chi}_2^\pm$). The list of mass eigenstates for the MSSM is shown in Tab. 2.4, along with the gauge eigenstates that mix to produce them.

Standard Model particles and their supersymmetric partners can be distinguished by a quantity known as *R*-parity (or matter parity), defined as

$$P_R = (-1)^{3(B-L)+2S}, \quad (2.5)$$

where L is the lepton number, B the baryon number, and S the spin quantum number. All supersymmetric particles have odd *R*-parity ($P_R = -1$) whereas the

¹A concise summary of more complex models is given in [11].

Table 2.3: Standard Model particles and their supersymmetric partners in the minimal supersymmetric Standard Model (MSSM).

Standard Model particle			supersymmetric partner (MSSM)		
particle name	symbol	spin	sparticle name	symbol	spin
quark	q	$\frac{1}{2}$	squark	\tilde{q}	0
lepton	ℓ	$\frac{1}{2}$	slepton	$\tilde{\ell}$	0
gluon	g	1	gluino	\tilde{g}	$\frac{1}{2}$
W bosons	W^\pm, W^0	1	winos	$\tilde{W}^\pm, \tilde{W}^0$	$\frac{1}{2}$
B boson	B^0	1	bino	\tilde{B}^0	$\frac{1}{2}$
Higgs boson	H	0	higgsinos	\tilde{H}	$\frac{1}{2}$
graviton	G	2	gravitino	\tilde{G}	$\frac{3}{2}$

Table 2.4: Supersymmetric particles in the MSSM: gauge eigenstates (left) mix to give experimentally measurable mass eigenstates (right).

particle	spin	gauge eigenstate(s)	mass eigenstate(s)
Higgs bosons	0	$H_1^0, H_2^0, H_1^+, H_1^-$	h^0, A^0, H^0, H^\pm
squarks	0	\tilde{q}	\tilde{q}
sleptons	0	$\tilde{\ell}$	$\tilde{\ell}$
neutralinos	$\frac{1}{2}$	$\tilde{B}^0, \tilde{W}^0, \tilde{H}_1^0, \tilde{H}_2^0$	$\tilde{\chi}_1^0, \tilde{\chi}_2^0, \tilde{\chi}_3^0, \tilde{\chi}_4^0$
charginos	$\frac{1}{2}$	$\tilde{W}^\pm, \tilde{H}_1^\pm, \tilde{H}_2^\pm$	$\tilde{\chi}_1^\pm, \tilde{\chi}_2^\pm$
gluino	$\frac{1}{2}$	\tilde{g}	\tilde{g}
gravitino	$\frac{3}{2}$	\tilde{G}	\tilde{G}

Standard Model particles have even R -parity ($P_R = +1$). Whether or not the quantity is conserved in a decay splits the realm of supersymmetric models in two – those in which matter parity is a conserved quantity and models in which it is violated. In the following, only R -parity conserving theories are considered since experimental constraints severely restrict matter-parity violating contributions [11–23]. Consequences of matter-parity conservation include the following:

- (i) the lightest supersymmetric particle (which has $P_R = -1$) cannot decay to any Standard Model particle and is therefore stable;
- (ii) particle production at hadron colliders can only occur in pairs as the colliding initial states are composed of Standard Model particles;
- (iii) sparticles (other than the LSP) must decay to states containing an odd number of LSPs.

R -parity conservation, while well-motivated, is a choice; the MSSM would not become internally inconsistent if matter parity was violated.

2.3.1 Implications of the MSSM

The challenges of the Standard Model merit a re-examination in the context of the extended particle content of the MSSM:

- (i) The additional particles reduce the sensitivity to the mass of the Higgs boson, provided that the new particles are sufficiently light. Heavier new particles would imply increasing fine-tuning of the parameters²;
- (ii) While the gauge couplings cannot be unified in the Standard Model, the additional particles of the supersymmetric extension permit the inverse gauge couplings to meet at high energies (see Fig. 2.2), opening the door for a grand unified theory (GUT);
- (iii) In the case of R -parity conservation, the lightest supersymmetric particle (LSP) must be stable and can be an attractive candidate for dark matter, provided it is electrically neutral.

As previously mentioned, if supersymmetry is indeed a symmetry of nature, the non-observation of supersymmetric partners implies that it must be broken. There are many ways in which SUSY breaking can be realized; the most common examples [24] include gauge mediated symmetry breaking (GMSB) and minimal supergravity (mMSSM) [25]. In its most generic form, SUSY breaking introduces more than 100 new parameters to the theory. While experimental observations (and non-observations) constrain the parameters, simpler models with fewer parameters are generally used for interpretations of experimental results. Two such approaches are introduced in the following.

2.3.2 The Phenomenological Minimal Supersymmetric Standard Model (pMSSM)

In the phenomenological Supersymmetric Standard Model [26, 27], the number of free parameters is significantly reduced thanks to several phenomenological constraints and reasonably justified assumptions:

- (i) Since new sources of CP-violations are constrained, all parameters are taken to be real;

²This problem is known as the “little hierarchy problem”.

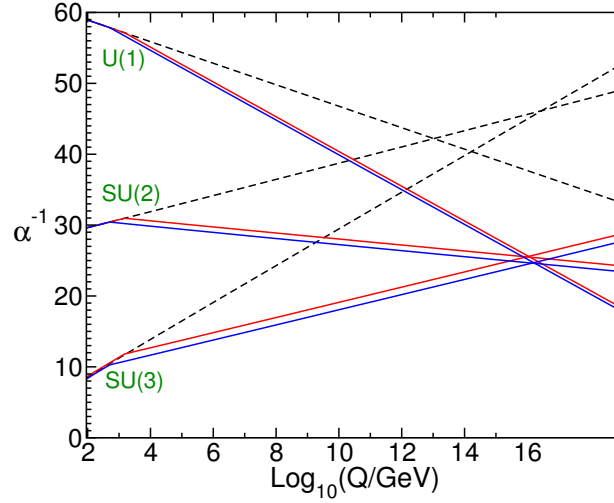


Figure 2.2: Evolution of the inverse gauge couplings α_i^{-1} as a function of the energy [11], computed in the Standard Model (dashed lines) and the MSSM case (red and blue lines); in the case of the MSSM, the sparticle masses were varied between 500 GeV and 1.5 TeV, and $\alpha_3(m_Z)$ is varied between 0.117 and 0.121. While the gauge couplings do not meet in the Standard Model, the unification is possible in the MSSM at very high energies.

- (ii) Current data severely constrains flavor-changing neutral currents; therefore, both mixing matrices for the sfermion masses and for the trilinear couplings (i.e. matrices describing the Higgs-squark-squark and Higgs-slepton-slepton interaction) are assumed to be diagonal, which leads to a significant reduction in the number of new parameters;
- (iii) It is assumed that the soft-SUSY breaking scalar masses are the same for the first and second generations since experimental data (e.g. from $K^0 - \bar{K}^0$ mixing [7, 26]) severely limits the splitting between the masses of the first and second generation squarks. One can assume that the trilinear couplings A_u , A_d , and A_l are the same for the two generations; some parameters in the Higgs sector can be related to Standard Model parameters.

After making these assumptions, only 19 free parameters remain:

- $\tan\beta = v_2/v_1$: the ratio of the two Higgs vacuum expectation values
- M_A : the pseudo-scalar Higgs mass
- μ : the higgsino mass parameter
- M_1, M_2, M_3 : the bino, wino, and gluino mass parameters

- $m_{\tilde{q}}, m_{\tilde{u}_R}, m_{\tilde{d}_R}, m_{\tilde{l}}, m_{\tilde{e}_R}$: first/second generation sfermion masses (degeneracy of first two generations is imposed)
- $m_{\tilde{Q}}, m_{\tilde{t}}, m_{\tilde{b}_R}, m_{\tilde{L}}, m_{\tilde{\tau}_R}$: third generation sfermion masses
- A_t, A_b, A_τ : third generation trilinear couplings

Additional theoretical constraints reduce the pMSSM space: the sparticle spectrum must be free of tachyons and cannot lead to color or charge breaking minima in the scalar potential. Furthermore, the model is required to be consistent with electroweak symmetry breaking and the Higgs potential must be bounded from below. Finally, the LSP must be the lightest neutralino, $\tilde{\chi}_1^0$.

A model satisfying these requirements has a reasonably low number of parameters while still providing an excellent proxy for the full MSSM.

2.3.3 Simplified Models of Supersymmetry (SMS)

Another approach to reduce the vastness of MSSM parameter space used to interpret experimental results within SUSY splits the typical modes of production and decay encountered in supersymmetric cascades into single chains, and considers each such chain as a standalone model. Such a simplified model [28–33] is, by itself, not a complete model, as it contains a minimal particle spectrum and number of particle decays. A given complete model can, however, be decomposed into a number of simplified models and any limit on cross-sections on individual simplified models can be used (with some degree of interpolation) to provide limits on the original complete model.

The striking advantage of simplified models lies in their simplicity and versatility: a single simplified model typically has between two and three supersymmetric particles, and therefore only between two and three free parameters. The initial particle (“mother particle”) can either decay directly, or undergo a cascade decay with an intermediate particle. The chain ends with a stable, neutral, undetected particle (the LSP, which can either be a gravitino or a neutralino) [28]. The masses of the mother particle and the LSP are usually free parameters, while the mass of the intermediate particle is governed by the x parameter,

$$m_{\text{intermediate}} = m_{\text{mother}} + (1 - x)m_{\text{LSP}}. \quad (2.6)$$

A given result can then be interpreted in the two-dimensional $m_{\text{mother}} - m_{\text{LSP}}$ mass parameter space for a given value of the x parameter (typical values are $x = \frac{1}{4}, \frac{1}{2}, \frac{3}{4}$).

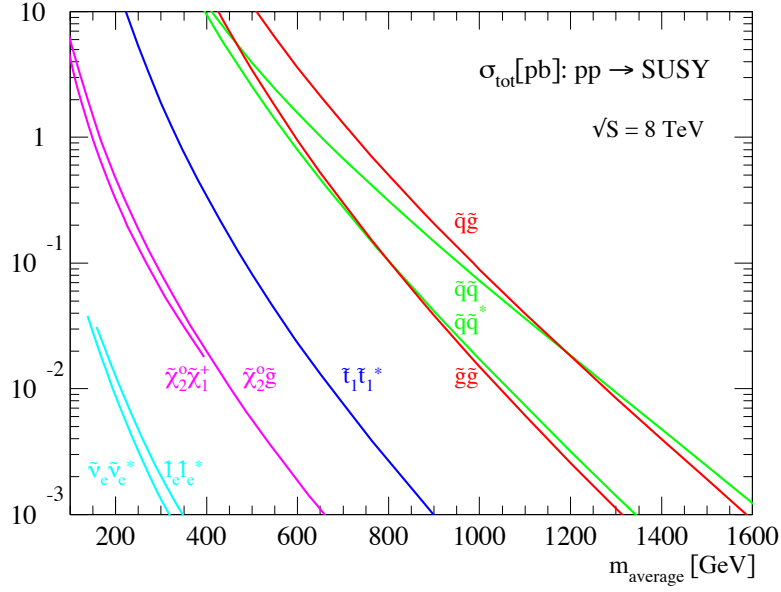


Figure 2.3: LHC cross-sections [34] for sparticle production at $\sqrt{s} = 8 \text{ TeV}$, calculated at next-to-leading order (NLO) by PROSPINO [35].

2.4 Particle Production and Decay

Supersymmetry can manifest itself in a broad range of final states; the production, however, always occurs in pairs due to R -parity conservation. The production is dominated by gluinos and the first two generations of squarks (see Fig. 2.3). Since these reactions are of QCD strength, the mode is commonly referred to as “strong production”. The second type of production is of electroweak strength, and leads to neutrinos and charginos (“electroweak production”).

Each particle of the original pair of supersymmetric particles undergoes a cascade decay, producing SM particles and a stable, lightest supersymmetric particle (LSP), which is the last element of the decay chain. The LSPs from the two branches escape undetected but lead to a momentum imbalance in the transverse detector plane (the magnitude of which depends on many factors, such as the mass of the LSP and the relative spatial orientation of the two LSPs).

In summary, events involving supersymmetric particles arise predominantly from strong production and therefore have high jet multiplicity; furthermore, due to the LSPs in the final state, the events also feature large missing transverse energy.

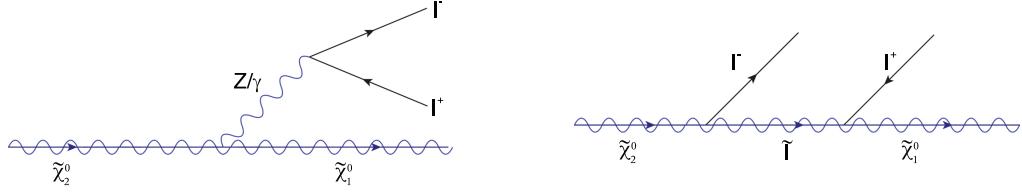


Figure 2.4: Lepton pair production in the decay of an $\tilde{\chi}_2^0$ into an $\tilde{\chi}_1^0$ via an on-shell Z boson or virtual Z/γ^* boson (left) or via a slepton (right).

2.4.1 The Dilepton Final State

The cascade decays of processes beyond the Standard Model lead to a broad array of final states, which can be classified according to the number of leptons n (where n can range from zero to more than three). In the case of zero leptons, the final state only contains jets and missing transverse energy, which is most effective if the branching ratios to leptonic final states are small; however, final states without leptons have large Standard Model backgrounds (which have very large cross-sections at hadron colliders), such as multijet production. Final states with leptons on the other hand tend to have smaller branching ratios but have significantly reduced backgrounds; these final states also offer kinematic handles to suppress the backgrounds even further and estimate them. The requirement of two leptons leads to a strong background suppression while maintaining good sensitivity: a study [36] of the sensitivity in the different final states using 7 TeV Monte Carlo simulation has shown that the opposite-sign same-flavor dilepton analysis was not only sensitive to a sizeable fraction of the tested models, but 20-40% of the models excluded by the search were inaccessible to analyses with zero leptons. The opposite-sign same-flavor dilepton final state therefore provides an orthogonal discovery mode.

A typical cascade decay leading to an opposite-sign dilepton final state is the decay starting with a squark,

$$\tilde{q} \rightarrow q + \tilde{\chi}_2^0 \rightarrow q + \tilde{\chi}_1^0 + l^\pm l^\mp, \quad (2.7)$$

where two leptons and an LSP are found in the final state. The decay of the second lightest neutralino ($\tilde{\chi}_2^0$) with two leptons in the final state can occur in the following ways (illustrated in Fig. 2.4):

- (i) $m_{\tilde{\chi}_2^0} - m_{\tilde{\chi}_1^0} > m_Z$:

If the mass difference between the two neutralinos is larger than the Z boson mass, the $\tilde{\chi}_2^0$ decay is given by

$$\tilde{\chi}_2^0 \rightarrow \tilde{\chi}_1^0 + Z,$$

and the Z can then decay leptonically to populate the opposite-sign dilepton final state.

- (ii) $m_{\tilde{\chi}_2^0} - m_{\tilde{\chi}_1^0} < m_Z$ and $m_{\tilde{\chi}_2^0} - m_{\tilde{\chi}_1^0} < m_{\tilde{l}}$:

If the mass difference between the neutralinos is smaller than the Z boson mass and any slepton mass, the exchange particles in Fig. 2.4 are virtual and a three body decay occurs: $\tilde{\chi}_2^0 \rightarrow \tilde{\chi}_1^0 \ell \ell$. The endpoint of the dilepton invariant mass distribution is given by

$$m_{\ell\ell}^{\text{edge}} = m_{\tilde{\chi}_2^0} - m_{\tilde{\chi}_1^0} . \quad (2.8)$$

- (iii) $m_{\tilde{\chi}_1^0} < m_{\tilde{l}} < m_{\tilde{\chi}_2^0}$:

If the slepton mass is between the masses of the two neutralinos, the decay via a slepton is kinematically allowed and two subsequent two-body decays take place,

$$\tilde{\chi}_2^0 \rightarrow \ell \tilde{\ell} \rightarrow \tilde{\chi}_1^0 \ell^+ \ell^- .$$

The endpoint of the resulting dilepton invariant mass is given by

$$m_{\ell\ell}^{\text{edge}} = \frac{\sqrt{(m_{\tilde{\chi}_2^0}^2 - m_{\tilde{l}}^2)(m_{\tilde{l}}^2 - m_{\tilde{\chi}_1^0}^2)}}{m_{\tilde{l}}} . \quad (2.9)$$

The dilepton mass distribution in the opposite-sign same-flavor final state can therefore allow for inferences about the masses of the particles involved in the decay.

Additional information about the masses can be obtained in this final state by considering the invariant mass distribution of quark-lepton systems. The system containing the lepton produced in the neutralino decay (abbreviated as ℓ_1) and the quark from the squark decay is denoted ($\ell_1 q$); its invariant mass distribution $m_{\ell_1 q}$ features an endpoint at

$$m_{\ell_1 q}^{\text{max}} = \frac{\sqrt{(m_{\tilde{q}}^2 - m_{\tilde{\chi}_2^0}^2)(m_{\tilde{\chi}_2^0}^2 - m_{\tilde{l}}^2)}}{m_{\tilde{\chi}_2^0}} . \quad (2.10)$$

Other distributions to consider are the invariant mass of the ($\ell_2 q$) and ($\ell\ell q$) system, which each contain additional endpoints; the combination of the endpoints can be used to reconstruct the particle masses of the decay cascade [37].

In conclusion, the opposite-sign same-flavor final state offers an orthogonal discovery mode, suppression of large Standard Model backgrounds, and potential mass reconstruction.

Table 2.5: Parameter values of pMSSM benchmark point.

parameter	$\tan\beta$	M_A (GeV)	μ (GeV)	M_1 (GeV)	M_2 (GeV)
value	24.2	565	854	311	224
parameter	M_3 (GeV)	$m_{\tilde{q}}$ (GeV)	$m_{\tilde{u}_R}$ (GeV)	$m_{\tilde{d}_R}$ (GeV)	$m_{\tilde{\ell}}$ (GeV)
value	846	1877	1190	919	280
parameter	$m_{\tilde{e}_R}$ (GeV)	$m_{\tilde{Q}}$ (GeV)	$m_{\tilde{t}_R}$ (GeV)	$m_{\tilde{b}_R}$ (GeV)	$m_{\tilde{L}}$ (GeV)
value	269	954	868	705	1519
parameter	$m_{\tilde{\tau}_R}$ (GeV)	A_t (GeV)	A_b (GeV)	A_τ (GeV)	
value	2277	1787	1570	1833	

A Benchmark pMSSM Point

A pMSSM point has been produced to illustrate the kinematic edge in the dilepton mass distribution. The parameters were chosen such that the mass of the Higgs boson was compatible with the measured values from CMS and ATLAS, and that the benchmark satisfied a range of experimental constraints (in analogy to [27]), such as the branching fractions of radiative penguin decays [38, 39]; these are subject to the flavor-changing neutral current, which only occurs via virtual loop diagrams in the Standard Model but can receive large additional new physics contributions when the Standard Model particles in the loop are replaced with new particles at a high mass scale. Another set of constraints stems from the sparticle mass limits from LEP [40].

The parameter values of the resulting benchmark are summarized in Tab. 2.5. The observables were computed using micrOMEGAs [41–43], and the mass of the Higgs boson for the benchmark is 124 GeV, which is close to the measured values. The benchmark also satisfies all previously mentioned constraints. The particle mass spectrum of the benchmark along with the different decay modes is shown in Fig. 2.5.

In this benchmark, supersymmetric particles can be produced³ via the strong interaction (production of squarks or gluinos) or via the electroweak interaction (production of charginos and neutralinos). In this model, the lightest chargino and the lightest neutralino have very similar masses (both approximately 233 GeV),

³The production modes were analyzed using SModelS [44].

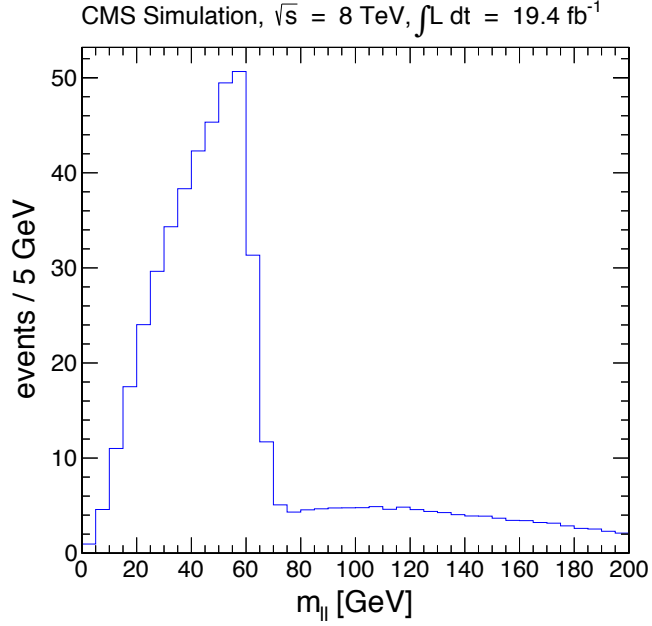


Figure 2.6: Dilepton invariant mass distribution for the pMSSM benchmark point described by the parameters summarized in Tab. 2.5. A clear kinematic edge can be seen at the expected endpoint of 62.4 GeV.

whereas the mass of the second neutralino is significantly different (307 GeV). The slepton mass is located between the neutralino masses (at around 280 GeV), so that a decay to a slepton is kinematically allowed. The value of the neutralino and slepton masses is arbitrary, but their relative masses (i.e. $m_{\tilde{\chi}_1^0} < m_{\tilde{\ell}} < m_{\tilde{\chi}_2^0}$) were chosen such that the cascade decay is kinematically allowed. A kinematic edge in the dilepton distribution is therefore expected to be located at 62.4 GeV (according to equation (2.9)). The dilepton invariant mass distribution for this model is shown in Fig. 2.6, where the kinematic edge can be seen. An additional contribution is visible at larger invariant masses, which stems from lepton pair combinations where each lepton is from a different decay cascade.

3

Experimental Apparatus

The masses of supersymmetric particles are expected to be relatively high; a search for such particles therefore crucially depends on the center-of-mass energy of the accelerator. Colliders are able to provide significantly higher center-of-mass energies than fixed target experiments with equal beam energy, making them much more practical for searches for high mass particles (and supersymmetric particles in particular). The probability of a given process taking place is linked to its cross-section σ_{proc} ; the concept of a cross-section stems from the classical picture of a scattering process, where an impinging particle sees an effective surface of the target particle. The cross-section is therefore measured in units of area, with the most common unit being barns (b), $1 \text{ b} = 10^{-28} \text{ m}^2$. The cross-section of a given process depends on the center-of-mass energy and can receive additional contributions as decay and production channels become available at higher energies. While the cross-section is specific to the process, the luminosity, \mathcal{L} , characterizes the accelerator performance; it represents the rate at which collisions occur. The number of events of a process within a given time T can be written as

$$N_{proc} = \sigma_{proc} \int_0^T \mathcal{L} dt = \sigma_{proc} L_{\text{int}} , \quad (3.1)$$

where the integral of the instantaneous luminosity over the time T is referred to as the integrated luminosity; it is a measure of the size of the collected data sample. The protons are squeezed together in so-called bunches (with transverse widths

σ_x and σ_y) which are brought into collision. Using the transverse widths of the bunches, the luminosity of a collider [45] can be written as

$$\mathcal{L} = \frac{N_1 N_2 f N_b}{4\pi\sigma_x\sigma_y}, \quad (3.2)$$

where N_1 and N_2 are the number of particles per bunch, N_b the number of bunches, and f the revolution frequency.

The analysis presented in Chap. 5 is carried out using particle collision data taken by the Compact Muon Solenoid (CMS) detector [6] at the Large Hadron Collider (LHC) [46–49]. An overview of the accelerator is given in Sec. 3.1, and the detector is described in Sec. 3.2.

3.1 The Large Hadron Collider (LHC)

The Large Hadron Collider (LHC) is a two-ring superconducting accelerator and collider, providing proton-proton collisions of up to 14 TeV of center-of-mass energy. The LHC is located in the 27 km long underground tunnel originally constructed for the Large Electron-Positron (LEP) collider [50] on the Franco-Swiss border.

The particle acceleration occurs through multiple steps (illustrated in Fig. 3.1), making use of large parts of the accelerator chain originally constructed for LEP before injecting the proton bunches into the LHC:

- (i) Hydrogen atoms from a gas bottle are stripped of their electrons by making an electrical discharge. The resulting protons are accelerated to 50 MeV in the Linear Accelerator 2 (LINAC2).
- (ii) The protons are then injected, in bunches, into the Proton-Synchrotron Booster (PSB), where they reach 1.4 GeV.
- (iii) The PSB is followed by the Proton Synchrotron (PS), where the energy is further increased to 25 GeV.
- (iv) The protons then arrive at the Super Proton Synchrotron (SPS) where they are accelerated to 450 GeV.
- (v) Lastly, the protons are injected into the two beam pipes of the LHC, where their energy is increased to 4 TeV (in 2012).

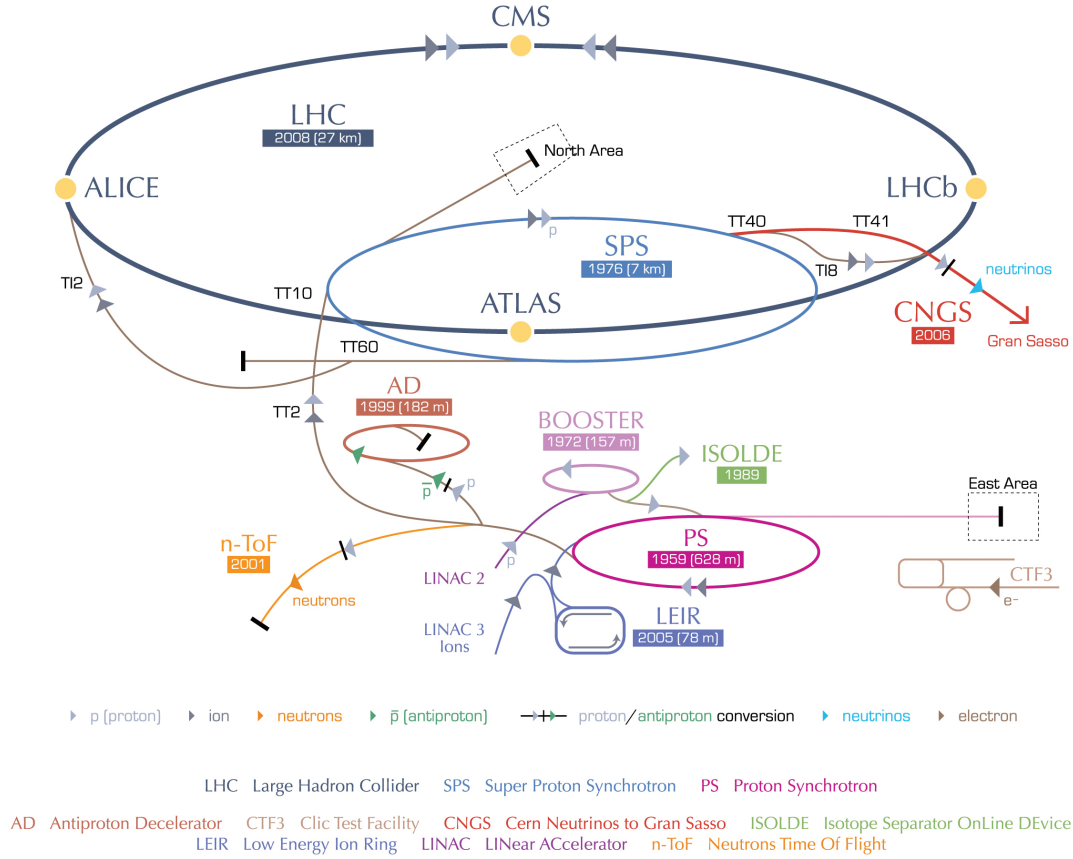


Figure 3.1: Accelerator Complex at CERN [51].

The fully accelerated bunches are then collided in detectors at four collision points located around the LHC ring: ATLAS [52], CMS [6], LHCb [53], and ALICE [54]. The ATLAS and CMS detectors are general purpose detectors, whereas LHCb focuses on b-physics and ALICE on heavy ion physics. In 2012, the LHC was operating at a center-of-mass energy of 8 TeV; the design value of 14 TeV may be reached in 2015 after the long shutdown of 2013/2014¹. The design and actual values for the 2012 run are summarized in Tab. 3.1.

¹The final center-of-mass energy after the long shutdown has not been decided at the time of writing.

Table 3.1: Design and actual (2012) parameters of the LHC; the integrated luminosity is the one delivered to CMS and ATLAS.

parameter	design	actual (2012)
center-of-mass energy E_{cm} [TeV]	14	8
Peak luminosity L [$\text{cm}^{-2}\text{s}^{-1}$]	10^{34}	$7.7 \cdot 10^{33}$
Integrated luminosity for CMS and ATLAS [fb^{-1}]	-	23.3
Bunch spacing [ns]	25	50
Number of bunches N_b per beam	2808	1380
Number of protons per bunch N_i	$1.2 \cdot 10^{11}$	$1.5 \cdot 10^{11}$

3.2 The Compact Muon Solenoid (CMS)

The CMS detector [6] is a general purpose detector designed to explore the physics at the TeV scale, elucidate the electroweak symmetry breaking mechanism, and to provide evidence for possible physics beyond the Standard Model [55]. The experiment's data also serves to make precision measurements [55].

While the CMS detector was designed to cover a broad range of analyses ranging from Standard Model measurements to new physics searches, a crucial benchmark for the design of the detector [56] was the search for the Higgs boson as it offers a multitude of decay modes (depending on the assumed Higgs mass). In the vicinity of the lower mass limit from LEP (114.4 GeV), hadronic decays dominate but are difficult to discover due to the large QCD backgrounds; decay modes with leptons and photons in the final state (e.g. $H \rightarrow WW \rightarrow \ell_1^\pm \nu_1 \ell_2^\mp \nu_2$) therefore become more favorable. The natural width of the Higgs boson is relatively small (a few MeV) in the allowed mass range up to $2 m_Z$ so that the observed width crucially depends on the instrumental mass resolution. For small Higgs masses (114–130 GeV), the diphoton channel is one of the principal channels, and the decay mode with two Z bosons becomes important for $m_H \gtrsim 130$ GeV, and is the mode of choice for large Higgs masses ($2m_Z < m_H < 600$ GeV). For very large Higgs masses ($600 < m_H < 1000$ GeV), modes with E_T^{miss} from W and Z bosons are used. The considerations of the array of decay modes lead to the following requirements that are not only relevant for the Higgs program but for the full physics program:

- (i) Good muon identification, momentum resolution (over a wide range of momenta), and good dimuon mass resolution;
- (ii) Good charged particle momentum resolution and reconstruction efficiency in the inner tracker;

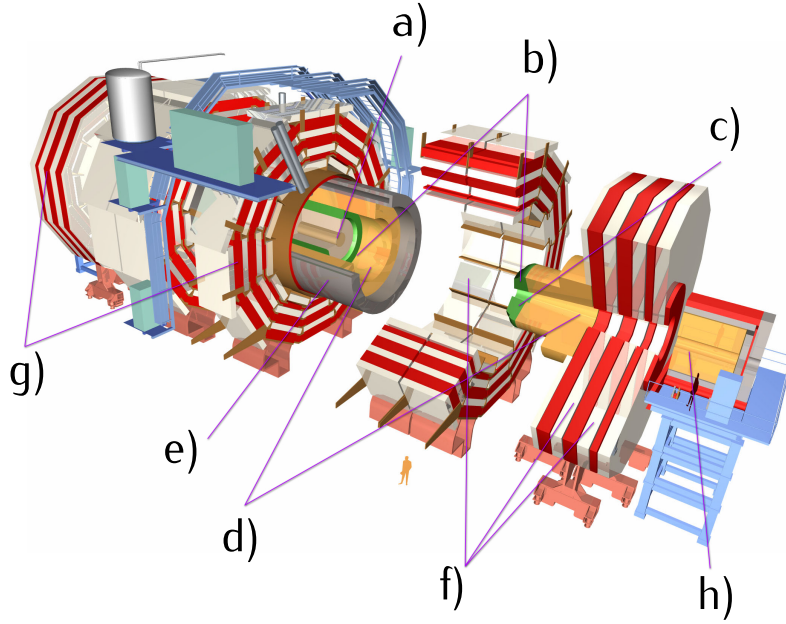


Figure 3.2: Layout of the CMS detector: silicon tracker (a), crystal electromagnetic calorimeter (b), preshower (c), hadron calorimeter (d), superconducting solenoid (e), muon chambers (f), steel return yoke (g), and forward calorimeter (h) [57].

- (iii) Good electromagnetic energy resolution, good diphoton and dielectron mass resolution;
- (iv) Good E_T^{miss} and dijet mass resolution, requiring a hadron calorimeter with a large hermetic geometric coverage.

The requirements were met using a relatively compact geometry; the CMS detector is approximately 22 meters long and about 15 meters in diameter, with a weight of 12,500 metric tons [55]. The full silicon-based tracker, the electromagnetic calorimeter and (most of) the hadronic calorimeter are located inside the strong superconducting solenoid magnet, which provides an axial magnetic field of 3.8 T. The different sub-detectors can be seen in the schematic in Fig. 3.2, and are briefly discussed in the following.

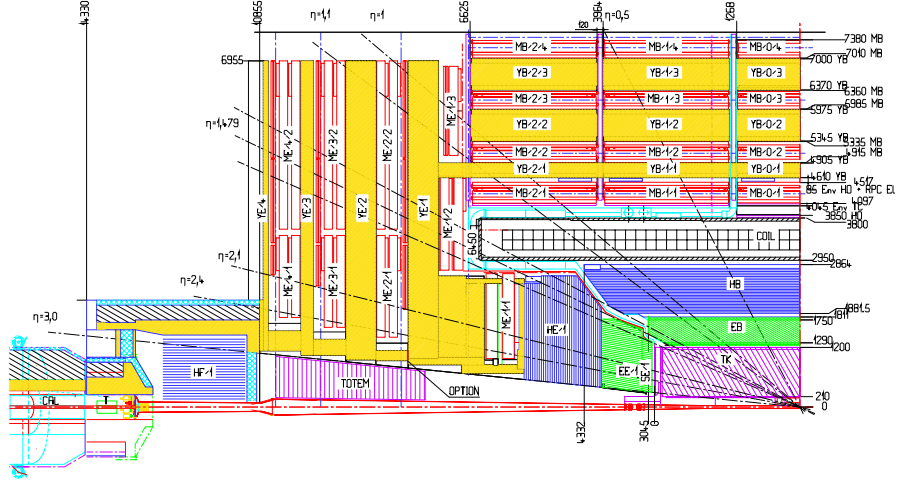


Figure 3.3: One quarter cross-sectional view of the CMS experiment with lines of constant pseudorapidity (η) superimposed and some dimensions (in mm) [56].

3.2.1 The CMS Coordinate System

The origin of the right-handed coordinate system of CMS is located at the nominal collision point, with the y coordinate axis pointing upward, the x -axis pointing radially towards the center of the LHC and the z axis pointing along the beam line (towards the Jura mountains).

A commonly used variable is the “pseudorapidity” η , which is defined using the polar angle θ measured from the z axis,

$$\eta = -\ln \left(\tan \frac{\theta}{2} \right) .$$

A cross-section of a quarter of the CMS detector is shown in Fig. 3.3 with lines of constant pseudorapidity superimposed; the barrel and endcap components of the electromagnetic calorimeter (green) and the hadronic calorimeter (blue) are also visible. The barrel components and tracker cover the region up to $|\eta| \lesssim 1.4$, after which the endcap sub-detectors provide coverage up to $|\eta| \sim 3.0$.

3.2.2 Inner Tracking Detectors

The innermost detector layer is the inner tracker [56], which consists of three different radial regions. The layer closest to the interaction point is made of pixel detectors, which are able to cope with the very high levels of particle flux present at these radii. The following intermediate region is composed of silicon microstrip

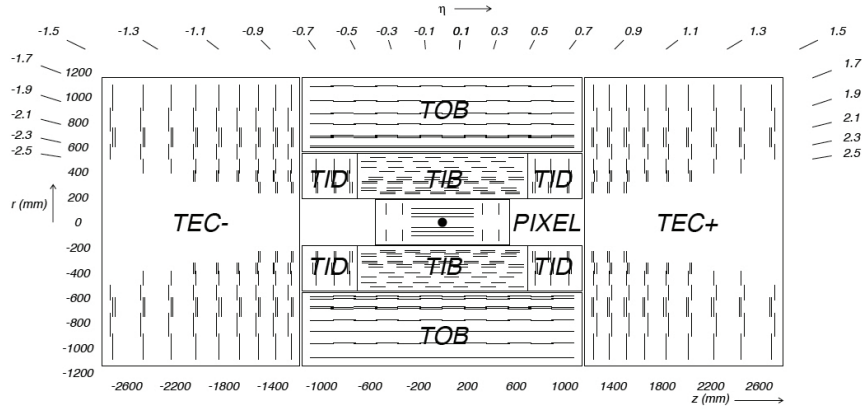


Figure 3.4: Schematic cross-section of the tracker, with each line representing a tracker module [6].

detectors, and the third region has sufficiently low particle flux to allow the use of larger pitch silicon microstrips. A schematic cross-section of the tracker is shown in Fig. 3.4.

Pixel Tracker

The pixel tracker is the part of the inner tracker located closest to the beam pipe and therefore exposed to the highest level of particle flux. The pixel tracker comprises three barrel layers, measuring 53 cm in length. Two endcap disks are located on each side at $|z| = 34.5$ cm and $|z| = 46.5$ cm. The spatial resolution is approx. $10 \mu\text{m}$ for the $r - \phi$ measurement and about $20 \mu\text{m}$ for the z measurement; it therefore provides precise tracking points, making a small impact parameter resolution possible, which is important for good secondary vertex reconstruction.

Strip Tracker

The barrel tracker consists of the inner and outer barrel. The inner barrel (Tracker Inner Barrel, TIB) comprises four layers which cover the region $|z| < 65$ cm with silicon sensors. The outer barrel (Tracker Outer Barrel, TOB) consists of six layers with a half-length of $|z| < 110$ cm.

The endcaps are made of the Tracker End Cap (TEC) and the Tracker Inner Disks (TID), with each TEC consisting of 9 disks covering the range $120 < |z| < 180$ cm, and each TID comprising 3 small disks covering the gap between the TIB and the TEC.

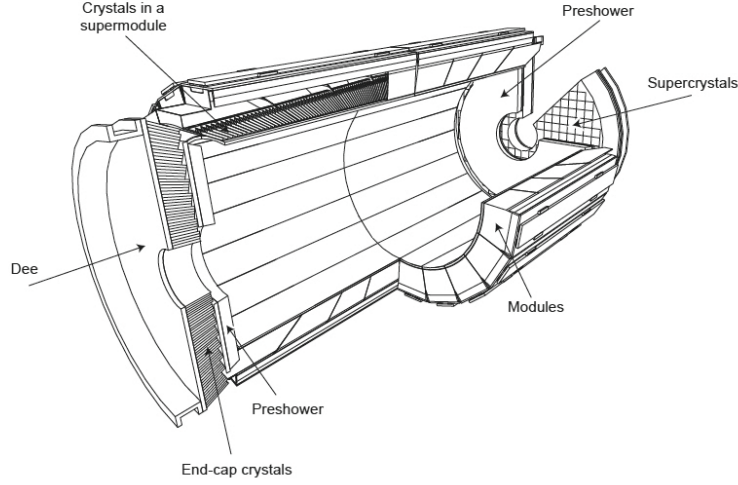


Figure 3.5: Layout of the electromagnetic calorimeter, indicating the arrangement of crystal modules, supermodules and endcaps, with the preshower in front [6].

As previously mentioned, components at larger radii use larger pitch silicon microstrips; for instance, the strip pitch for the TIB is between 80 and 120 μm , whereas the TOB (located at larger radii) has strip pitches up to 180 μm .

Tracker Performance

The transverse momentum resolution $\delta p_T/p_T$ for single muons was measured for $p_T = 1, 10, \text{ and } 100 \text{ GeV}$; it is below 1% for the former two cases up to $|\eta| < 0.9$ and remains below 2% across the pseudorapidity range. For the high- p_T case, the resolution is better than 2% up to $|\eta| \lesssim 1.6$, after which the resolution degrades (to up to 7% at $|\eta| = 2.4$).

3.2.3 Electromagnetic Calorimeter

The electromagnetic calorimeter (ECAL) consists of 61,200 lead tungstate (PbWO_4) crystals in the central barrel part and an additional 7324 crystals in each of the two endcaps. The barrel section has an inner radius of 129 cm and provides coverage for $|\eta| < 1.479$. It consists of 36 identical “supermodules”, each covering half the barrel length and 20° in ϕ . The crystals cover 1° each and are oriented in a quasi-projective geometry (the axes are tilted by 3° with respect to the line to the nominal interaction point).

The endcaps are located at a distance of 314 cm and cover the pseudorapidity range of $1.479 < |\eta| < 3.0$. The crystals each cover 0.0174 in $\Delta\phi$ and $\Delta\eta$, and have a front face of approx. $22 \times 22 \text{ mm}^2$ and a length of 230 mm ($25.8 X_0$).

A preshower detector is located between the inner tracking system and the endcaps in the pseudorapidity range $1.653 < |\eta| < 2.6$. The preshower detector consists of two planes of silicon strip detectors behind disks of lead absorber.

Electromagnetic Calorimeter Performance

The energy resolution of the electromagnetic calorimeter has been measured in a test beam [58], and can be parametrized as

$$\left(\frac{\sigma}{E}\right)^2 = \left(\frac{2.8\%}{\sqrt{E}}\right)^2 + \left(\frac{12\%}{E}\right)^2 + (0.30\%)^2. \quad (3.3)$$

The first term is the stochastic term, which stems from event-to-event fluctuations in lateral shower containment, photostatistics contribution, and fluctuations in the energy deposited in the preshower absorber. The second term is due to noise, comprising electronics noise, digitization noise, and pile-up noise. The last, constant term mainly stems from the non-uniformity of the longitudinal light collection, inter-calibration errors, and leakage of energy from the back of the crystal.

3.2.4 Hadronic Calorimeter

A peculiarity of CMS is the location of the magnet (see Sec. 3.2.6), which is situated outside most of the calorimetry to permit an accurate measurement of the particle transverse momentum and energy. The location of the magnet therefore drives the design of the hadronic calorimeter (HCAL), which is required to minimize the non-Gaussian tails in the energy resolution and to supply good containment and hermeticity for the E_T^{miss} measurement. The HCAL consists of four parts, the hadron barrel, hadron outer detector, hadron endcap, and the hadron forward calorimeter. Only the hadron outer detector is located outside the coil.

Hadron Barrel

The hadron barrel covers the pseudorapidity range $|\eta| < 1.4$. The absorber material (15 brass plates, each 5 cm thick, and two external stainless steel plates) alternates with plastic scintillator plates.

Hadron Outer

The hadron outer detector spans the region $|\eta| < 1.26$, and lines the outside of the outer vacuum tank of the coil with 10 mm thick scintillators. Its function is to sample the energy of hadron showers leaking through the rear of the calorimeters, increasing the effective thickness of the hadron calorimeter to over 10 interaction lengths. Furthermore, the hadron outer detector improves the E_T^{miss} resolution.

Hadron Endcaps

The hadron endcaps cover the $1.3 < |\eta| < 3.0$ region, and each consists of 14 η towers. The towers farthest away from the beam pipe in η have a $\phi \times \eta$ segmentation of $5^\circ \times 0.087$ whereas for the 8 innermost towers the ϕ segmentation is 10° while the η segmentation varies.

Hadron Forward

The hadron forward detector, consisting of steel/quartz fiber, extends the coverage of the hadron calorimeter by adding the $3.0 < |\eta| < 5.0$ region. Its front face is situated 11.2 m away from the interaction point (visible in Fig. 3.3 at the far left, labeled “HF-1”). The signal stems from Cerenkov light emitted in the quartz fibres, which is amplified in photomultipliers. The ϕ segmentation is 10° and the η granularity is between $\Delta\eta \approx 0.1$ and $\Delta\eta \approx 0.3$; the only exception is the tower closest to the beam pipe, for which the ϕ segmentation is 20° .

HCAL Performance

The hadronic energy resolution of the barrel HCAL and ECAL combination can be parametrized as

$$\frac{\sigma}{E} = \frac{a}{\sqrt{E}} \oplus b, \quad (3.4)$$

with a stochastic term a and a constant term b . Using different beams, the two terms have been measured [59] to be $a = (0.847 \pm 0.016) \text{ GeV}^{\frac{1}{2}}$ and $b = 0.074 \pm 0.008$. For HF the measured values are $a = 1.98 \text{ GeV}^{\frac{1}{2}}$ and $b = 0.09$.

3.2.5 Muon System

The muon system, illustrated in Fig. 3.6, consists of drift tube chambers (DT) in the barrel region ($|\eta| < 1.2$), followed by cathode strip chambers (CSC), which cover the region up to $|\eta| < 2.4$, and the resistive plate chambers (RPC) which are used both in the barrel and the endcap regions.

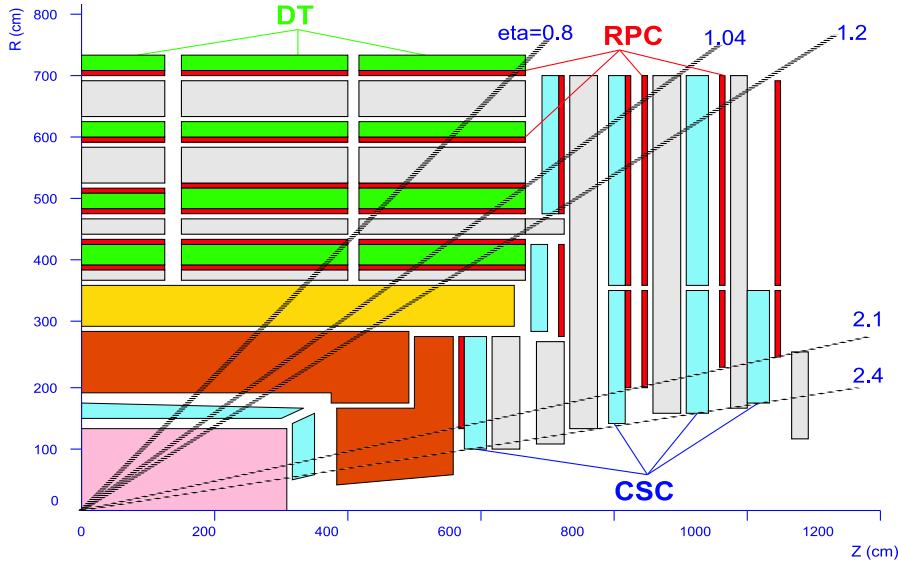


Figure 3.6: Labeled layout of the muon system with lines of constant pseudorapidity [56].

Drift Tube Chambers

The muon barrel (MB) detector consists of four layers of drift tube chambers, interleaved with layers of iron yoke.

Cathode Strip Chambers

The muon endcap (ME) system consists of 468 CSCs in two endcaps. The CSCs are of trapezoidal shape and consist of 6 layers; they are organized in concentric rings around the beam pipe.

Resistive Plate Chambers

The forward resistive plate chambers cover the pseudorapidity region up to $|\eta| < 2.1$. They provide an additional muon trigger system and allow to resolve ambiguities in the CSCs. A total of 36 chambers are arranged in each of the two rings in each endcap.

Performance

The muon momentum is measured in the inner tracker and in the return flux; the muon momentum resolution of the combined measurement is $\Delta p_T \approx 1\%$ for $|\eta| < 0.8$

and $p_T = 10$ GeV ($\Delta p_T/p_T \approx 4\%$ for $p_T = 1$ TeV). The resolution is degraded in the endcap regions ($\sim 2\text{--}10\%$).

3.2.6 Magnet

One of the main priorities of the detector design was the accurate measurement of particle transverse momentum, which is determined based on the sagitta of the particle trajectory. The curvature of the trajectory increases with the strength of the magnetic field, making it possible to determine the transverse momentum more accurately (especially for particles with high transverse momentum). The magnet was therefore a driving element in the design of the CMS detector. Its location also allows for a number of layers of the muon detectors within the magnetic field, permitting measurement of a muon's momentum on both sides of the magnetic coil (leading to a more precise overall measurement).

The magnet is a 12.9 m long solenoid made of a high-purity aluminum-stabilized conductor, which is cooled indirectly. The conductor has a cross-section of 64×22 mm², through which 20 kA of current flow. The solenoid is located outside the HCAL (with the exception of the HO), and provides a magnetic field of up to 4 T.

3.2.7 Trigger and Data Acquisition Systems

There are approximately 10^9 interactions per seconds, while only about 10^2 events per second can be stored. The trigger and data acquisition systems are thus tasked with reducing the rate by a factor of 10^7 , which is achieved in two main steps: the Level-1 trigger and the High-Level triggers.

The Level-1 trigger receives collision data for each event and makes a decision on whether to accept the event within a very short time frame ($3.2 \mu\text{s}$). Custom hardware is used in order to meet this demanding time limit. The Level-1 decision employs “trigger primitive” objects which are based on reduced granularity and resolution data from the calorimetry and muon systems; these objects include photons, electrons, muons, and jets for a given E_T^{miss} and p_T threshold. The output rate of the Level-1 trigger system is limited to 100 kHz, but typical values are on the order of 30 kHz.

Triggered events are transferred to front-end readout buffers, and are accessed by the data acquisition system. A given event is transferred to a processor of the High-Level trigger processor farm, which reduces the rate to about 100 Hz for mass storage. Instead of reconstructing all possible objects in an event, only objects and

regions of the detector which are directly needed are reconstructed, while events are discarded as soon as possible.

3.2.8 Software and Computing

Computing has played a central role in CMS [56, 60, 61], starting with the design, evaluation, construction, and calibration of the detector. Further roles include the storage, access, reconstruction, and analysis of data as well as the support of a distributed computing infrastructure for physicists engaged in these tasks.

The computing needs extend far beyond standard requirements and the computing model is therefore based on distributed computing. The computing model makes use of the tier hierarchy [60, 62]:

- (i) The primary computing center at CERN (Tier-0) is directly connected with the experiment for initial processing and data archival;
- (ii) A significant amount of processing is delegated to remote Tier-1 centers, which are connected to the Tier-0 using Grid technology and provide services for data archival, reconstruction, calibration, skimming and other data-intensive analysis tasks;
- (iii) A large number of Tier-2 centers (which are smaller but provide substantial CPU power) provide processing power for analyses, calibration activities, and Monte Carlo simulation; large datasets are accessed from Tier-1 centers.
- (iv) Finally, local groups use Tier-3 centers which also provide best-effort computing capacity for the collaboration.

The ensemble of global resources available make up the Worldwide LHC Computing Grid (WLCG), and the regions contributing WLCG resources use a homogeneous interface to their local grid environment. The end user can access the resources by providing a task to be completed, which is split into jobs that are submitted to the sites offering the required resources, and the output is made available upon completion.

4

Reconstruction

The event reconstruction is based on the particle flow algorithm [63, 64], which combines the information of all CMS sub-detectors to reconstruct and identify all stable particles in an event (electrons, muons, photons, charged hadrons and neutral hadrons). The large silicon tracker, immersed in a uniform axial magnetic field of 3.8 T provided by a superconducting solenoidal coil, and the excellent granularity of the ECAL (enhanced by an order of magnitude in the endcaps by the preshower) make the CMS detector almost ideally suited for a particle flow algorithm.

The particle flow (PF) algorithm is briefly summarized below in Sec. 4.1, and the reconstruction (and identification) of the different objects used in the analysis (in Chap. 5) are summarized in Sec. 4.2 – Sec. 4.7. The treatment of multiple proton-proton collisions occurring in the same bunch crossing (“pile-up”) is discussed in Sec. 4.8. A more detailed description of the reconstruction is given in [63].

4.1 The Particle Flow Algorithm

The PF algorithm first reconstructs the central elements (the charged-particle tracks, calorimetry clusters, and muon tracks) which are then linked into “blocks”, and interpreted as particles.

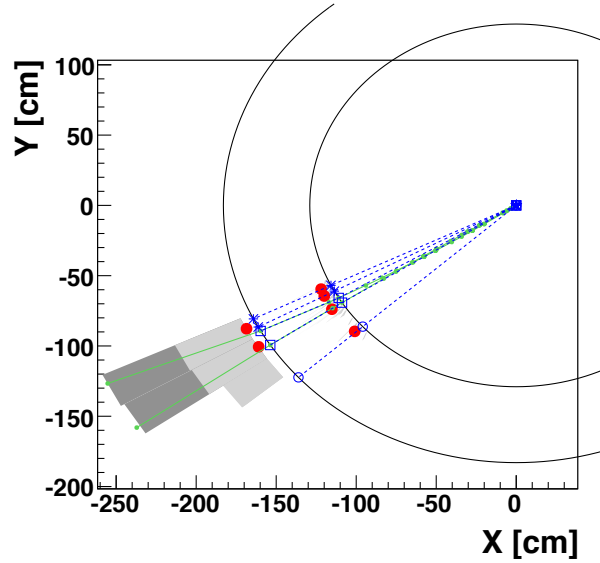


Figure 4.1: Event display of a simple hadronic jet; dots represent cluster positions, dashed lines indicate simulated particles, and open markers stand for the position of their impact on the calorimeter surfaces [63].

High efficiency and low fake rates are prerequisites of the PF algorithm. The tracker provides a momentum resolution which is vastly superior to that of the calorimeters (for p_T up to several hundred GeV), and it provides a precise measurement of the direction of a charged particle. A tracking algorithm is required to simultaneously have high efficiency and low fake rates since a missed hadron would only be reconstructed by the calorimeter (if at all), and a fake track could lead to large energy excesses. An iterative tracking strategy [65] meets both requirements by first seeding and reconstructing with tight criteria (providing moderate efficiency but negligible fake rate), followed by iterations with increasingly softer requirements (increasing the efficiency) while removing hits unambiguously assigned to tracks in the previous iterations (to retain a low fake rate). For the calorimeter, “cluster seeds” are identified as local calorimeter cell maxima, and adjacent cells are grouped into “topological clusters”. The “particle flow clusters” are then derived from the topological clusters.

An example of a simple hadronic jet with four particles is shown in Fig. 4.1, where the clusters are represented by dots and the simulated particles are indicated by dashed lines. In the simple example, four clusters are resolved from two topological clusters, one in ECAL and one in HCAL.

Since a particle can be detected in various sub-detectors, the PF elements must be connected with each other, which is done with a linking algorithm to avoid double counting. The last step consists of reconstructing and identifying particles based on the blocks of elements; this step is summarized below individually for the different particles.

4.2 Muon Reconstruction and Identification

The muon reconstruction [66–68] takes place before the particle flow reconstruction. The reconstruction starts by identifying hits in the different layers of the muon chamber, the drift tubes, and the CSCs. These hits are then used to construct straight-line track segments in the so-called “local reconstruction”, followed by two different approaches:

- (i) The hits and segments can be used to reconstruct muon tracks (“global reconstruction”), which can either be based on hits in the muon detector alone (“standalone muons”) or, alternatively, by combining hits in the muon detectors with those in the central tracker (“global muons”).
- (ii) The second approach considers all tracker tracks to be potential muons and extrapolates those tracks to the calorimeters and the muon system; if at least one muon segment corresponds to the extrapolated track, then the corresponding track is referred to as a “tracker muon”.

Low- p_T muons are less likely to leave enough hits in the muon system for a standalone muon, making “tracker muons” more useful for low- p_T muons ($p_T \lesssim 5$ GeV). On the other hand, the resolution for high- p_T global muons is better since the algorithm makes use of the full bending power of the CMS magnetic field.

Muon Identification

Muon identification employs cones around the particle candidate, which are constructed in $\eta - \phi$ space with a radius

$$\Delta R = \sqrt{(\Delta\eta)^2 + (\Delta\phi)^2},$$

where $\Delta\eta = \eta_i - \eta_j$ (and $\Delta\phi = \phi_i - \phi_j$) is the distance between the candidate particle i and another point j in η (ϕ) space. The sum of the transverse energy of all particle candidates within the cone (except the considered muon candidate), divided by the muon momentum, is referred to as the “relative isolation” of the muon. The sum is corrected for pile-up contributions to the total energy in the cone, which is based on charged particle deposits not originating from the leading primary vertex,

and takes the average charged/neutral particle ratio into account (see Sec. 4.8.3). Low values of the isolation variable imply little activity in the vicinity of the muon candidate. There are different selections (loose, soft, tight, and high- p_T muons) with varying identification criteria [66, 67], and consequently different efficiencies and fake rates. Any global or tracker muon fulfilling the particle flow identification is considered a loose muon; the tight muons in the analysis are global muons that fulfill an array of additional conditions to guarantee a good p_T measurement and to suppress hadronic punch-through, muons from decays in flight, accidental track-to-segment matches, and cosmic muons. Among the requirements for tight muons are a particle flow identification, at least one muon chamber hit included in the global-muon track, muon segments in at least two muon stations, at least one pixel hit and more than five hits on tracker layers.

Muon Selection

Muons in the analysis are required to have a relative isolation (computed with a cone size of $\Delta R = 0.3$) of less than 0.15, rejecting the large background arising from QCD production of jets where leptons are produced in the decay of low-mass particles, such as hadrons containing b and c quarks. The muons are required to be within $|\eta| < 2.4$, have a transverse momentum $p_T > 20$ GeV, and fulfill the “tight” identification criteria [66]. Since the electron and muon efficiencies are significantly different in the barrel transition region, muons in $1.4 < |\eta| < 1.6$ are not considered.

4.3 Electron Reconstruction and Identification

The tracker material (corresponding to up to two radiation lengths) leads to significant Bremsstrahlung photon emission, and the photons can be widely spread along the azimuthal direction due to the 3.8 T axial field. Two complementary electron reconstruction algorithms are used to face this challenge:

- (i) ECAL energy deposits within a given $\eta - \phi$ window are aggregated to form a “super-cluster”, which is then matched to track seeds in the inner tracker layer. Electron tracks are built from these track seeds utilizing a dedicated fitting procedure [69] which is able to cope with sudden changes in curvature due to Bremsstrahlung photon emission. This reconstruction algorithm is efficient for high- p_T , isolated electrons [70].
- (ii) The alternative approach finds electron energy deposits by extrapolating the electron track to the electromagnetic calorimeter, and then collecting all Bremsstrahlung photons (reconstructed with PF) by extrapolating a straight-line tangent to the electron track to the ECAL from each tracker layer.

The identification is carried out by using a number of tracking and calorimeter variables, such as the ratio of hadron calorimeter energy to electromagnetic calorimeter energy H/E , the shower shape variable $\sigma_{i\eta i\eta}$ (second moment of the cluster about its average η position), the relative isolation, and the number of missing inner hits. Several working points are defined [71], which are characterized by their respective efficiency and fake rate.

Electron Selection

Electrons are required to have a relative isolation of less than 0.15 computed with a cone size of $\Delta R = 0.3$, where the sum entering the isolation calculation is corrected for pile-up contributions (see Sec. 4.8, and in particular the effective area correction in Sec. 4.8.2). Electrons are also required to be in $|\eta| < 2.4$, have a transverse momentum of $p_T > 20$ GeV, and fulfill the loose identification criteria. The pseudorapidity region $1.4 < |\eta| < 1.6$ is not considered.

4.4 Tau Reconstruction and Identification

Taus can either decay leptonically (with a probability of about 35% [7]) or hadronically (with a probability of about 65%). In the leptonic case, an electron (or a muon) is produced along with a neutrino and an anti-neutrino. In the hadronic case, one or three charged hadrons and a number of π^0 mesons are produced, which decay into photons. Hadronic taus are reconstructed based on the decay products by using the particle flow technique and the “hadron plus strips” (HPS) algorithm [58, 72], which uses several cuts on the hadron multiplicity and the invariant mass of charged hadrons and neutral pions reconstructed in a narrow cone of size $\Delta R = 2.8/p_T$; no other particles above a certain threshold are allowed to be within the jet. A set of different working points is defined [73] with varying efficiencies and fake rates.

Hadronic taus are not used in the analysis.

4.5 Photon Reconstruction and Identification

The essentially hermetic electromagnetic calorimeter surrounding the tracker, along with the large magnetic field and the ECAL granularity, allows the particle-flow technique to reconstruct photons with an excellent energy resolution. The granularity is important as it allows photons to be separated from charged-particle energy deposits. Photons (and neutral hadrons) are reconstructed from energy deposits in the calorimeters. Any deposit away from the extrapolation of reconstructed tracks are a clear signature of neutral particles, whereas energy deposits overlapping

with reconstructed charged particle candidates can be recovered by comparing the energy to the sum of the associated track momenta. The photons are identified using isolation, shower shape variables, and the ratio of energy deposits in the single hadronic calorimeter tower divided by the energy deposits in the single electromagnetic calorimeter tower. Furthermore, a veto is generally used to protect against converted photons.

Photons are not used in the analysis. Electrons from conversions are vetoed, but no explicit photon veto is used.

4.6 Jet Reconstruction and Identification

Due to confinement, quarks and gluons produced in collisions cannot exist freely but form quark-antiquark pairs during parton showering and hadronization. The experimental signature of a quark or gluon in the detector is therefore a tight cone of particles, referred to as a “jet”, moving in a common direction. The original parton (gluon or quark) is reconstructed using a jet clustering algorithm. CMS makes use [74] of the anti- k_T jet clustering algorithm [75], which measures the distance d_{ij} between two entities (particles or pseudojets) i and j using the transverse momenta $k_{t,i}$, rapidity $y_i = \frac{1}{2} \ln \left(\frac{E+p_z}{E-p_z} \right)$, and azimuthal angle ϕ of the particles,

$$d_{ij} = \min(k_{ti}^{2p}, k_{tj}^{2p}) \frac{\Delta_{ij}^2}{R^2}, \quad (4.1)$$

where $\Delta_{ij}^2 = (y_i - y_j)^2 + (\phi_i - \phi_j)^2$, R is the radius parameter, and p is a parameter to modify the relative power of the energy versus the geometrical (Δ_{ij}) scales. The distance between an entity i and the beam is defined as

$$d_{iB} = k_{ti}^{2p}. \quad (4.2)$$

The inclusive k_T algorithm [76] is recovered by setting $p = 1$, while the inclusive Cambridge/Aachen algorithm [77] corresponds to $p = 0$, and the anti- k_T algorithm uses $p = -1$. Note that all these variants are infrared and collinear safe. The jet clustering proceeds iteratively by first calculating the distances d_i and d_{ij} , considering the smallest distance and then either (a) combining entities i and j if d_{ij} is the smallest distance or (b) calling i a jet and removing it from the list if d_i is the smallest distance. The distances are recomputed after each step until no entities are left.

The typical cone size used in CMS is $R = 0.5$, and the anti- k_T algorithm is implemented in the *FastJet* package [78, 79]. The four-momentum vectors of the PF

particles are clustered to reconstruct the particle-flow jets [64, 80]. Other types of jets include calorimeter jets (“calo jets”), which are reconstructed from energy deposits in the calorimeter, and Jet-Plus-Track jets (“JPT jets”), which are based on calorimeter jets but improve their energy response and resolution by using track information.

4.6.1 Jet Energy Corrections

The raw jet energy measurement from the detector is calibrated to relate, on average, to the energy of the corresponding true particle jet resulting from the clustering of all stable particles from the fragmenting parton but also from the underlying event activity. The correction factor \mathcal{C} is applied to every component of the jet four-momentum p_μ^{raw} ,

$$p_\mu^{\text{corr}} = \mathcal{C} \cdot p_\mu^{\text{raw}} \quad (4.3)$$

The correction factor \mathcal{C} consists of the offset correction $\mathcal{C}_{\text{offset}}$, the Monte Carlo calibration factor \mathcal{C}_{MC} , and the residual calibrations \mathcal{C}_{rel} and \mathcal{C}_{abs} for the relative and absolute energy scale, respectively,

$$\mathcal{C} = \mathcal{C}_{\text{offset}}(p_T^{\text{raw}}, \eta) \cdot \mathcal{C}_{\text{MC}}(p_T', \eta) \cdot \mathcal{C}_{\text{rel}}(\eta) \cdot \mathcal{C}_{\text{abs}}(p_T''), \quad (4.4)$$

where p_T' is the transverse momentum of the jet after applying the offset correction, and p_T'' is the transverse momentum of the jet after all previous corrections.

The offset correction estimates and subtracts the energy from electronics noise and pile-up (for more details on pile-up see Sec. 4.8). The correction is computed by first adding infinitely small four momenta to the event and then carrying out jet clustering with $R = 0.6$ using the anti- k_T algorithm [75, 81, 82]. The resulting area occupied in $\phi - y$ space is the jet area A . The average p_T density ρ is then defined on an event-by-event basis as the median of the distribution of the p_{Tj}/A_j variable (with j running over all jets in the event). The offset correction can then be written as

$$\mathcal{C}_{\text{offset}}(p_T^{\text{raw}}, \eta, A_j, \rho) = 1 - \frac{(\rho - \langle \rho_{\text{UE}} \rangle) \cdot \beta(\eta) \cdot A_j}{p_T^{\text{raw}}} \quad (4.5)$$

where $\langle \rho_{\text{UE}} \rangle$ is the p_T -density component due to the underlying event activity and electronics noise. The small variation of the detector response as a function of the pseudorapidity is accounted for by $\beta(\eta)$.

The Monte Carlo correction (\mathcal{C}_{MC}) is derived based on the comparison between the energy of the reconstructed jet and the generated Monte Carlo particle jet, and links the former to the latter. The reconstructed jets are matched to the generated

particle jets using a cone of size $\Delta R = 0.25$ in $\eta - \phi$ space; the response variable $\mathcal{R} = p_{\text{T}}^{\text{reco}}/p_{\text{T}}^{\text{gen}}$ and the detector jet transverse momentum $p_{\text{T}}^{\text{reco}}$ are used to compute the average correction factor,

$$\mathcal{C}_{\text{MC}} = \frac{1}{\langle \mathcal{R} \rangle}, \quad (4.6)$$

as a function of the average detector transverse momentum $\langle p_{\text{T}}^{\text{reco}} \rangle$.

The relative jet energy scale correction measures the response of a jet at any given pseudorapidity and relates it to the jet energy response in the region $|\eta| < 1.3$. The measurement uses the dijet p_{T} -balancing method [83–85] which is based on transverse momentum conservation and utilizes the p_{T} -balance in dijet events.

The absolute jet energy scale is measured in the reference region $|\eta| < 1.3$ using the $E_{\text{T}}^{\text{miss}}$ -projection fraction (MPF) method [84], which is based on the fact that $Z + \text{jets}$ events do not have any intrinsic $E_{\text{T}}^{\text{miss}}$. At parton level, the Z (or γ) is therefore perfectly balanced by the hadronic recoil in the transverse plane:

$$\vec{p}_{\text{T}}^{\gamma, Z} + \vec{p}_{\text{T}}^{\text{recoil}} = 0. \quad (4.7)$$

At reconstruction level, the detector response for the recoil (R_{recoil}) and for Z/γ (R_{γ}) need to be taken into account,

$$R_{\gamma} \vec{p}_{\text{T}}^{\gamma, Z} + R_{\text{recoil}} \vec{p}_{\text{T}}^{\text{recoil}} + \vec{E}_{\text{T}}^{\text{miss}} = 0, \quad (4.8)$$

which leads to the following expression for the hadronic recoil R_{recoil} :

$$R_{\text{recoil}} = R_{\gamma, Z} + \frac{\vec{E}_{\text{T}}^{\text{miss}} \cdot \vec{p}_{\text{T}}^{\gamma, Z}}{(\vec{p}_{\text{T}}^{\gamma, Z})^2} \equiv R_{\text{MPF}}. \quad (4.9)$$

The value of R_{MPF} is measured for different thresholds on $\alpha = p_{\text{T}}^{\text{jet2}}/p_{\text{T}}^{\gamma}$ for data and Monte Carlo simulation, and an extrapolation to $\alpha = 0$ is carried out. The result of the extrapolation is

$$\lim_{\alpha \rightarrow 0} \frac{R_{\text{MPF}}^{\text{data}}}{R_{\text{MPF}}^{\text{MC}}} = 0.985 \pm 0.001, \quad (4.10)$$

leading to an absolute correction term of $\mathcal{C}_{\text{abs}} = 1.015$ [74] in (4.4).

The total jet energy correction factor, \mathcal{C} , is shown in Fig. 4.2 as a function of the pseudorapidity (for two different values of p_{T}) and in Fig. 4.3 as a function of p_{T} (for two different values of the pseudorapidity). Further (optional) corrections, such as for the jet flavor, can be applied to correct for remaining residual effects. The uncertainty on the total jet energy scale is shown in Fig. 4.4.

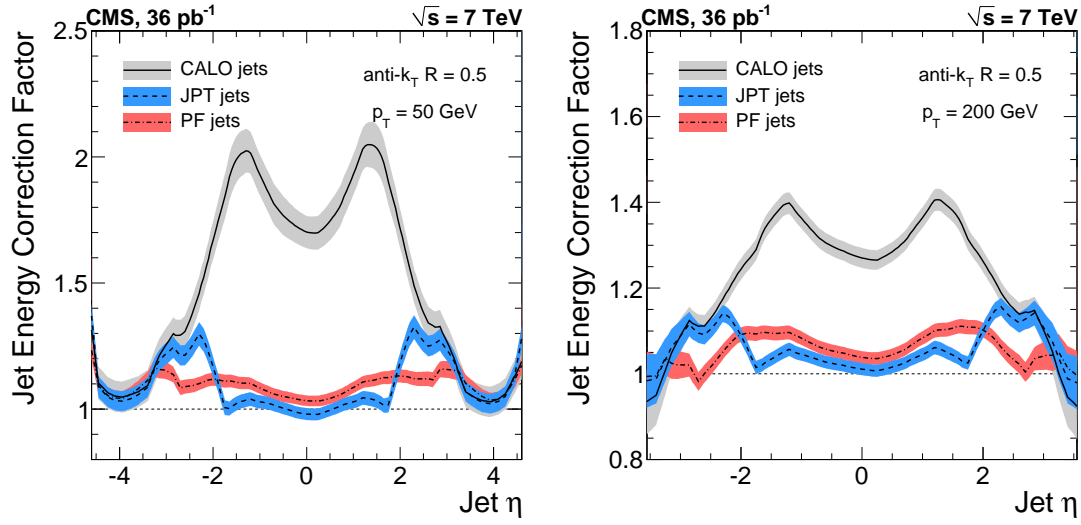


Figure 4.2: Total jet energy correction factor, as a function of the pseudorapidity for two different p_T values. The bands indicate the corresponding uncertainty [74].

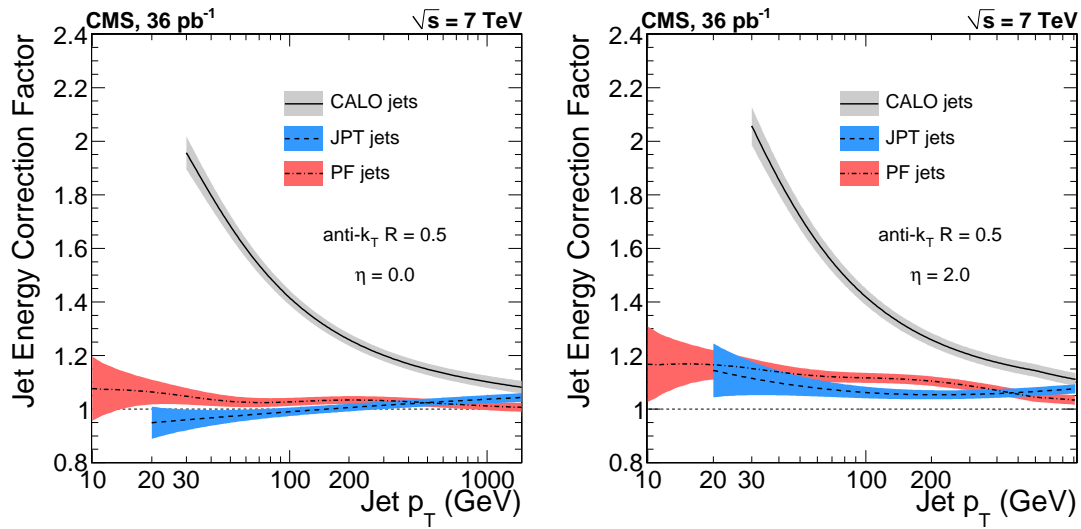


Figure 4.3: Total jet energy correction factor, as a function of the transverse momentum for two different η values. The bands indicate the corresponding uncertainty [74].

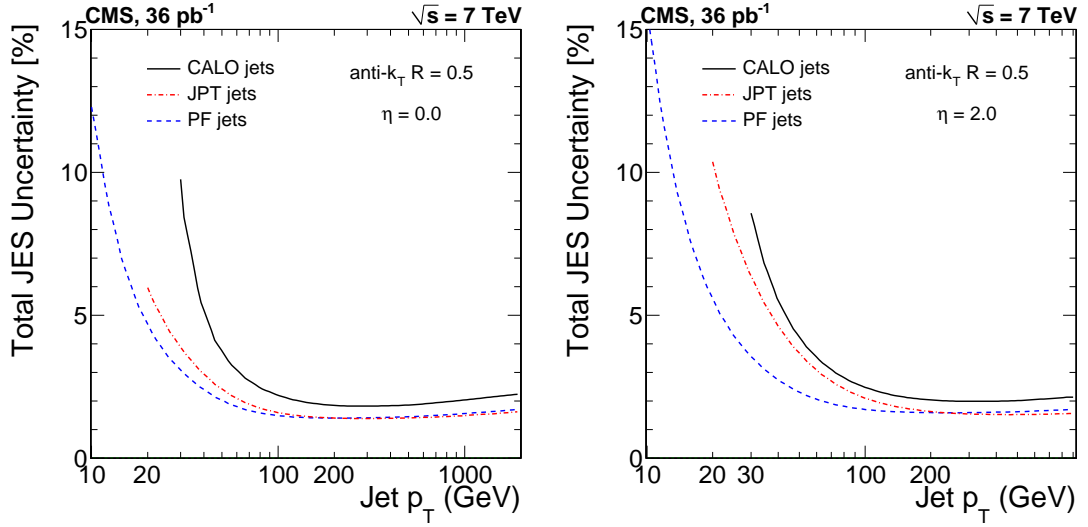


Figure 4.4: Total jet energy scale uncertainty as a function of the transverse momentum for two different η values [74].

Jet Selection

Particle flow jets in the analysis are reconstructed with a cone size of $\Delta R = 0.5$; they are required to be within $|\eta| < 3.0$ and have $p_T > 40$ GeV. Furthermore, they must be separated by $\Delta R > 0.4$ from any of the leptons (as defined in the previous Sections).

4.7 Missing Transverse Energy Reconstruction

The missing transverse energy, E_T^{miss} , is defined as the imbalance in the transverse plane of all visible particles in the final state [86]. Momentum conservation implies that the E_T^{miss} corresponds to the sum of the p_T of weakly interacting particles, such as neutrinos. Several algorithms exist to reconstruct the missing transverse energy [87]; algorithms including tracker information have an improved resolution, while the global particle-flow event reconstruction leads to the best resolution. The particle-flow event reconstruction based E_T^{miss} is the most commonly employed algorithm, and is also used in the present analysis.

The performance was enhanced for 2012 data by introducing specific corrections to account for the larger number of pile-up interactions. While pile-up interactions are minimum bias proton-proton interactions, whose true E_T^{miss} is close to zero, the E_T^{miss} points, on average, in the direction of the vectorial p_T sum of neutral particles,

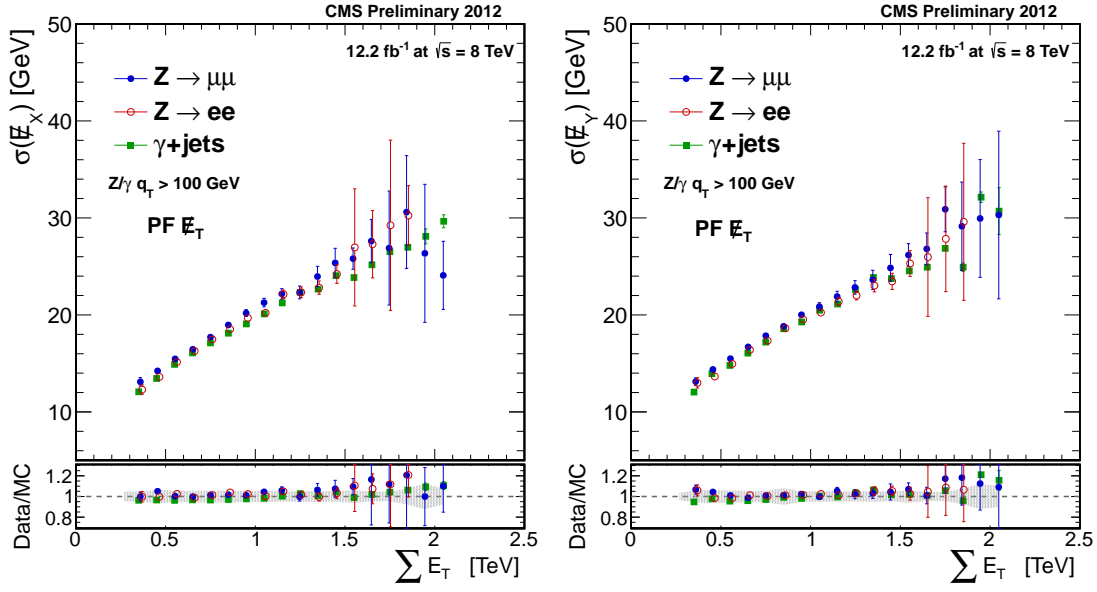


Figure 4.5: Resolution of the particle-flow E_T^{miss} projection along the x axis (left) and y axis (right) as a function of $\sum E_T$ for events with a Z and a γ (blue circles represent $Z \rightarrow \mu^+ \mu^-$ events, red circles stand for $Z \rightarrow e^+ e^-$ events, and full green squares illustrate photon events). The response in data is shown in the top frame whereas the ratio between data and Monte Carlo simulation is shown in the bottom frame [86].

which is due to calorimeter non-linearity and minimum energy thresholds in the calorimeters. A correction has been introduced (“type-0 correction”) to account for this effect by considering the vectorial p_T sum of charged particles associated with pile-up as an estimator of the induced E_T^{miss} [86].

Additionally, the energy corrections discussed in Sec. 4.6.1 can also be propagated to the E_T^{miss} (referred to as type-1 corrected E_T^{miss}),

$$\vec{E}_T^{\text{miss,corr}} = \vec{E}_T^{\text{miss}} - \sum_{\text{jets}} (\vec{p}_{T,\text{jet}}^{\text{corr}} - \vec{p}_{T,\text{jet}}) , \quad (4.11)$$

where $\vec{E}_T^{\text{miss,corr}}$ and $\vec{p}_{T,\text{jet}}^{\text{corr}}$ are the corrected missing transverse energy and transverse jet momentum, respectively.

The E_T^{miss} resolution in events with a Z or a γ , as a function of the vectorial p_T sum of all reconstructed particles (except for dileptons from Z bosons or the photons), is shown for the parallel and perpendicular components in Fig. 4.5.

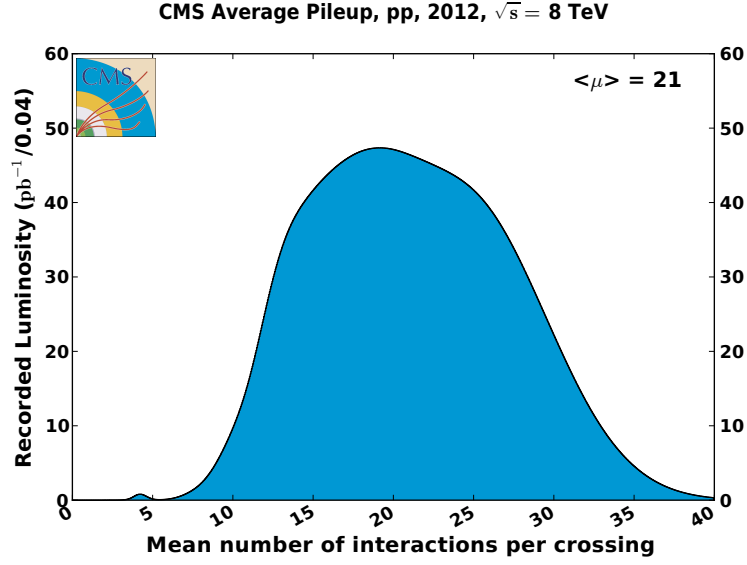


Figure 4.6: Mean number of interactions per bunch crossing [88].

Missing Transverse Energy in the Analysis

The particle-flow based E_T^{miss} is used in the definition of the signal region in the analysis but not in the pre-selection; only the type-0 correction is used to account for pile-up.

4.8 Pile-Up

The high luminosity of the LHC leads to various proton-proton collisions occurring in the same bunch crossing. A given considered event therefore not only contains a hard scatter process, but also a number of further, typically soft, proton-proton interactions; this effect is referred to as pile-up. A distinction is generally made between three types of pile-up, based on their time of entry in calorimeter system: in-time pile-up refers to energy in proton-proton collisions in the current bunch-crossing, while early out-of-time pile-up stems from left over energy deposits from earlier bunch crossings. The opposite is also possible (late out-of-time pile-up), which can occur when energy deposits from the following bunch crossing are integrated with the energy deposited in the current event.

The mean number of interactions per bunch crossing in the proton-proton collision CMS data sample at $\sqrt{s} = 8$ TeV is shown in Fig. 4.6. There are on average 21

interactions per bunch crossing, leading to considerable additional energy deposits which obscure the hard-scatter physics signal of interest, posing one of the main challenges faced by the LHC experiments. Pile-up leads to challenges in vertexing due to additional primary vertices from the other proton-proton collisions, in particle identification due to the additional energy deposits (which affects the isolation variable), in the jet energy scale, in the missing transverse energy, and in various other aspects of the reconstruction.

Pile-up effects therefore need to be taken into consideration. In the following, three mitigation techniques (used in the analysis) are explained in further detail: the jet area correction is described in Sec. 4.8.1, followed by the effective area correction used in the electron isolation in Sec. 4.8.2, and the $\Delta\beta$ correction used in the muon isolation in Sec. 4.8.3.

4.8.1 Jet Area Correction

One pile-up mitigation technique [74] relies on the so-called “jet area”, which is computed by adding a large number of infinitely small four-momenta to the event (as mentioned in Sec. 4.6.1), and carrying out the jet clustering again with a cone size of $R = 0.6$. The area in $y - \phi$ space occupied by the soft particles clustered in each jet is then defined as the jet area A . The jet area can then be used to estimate the average p_T density ρ per unit area in the event which characterizes the soft jet activity (i.e. the underlying event, electronics noise, and pile-up); the average p_T density per unit area of an event is defined as the median of the p_{Tj}/A_j distribution for all the jets j present in the event. The quantity ρ can be interpreted as the convolution of the true particle-level activity with the detector response to various particle types. The average p_T density per unit area is also measured in events with exactly one reconstructed primary vertex (i.e. no pile-up) to extract the density due to electronics noise and the underlying event alone, referred to as $\langle\rho_{UE}\rangle$. The difference between the measured value of ρ and the reference value without pile-up, $\langle\rho_{UE}\rangle$, can then be used to calculate a correction term,

$$C_{\text{area}}(p_T^{\text{raw}}, A_j, \rho) = 1 - \frac{(\rho - \langle\rho_{UE}\rangle) \cdot A_j}{p_T^{\text{raw}}} . \quad (4.12)$$

The resulting correction is uniform in the pseudorapidity; however, the detector response is not η -invariant. Therefore, an additional factor $\beta(\eta)$ is added to correct for the non-uniformity of the energy response,

$$C_{\text{area}}(p_T^{\text{raw}}, A_j, \rho) = 1 - \frac{(\rho - \langle\rho_{UE}\rangle) \cdot \beta(\eta) \cdot A_j}{p_T^{\text{raw}}} . \quad (4.13)$$

The non-uniformity correction $\beta(\eta)$ can be shown to be relatively stable as a function of η for particle flow jets. The resulting pile-up corrected jets are also used in the calculation of the missing transverse energy (as mentioned in Sec. 4.7).

4.8.2 Effective Area Correction

The electron identification relies on the relative isolation of the electron candidate, i.e. the amount of energy present in the immediate vicinity of the candidate, which can be written as

$$\text{Iso} = \frac{\left(\sum p_{\text{T}}^{\text{charged had}} + \sum p_{\text{T}}^{\text{neutral had}} + \sum p_{\text{T}}^{\gamma} \right)}{p_{\text{T}}}, \quad (4.14)$$

where the sums run over charged particle flow candidates (first term) originating from the relevant primary vertex of the event, and the neutral particle flow candidates and photons (second and third terms). The observables entering the isolation are, however, very sensitive to additional energy deposits from pile-up, which would lead to larger values of the isolation and therefore lead to electron candidates being rejected (lowering the identification efficiency).

A similar approach to the jet area method presented in the previous Section can be used for electrons [89–92]: instead of using a jet area A (as for the jets), an effective area A_{eff} is used; this effective area is defined as the geometric area of the isolation cone, scaled by a factor to account for a residual pseudorapidity dependence of the average pile-up deposition. The effective area is determined in a $Z \rightarrow ee$ sample and the values are specific to the analyzed run period. The p_{T} density parameter ρ is defined as the median of the energy density distribution for the particles within the area of any jet in the event (reconstructed using the anti- k_{T} jet clustering algorithm [75], with distance parameter $R = 0.5$ for jets with $p_{\text{T}} > 3$ GeV and $|\eta| < 2.5$). The correction can then be written as $p_{\text{T}}^{\text{PU}}(\text{ele}) = \rho A_{\text{eff}}$, and the isolation becomes [89]

$$\text{Iso} = \frac{\left(\sum p_{\text{T}}^{\text{charged had}} + \max \left[0, \sum p_{\text{T}}^{\text{neutral had}} + \sum p_{\text{T}}^{\gamma} - p_{\text{T}}^{\text{PU}}(\text{ele}) \right] \right)}{p_{\text{T}}}. \quad (4.15)$$

The different components entering the isolation are shown in Fig. 4.7 as a function of the number of primary vertices, along with the isolation variable. The inclusion of the effective area correction leads to a significantly reduced dependence on the number of vertices¹.

¹Note that while the plots are shown for $|\eta| < 1.0$, similar conclusions hold for regions outside this specific pseudorapidity range.

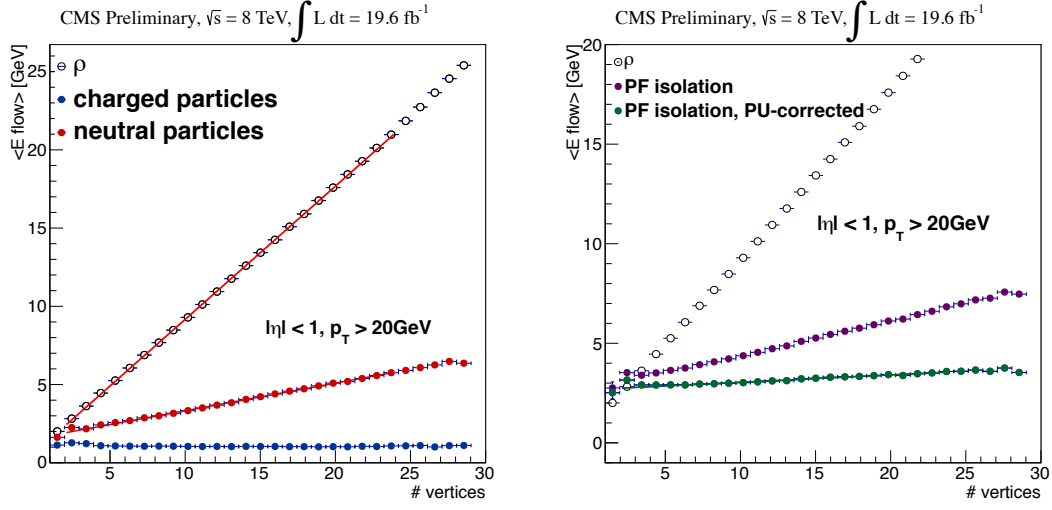


Figure 4.7: Contributions entering the particle isolation calculation, including the average energy density ρ , shown as a function of the number of reconstructed primary vertices (left); the isolation with and without the effective area correction are also shown (right) [93].

4.8.3 Pile-Up Correction for Muons

The muon isolation is also corrected to account for effects of additional interactions [94]. The charged particle flow candidates are split up into two groups, those that are associated with the primary vertex (PV) and those that are not associated with the primary vertex (NPV); the latter can be used as an estimate of the pile-up contribution for the neutral particle flow candidates by taking the ratio $\Delta\beta$ of charged to neutral hadron production in the hadronization process of pile-up interactions into account. The resulting muon isolation is given by

$$Iso = \frac{\sum p_T^{\text{charged, PV}} + \max \left[0, \sum p_T^{\text{neutral had}} + \sum p_T^{\gamma} - \frac{1}{\Delta\beta} \sum p_T^{\text{charged, NPV}} \right]}{p_T}. \quad (4.16)$$

The average ratio of charged to neutral hadron production is $\Delta\beta \approx 2$, so the correction from charged contributions inconsistent with the primary vertex is multiplied with 0.5. The performance of the $\Delta\beta$ correction is comparable to that of an effective area correction; unlike the effective area method, the $\Delta\beta$ method makes it possible to use the same event to compute the correction, making an additional run period dependent area calculation unnecessary.

5

Search for Physics Beyond the Standard Model in the Opposite-Sign Same-Flavor Dilepton Final State

This Chapter describes a search [95–97] for physics beyond the Standard Model (BSM) in final states with two opposite-sign same-flavor leptons, jets and missing transverse energy, in a sample of 8 TeV pp collisions collected by the CMS experiment at the Large Hadron Collider. The size of the data sample corresponds to an integrated luminosity of 19.4 fb^{-1} . Standard Model backgrounds are estimated using data control samples. Two different approaches are taken: a counting experiment at low dilepton mass, and a search for a kinematic edge in the dilepton (e^+e^- , $\mu^+\mu^-$) mass distribution using a fit procedure.

Leptons are reconstructed as electrons and muons, since they provide a clean signature with low background. After selecting events with jets and an opposite-sign same-flavor lepton pair, the dominant SM backgrounds consist of Z + jets and top pair production ($t\bar{t}$). The relative importance of the backgrounds depends on the selection.

Some backgrounds, such as top pair production, produce electrons and muons with equal probability and therefore evenly populate the same-flavor and opposite-flavor dilepton final states; backgrounds with this property are referred to as flavor symmetric processes. The number of events in the e^+e^- and $\mu^+\mu^-$ final states can be estimated by using the events in the $e^\pm\mu^\mp$ final state and a transfer factor. Considering the same-flavor final state instead of the e^+e^- and $\mu^+\mu^-$ final states separately has the advantage of reducing the systematic uncertainties on the transfer factor, but it reduces the sensitivity of the analysis in BSM flavor symmetric models as well as BSM models where the production cross-section times branching fraction of these two same-flavor final states differ.

The transfer factor used in the estimate is derived from data control samples based on two independent methods, leading to a very robust combined estimate of flavor symmetric processes. In the event of an observation or discovery, it will be crucial to demonstrate that an excess is not due to a reconstruction bias; an additional cross-check factoring out trigger effects is therefore proposed and carried out to establish the absence of such a bias.

Not all backgrounds are flavor symmetric; the Z + jets process predominantly populates the same-flavor final state (except for events with leptonically decaying taus). The missing transverse energy in Z + jets events arises primarily due to jet energy resolution and reconstruction effects. Two independent methods based on data control samples are used to provide a combined estimate for the Z/γ^* background.

Further backgrounds, though very small, are also considered, such as backgrounds containing non-prompt leptons (which are estimated using several methods) and rare backgrounds.

The Chapter is organized as follows: the samples and event selection are discussed in Section 5.1. The signal and control regions are defined in Section 5.2, followed by a discussion of the background estimates in Section 5.3. In addition to the counting experiment, the background estimates are used as additional inputs for a fit to the dilepton mass spectrum in a search for a kinematic edge in Section 5.4. The results of the counting experiment and the fit are summarized in Section 5.5 and interpreted in Section 5.6.

5.1 Samples and Event Selection

5.1.1 Event Preselection

The event preselection is based on the object reconstruction outlined in Chapter 4.

The set of leptons (electrons or muons) passing the selection criteria is sorted according to their respective transverse momentum. The highest p_T lepton is selected as the “leading lepton”, and a second lepton (“sub-leading lepton”) is sought among the remaining leptons such that the leading and sub-leading lepton form an opposite-sign dilepton pair. In case of multiple sub-leading lepton candidates, the highest p_T candidate is selected. The two leptons are required to be spatially separated by $\Delta R > 0.3$ to avoid systematic effects due to isolation requirements. Furthermore, since the muon and electron reconstruction efficiencies are significantly different in the barrel-endcap transition region, leptons in the pseudorapidity range $1.4 < |\eta| < 1.6$ are rejected.

Jets are required to have $p_T > 40$ GeV and to be located in $|\eta| < 3.0$. Jets located within a cone of $\Delta R < 0.4$ around a selected lepton are rejected to avoid energy double-counting. Finally, the missing transverse momentum E_T^{miss} is defined as the magnitude of the vector sum of the transverse momenta of all PF objects.

A preselection is made requiring the presence of two opposite-sign leptons with an invariant mass $m_{\ell\ell} > 20$ GeV and at least two jets with $p_T > 40$ GeV. The selection criteria are summarized in Tab. 5.1.

Table 5.1: Summary of object definitions and selections for the search and control regions (for a more detailed description of the different objects see Chap. 4).

Object	Definition
Electron	$ \eta < 1.4$ or $1.6 < \eta < 2.4$, “loose” ID, isolated
Muon	$ \eta < 1.4$ or $1.6 < \eta < 2.4$, “tight” ID, isolated
Jet	particle-flow, anti- k_T with $R = 0.5$, $p_T > 40$ GeV, $ \eta < 3$
E_T^{miss}	uncorrected neg. vector sum of all particle-flow candidates

Selection	Definition
Lepton p_T	> 20 GeV
e-isolation	Iso < 0.15 , using $\Delta R < 0.3$, pile-up corrected
μ -isolation	Iso < 0.15 , using $\Delta R < 0.3$, pile-up corrected
Lepton $ \eta $	central: both $ \eta < 1.4$ forward: at least one $ \eta > 1.6$

Table 5.2: Triggers used in the analysis (top) and for control samples (bottom), including their thresholds.

Triggers used in the analysis	
Trigger	Trigger requirement(s)
Double-Electron	$p_{\text{T}}^{(1)} > 17 \text{ GeV} , p_{\text{T}}^{(2)} > 8 \text{ GeV}$
Double-Muon	$p_{\text{T}}^{(1)} > 17 \text{ GeV}$ or $p_{\text{T}}^{(1)} > 13 \text{ GeV} , p_{\text{T}}^{(2)} > 8 \text{ GeV}$
Electron-Muon	$p_{\text{T}}^{(1)} > 17 \text{ GeV} , p_{\text{T}}^{(2)} > 8 \text{ GeV}$
Control samples	
Trigger	Trigger requirement(s)
Single-Electron	$p_{\text{T}} > 27 \text{ GeV}$
Single-Muon	$p_{\text{T}} > 24 \text{ GeV}$
H_{T}	H_{T} requirements between 200 GeV and 750 GeV

5.1.2 Data Sample

The data used in the analysis was collected using dilepton triggers, i.e. triggers recording events with (at least) two leptons. The trigger decision is, however, based on trigger primitive objects (see Sec. 3.2.7), which are optimized for fast trigger decisions, and therefore differ from the objects used in the analysis. The difference in object definition could lead to cases where the trigger primitive object for a given event does not satisfy the trigger threshold whereas the analysis object would (e.g. due to energy corrections); the event would not be recorded for such cases even though the analysis would expect it to be present, leading to an inefficiency. The threshold used in the analysis is therefore increased with respect to the corresponding trigger threshold; the analysis threshold has been validated to ensure that such inefficiencies are avoided. An orthogonal reference trigger based on the scalar sum of transverse momenta of energy-corrected jets, H_{T} , is used to calculate the trigger efficiencies in Sec. 5.3.2, and additional triggers are used for control samples. An overview of the triggers used in the analysis and for control samples, along with the trigger thresholds, is given in Tab. 5.2.

The data was recorded between April and December of 2012; the luminosity is shown in Fig. 5.1 as a function of time, along with the luminosity delivered by the LHC. The data is divided into four data taking periods, called 2012A through 2012D, which differ from each other by their run conditions (such as pile-up). The different run periods are distinguishable in Fig. 5.2, which illustrates the peak

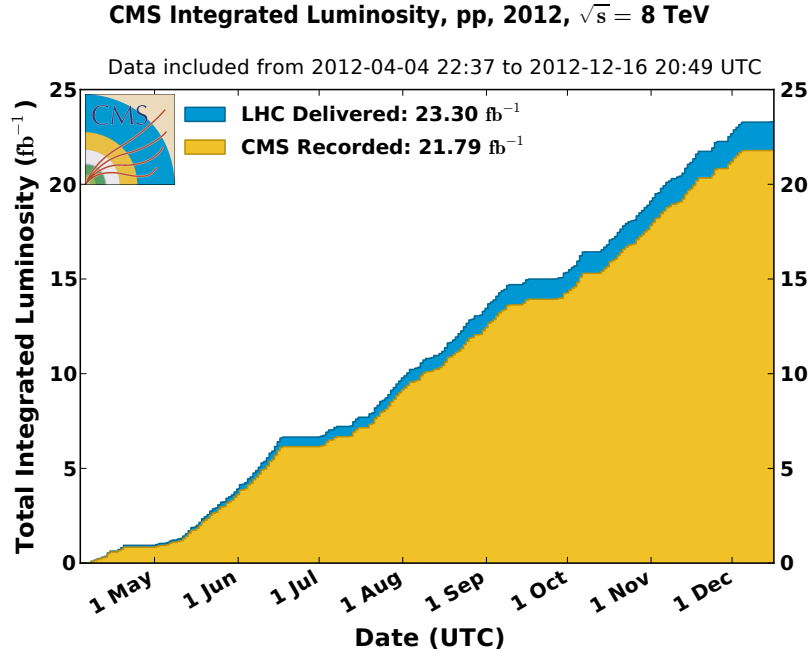


Figure 5.1: Cumulative luminosity delivered (blue) to and recorded (orange) by CMS during stable beams, as a function of time [88].

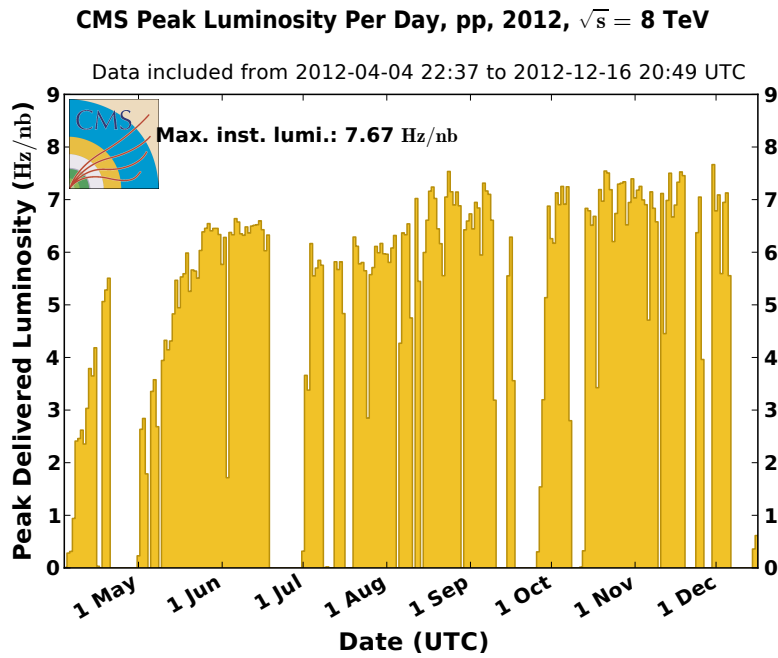


Figure 5.2: Peak luminosity per day recorded by CMS during stable beams, as a function of time; the different data taking periods are visible: the first ranges from early to mid-April (2012A), the second from early May to mid-June (2012B), the third from July 1 to mid-September (2012C), and the last from late September to late December (2012D) [88].

luminosity per day as a function of time; the peak luminosity varied significantly over the course of time and between run periods. After acquisition, the raw collision data is centrally checked and data taken during periods with working trigger and sub-detectors is certified. The total integrated luminosity used in the analysis presented in this Chapter is 19.4 fb^{-1} [98–102].

5.1.3 Simulated Events

While the main SM backgrounds are estimated from data control samples (see Sec. 5.3), Monte Carlo (MC) simulation samples are used to guide the design of the methods and provide cross-checks.

The MADGRAPH 5.1.3.30 [103] package is used to generate simulated events for $Z + \text{jets}$, $t\bar{t}$, $W + \text{jets}$, VV , and $t\bar{t}V$ ($V = W, Z$). The $Z + \text{jets}$ sample includes events with dilepton invariant masses down to 10 GeV , as well as decays to the $\tau\tau$ final state. The generation of parton showers is handled by PYTHIA 6.4.22 [104], and the detector response in the samples is simulated with a GEANT4 model [105] of the CMS detector; the reconstruction and analysis utilize the same software for collision data events and simulated events.

Multiple proton interactions are superimposed on the hard collisions in MC simulation, and the simulated samples are reweighted to describe the distribution of reconstructed primary vertices in data. The Monte Carlo simulation is also reweighted to account for differences between data and simulation in reconstruction, trigger efficiencies, and the top p_T spectrum. Next-to-leading order (NLO) cross-sections, or higher orders if available (for $Z + \text{jets}$ and $W + \text{jets}$ ¹), are used to normalize the simulated samples to an integrated luminosity of 19.4 fb^{-1} .

The dilepton invariant mass distributions for same-flavor (SF) and opposite-flavor (OF) lepton pairs after the preselection (and a requirement of at least 3 jets) are shown for data and Monte Carlo simulated samples in Fig. 5.3.

¹ Note that $V + \text{jets}$ is only known to NLO whereas inclusive Z and W production are known to NNLO; the $V + \text{jets}$ samples are reweighted to the inclusive NNLO cross-section.

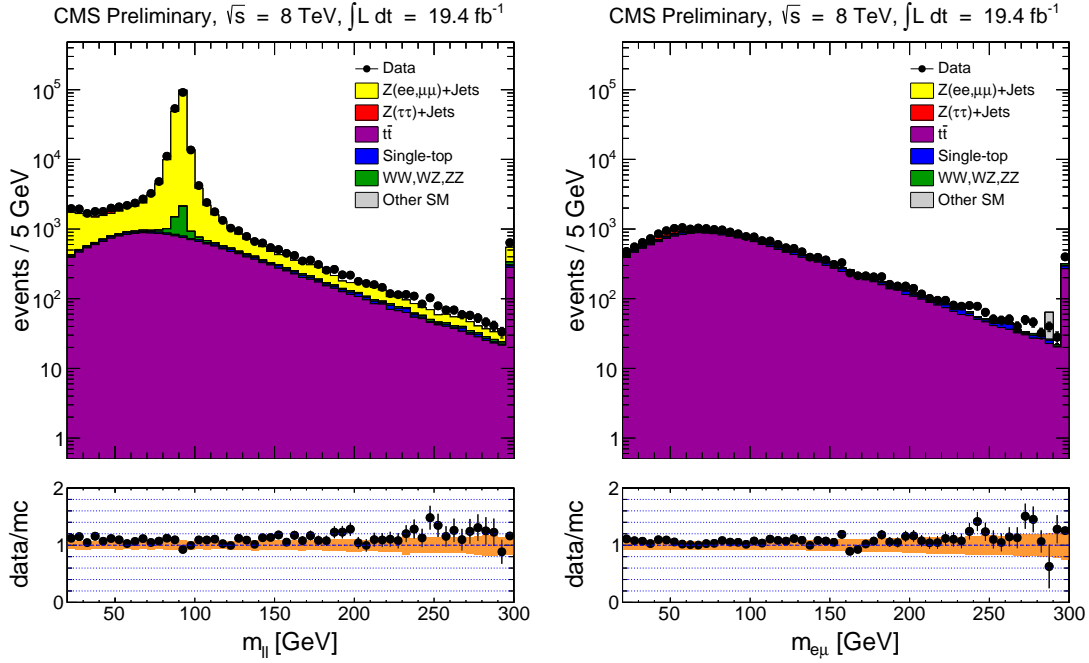


Figure 5.3: Opposite-sign same-flavor (left) and opposite-sign opposite-flavor (right) dilepton mass distributions in data and Monte Carlo simulation, in events with ≥ 3 jets. The bottom plots show the ratio between data and Monte Carlo simulation, and the orange band represents the systematic uncertainty from Jet Energy Scale calibration, pile-up re-weighting, and the $t\bar{t}$ cross-section.

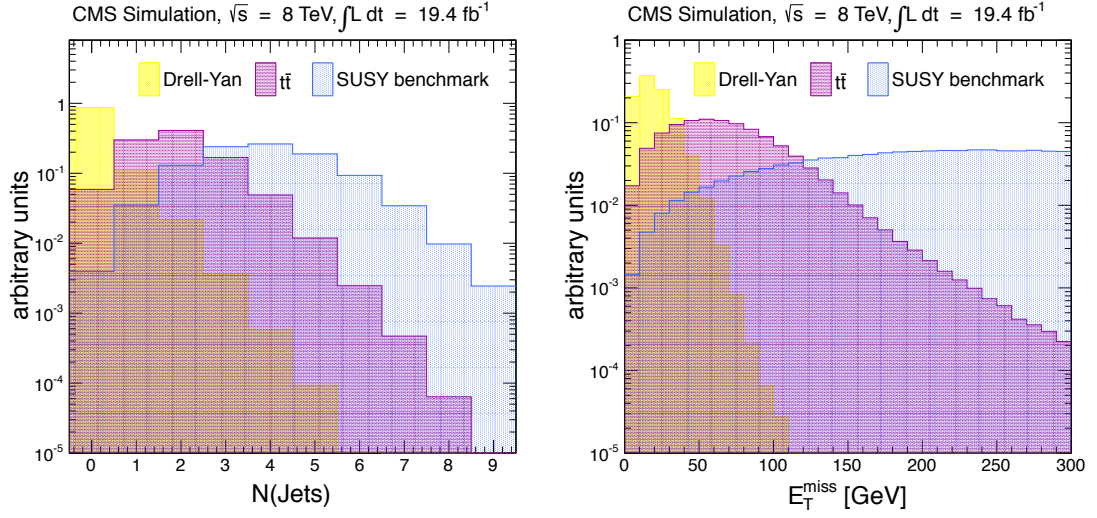


Figure 5.4: Jet multiplicity (left) and E_T^{miss} (right) shape (normalized to unit area) in opposite-sign same-flavor dilepton events (without any jet multiplicity or E_T^{miss} requirement) for the dominant backgrounds and a SUSY benchmark point; the Standard Model processes tend to have lower jet multiplicity and lower E_T^{miss} than the SUSY benchmark model.

5.2 Signal and Control Regions

New heavy particles in processes beyond the Standard Model typically decay in cascades (whose nature depends on the mass hierarchy of the involved particles); due to the emission of quarks and gluons, these processes are accompanied by large jet multiplicities. Furthermore, unobserved weakly interacting particles produced in the cascade cause an imbalance in the transverse plane and therefore large E_T^{miss} . Standard Model processes are therefore expected to have, in comparison, lower jet multiplicity and E_T^{miss} ; these distributions are shown in Fig. 5.4 for $Z + \text{jets}$, $t\bar{t}$, and the sample benchmark point introduced in Sec. 2.4.1.

These general considerations lead to the definition of signal and control regions based on the jet multiplicity and E_T^{miss} .

Signal Region

In order to make full use of the discriminating power of the jet multiplicity and E_T^{miss} , the signal region consists of the union of two sets of requirements reducing the main Standard Model backgrounds. In addition, the search is done separately

for events with two central leptons ("central region") and for events with at least one lepton in the detector endcaps ("forward region"). The requirements for the two resulting regions are:

- ($E_T^{\text{miss}} > 100 \text{ GeV}$ and ≥ 3 jets) or ($E_T^{\text{miss}} > 150 \text{ GeV}$ and ≥ 2 jets);
- central region: both leptons with $|\eta_{\text{lep}}| < 1.4$;
forward region: at least one lepton with $1.6 < |\eta_{\text{lep}}| < 2.4$.

All events in the dilepton mass range $[20, 300] \text{ GeV}$ enter the construction of the likelihood used in the fit (documented in Sec. 5.4) whereas the range for the counting experiment is restricted to the low-mass region $20 \text{ GeV} < m_{\ell\ell} < 70 \text{ GeV}$.

Control Regions

A control region close to the signal region is defined as containing events with exactly two jets and E_T^{miss} in the range $[100, 150] \text{ GeV}$. The region is largely dominated by top pair production whereas other SM backgrounds (as well as BSM signals) are suppressed. Since the control region is adjacent to the signal region, the lepton kinematics (p_T , η and $\Delta R(\ell_1, \ell_2)$) are also very close to those in the signal region, whereas the $t\bar{t}$ acceptance is slightly higher than in the signal region (by about 20%). Possible reconstruction or trigger biases in the flavor symmetric background estimate as well as $Z + \text{jets}$ contributions in the signal region would also affect and therefore be observed in this region.

An additional Drell-Yan enriched control region is defined as containing events having two or more jets, but limited missing transverse momentum ($E_T^{\text{miss}} < 50 \text{ GeV}$) in order to increase Drell-Yan (DY) purity and suppress the $t\bar{t}$ contribution. The DY-enriched control region is used for determining the relative efficiency of electrons and muons in one of the methods to determine the flavor symmetric background estimate (see Sec. 5.3.2) as well as to compute the extrapolation factor to the low mass region in the DY estimate (see Sec. 5.3.3). It is also used to obtain the shape of the DY background for the fit (documented in Sec. 5.4).

The location of the signal and control regions in terms of E_T^{miss} and the number of jets is illustrated in Fig. 5.5.

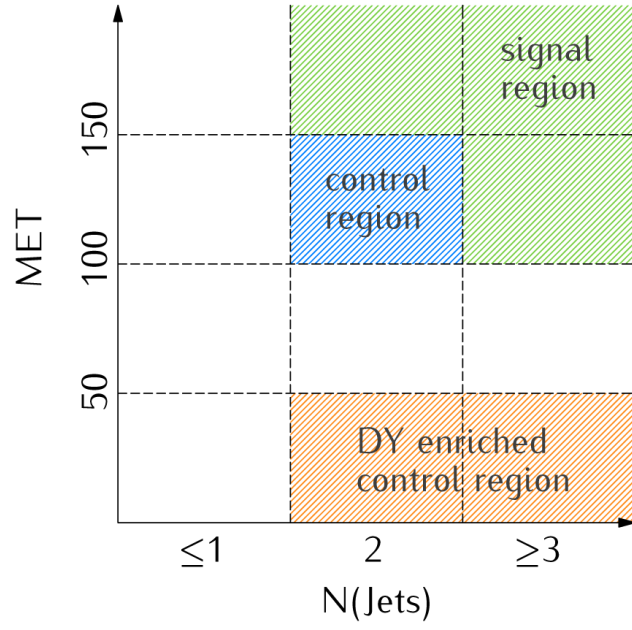


Figure 5.5: Illustration of the signal and control regions used in the analysis, with the signal region (green) occupying the region at high E_T^{miss} and high jet multiplicity, the adjacent main control region (blue) having reduced jet multiplicity and E_T^{miss} , and the DY-enriched control region (orange) at low E_T^{miss} .

5.3 Background Estimation

This Section focuses on the different methods employed to determine the backgrounds in the analysis. An overview is given in Sec. 5.3.1, followed by the different estimates, starting with the flavor symmetric backgrounds in Sec. 5.3.2, Drell-Yan in Sec. 5.3.3, backgrounds with non-prompt leptons in Sec. 5.3.4, and the estimate of rare backgrounds in Sec. 5.3.5. The predictions are summarized in Sec. 5.3.6.

5.3.1 Overview

The backgrounds in the signal region can be divided into four different categories:

- (i) Backgrounds that produce opposite-flavor pairs ($e^+\mu^-$, $e^-\mu^+$) and same-flavor pairs (e^+e^- , $\mu^+\mu^-$) with equal probability are referred to as “flavor symmetric backgrounds”. This category is dominated by top pair production processes.
- (ii) Backgrounds with two same-flavor leptons from a Z boson are referred to as “ Z backgrounds”. This category is dominated by Standard Model Z + jets production, where E_T^{miss} can come e.g. from mismeasured calorimetric energy.
- (iii) Backgrounds due to non-prompt leptons: these are backgrounds that contain a lepton that does not originate from a prompt decay (e.g. leptons not from a W or a Z). W + jets and $t\bar{t}$ are the main contributors in this category, whereas QCD multijet production is negligible (which will be shown in Sec. 5.3.4).
- (iv) Backgrounds from very rare processes (such as $t\bar{t}W$) are referred to as “rare backgrounds”. The main contribution stems from $t\bar{t}Z$.

The SM background yields expected from MC simulation in the central and forward signal regions are summarized in Tab. 5.3. The backgrounds (except for rare backgrounds) are estimated exclusively based on data control samples.

5.3.2 Flavor Symmetric Backgrounds

Flavor symmetric processes, such as $t\bar{t}$, $Z \rightarrow \tau\tau$, WW , and single top production, have equal contributions to the $(e^+e^-, \mu^+\mu^-)$ and $e^\pm\mu^\mp$ final states at particle level (i.e. before trigger and reconstruction effects). The contribution of the flavor symmetric background to the SF signal region can therefore be estimated based on the statistically independent OF data control sample collected using $e^\pm\mu^\mp$ triggers. The OF sample accurately describes the flavor symmetric background in the SF sample, provided that the same phase space (p_T^{lep} , η^{lep} , N_{jets} , E_T^{miss}) is considered.

Table 5.3: SM background yields expected for 19.4 fb^{-1} from MC simulation after the event selection.

	central	forward
$t\bar{t}$	622	127
DY + jets (e^+e^- , $\mu^+\mu^-$)	8	4
DY + jets ($\tau\tau$)	59	13
single-top	55	6
WW , ZZ , WZ	40	11
$t\bar{t}W$, $t\bar{t}Z$	8	2
W + jets	<1.4	<1

The symmetry between the SF and OF sample can be affected by trigger and reconstruction effects, potentially introducing a bias in the extrapolation. Since these effects can affect electrons and muons differently, the individual extrapolations to electrons and muons may also be biased.

The flavor symmetric background yield in same-flavor events is estimated based on opposite-flavor events via a transfer factor (“ R ratio”),

$$\begin{aligned}
 N_{ee} &= R(ee/OF) \times N_{OF} \\
 N_{\mu\mu} &= R(\mu\mu/OF) \times N_{OF} \\
 N_{SF} &\equiv N_{ee} + N_{\mu\mu} = R(SF/OF) \times N_{OF} .
 \end{aligned} \tag{5.1}$$

The factors at particle level (before any final state radiation), R^p , are simply

$$\begin{aligned}
 R^p(ee/OF) &= 0.5 \\
 R^p(\mu\mu/OF) &= 0.5 \\
 R^p(SF/OF) &= 1.0.
 \end{aligned} \tag{5.2}$$

A similar set of equations can be obtained at reconstruction level (i.e. after trigger and reconstruction effects) by using the reconstruction and trigger efficiencies to link the number of events at particle level, N^p , to the number of triggered events at reconstruction level, N ,

$$\begin{aligned}
 N_{ee} &= \epsilon_{ee}^{\text{reco.}} \epsilon_{ee}^{\text{trig.}} N_{ee}^p \\
 N_{\mu\mu} &= \epsilon_{\mu\mu}^{\text{reco.}} \epsilon_{\mu\mu}^{\text{trig.}} N_{\mu\mu}^p \\
 N_{OF} = N_{e\mu} + N_{\mu e} &= \epsilon_{e\mu}^{\text{reco.}} \epsilon_{e\mu}^{\text{trig.}} N_{e\mu}^p + \epsilon_{\mu e}^{\text{reco.}} \epsilon_{\mu e}^{\text{trig.}} N_{\mu e}^p .
 \end{aligned}$$

In the following, the average trigger efficiency for OF, defined as

$$\epsilon_{OF}^{trig} = \frac{\epsilon_{e\mu}^{trig} + \epsilon_{\mu e}^{trig}}{2} ,$$

is used, so the final transfer factors are given by

$$\begin{aligned} R(ee/OF) &= \frac{N_{ee}}{N_{OF}} = \frac{\epsilon_{ee}^{reco.} \epsilon_{ee}^{trig.}}{\epsilon_{OF}^{reco.} \epsilon_{OF}^{trig.}} \underbrace{\frac{N_{ee}^p}{N_{OF}^p}}_{R^p(ee/OF)} = \frac{\epsilon_{ee}^{reco.} \epsilon_{ee}^{trig.}}{2 \epsilon_{OF}^{reco.} \epsilon_{OF}^{trig.}} \\ R(\mu\mu/OF) &= \frac{N_{\mu\mu}}{N_{OF}} = \frac{\epsilon_{\mu\mu}^{reco.} \epsilon_{\mu\mu}^{trig.}}{\epsilon_{OF}^{reco.} \epsilon_{OF}^{trig.}} \underbrace{\frac{N_{\mu\mu}^p}{N_{OF}^p}}_{R^p(\mu\mu/OF)} = \frac{\epsilon_{\mu\mu}^{reco.} \epsilon_{\mu\mu}^{trig.}}{2 \epsilon_{OF}^{reco.} \epsilon_{OF}^{trig.}} \\ R(SF/OF) &= \frac{N_{ee} + N_{\mu\mu}}{N_{OF}} = \frac{\epsilon_{ee}^{reco.} \epsilon_{ee}^{trig.}}{\epsilon_{OF}^{reco.} \epsilon_{OF}^{trig.}} \underbrace{\frac{N_{ee}^p}{N_{OF}^p}}_{R^p(ee/OF)} + \frac{\epsilon_{\mu\mu}^{reco.} \epsilon_{\mu\mu}^{trig.}}{\epsilon_{OF}^{reco.} \epsilon_{OF}^{trig.}} \underbrace{\frac{N_{\mu\mu}^p}{N_{OF}^p}}_{R^p(\mu\mu/OF)} \\ &= \frac{\epsilon_{ee}^{reco.} \epsilon_{ee}^{trig.} + \epsilon_{\mu\mu}^{reco.} \epsilon_{\mu\mu}^{trig.}}{2 \epsilon_{OF}^{reco.} \epsilon_{OF}^{trig.}} . \end{aligned} \quad (5.3)$$

These equations demonstrate the complex link between efficiencies and transfer factors.

An alternative way to write the transfer factors involves the relative efficiency $r_{\mu e}$ [106],

$$r_{\mu e} \equiv \sqrt{\frac{N_{\mu\mu}}{N_{ee}}} = \sqrt{\frac{\epsilon_{\mu\mu}^{reco.} \epsilon_{\mu\mu}^{trig.}}{\epsilon_{ee}^{reco.} \epsilon_{ee}^{trig.}}} ,$$

with which equations (5.3) can be rewritten as

$$\begin{aligned} R(ee/OF) &= \frac{\epsilon_{ee}^{reco.} \epsilon_{ee}^{trig.}}{2 \epsilon_{OF}^{reco.} \epsilon_{OF}^{trig.}} = \frac{1}{2} \underbrace{\sqrt{\frac{\epsilon_{ee}^{reco.} \epsilon_{ee}^{trig.}}{\epsilon_{\mu\mu}^{reco.} \epsilon_{\mu\mu}^{trig.}}}}_{r_{\mu e}^{-1}} \underbrace{\sqrt{\frac{\epsilon_{\mu\mu}^{reco.} \epsilon_{\mu\mu}^{trig.}}{\epsilon_{OF}^{reco.} \epsilon_{OF}^{trig.}}}}_{R_T} = \frac{1}{2} r_{\mu e}^{-1} \cdot R_T \\ R(\mu\mu/OF) &= \frac{\epsilon_{\mu\mu}^{reco.} \epsilon_{\mu\mu}^{trig.}}{2 \epsilon_{OF}^{reco.} \epsilon_{OF}^{trig.}} = \frac{1}{2} \underbrace{\sqrt{\frac{\epsilon_{\mu\mu}^{reco.} \epsilon_{\mu\mu}^{trig.}}{\epsilon_{ee}^{reco.} \epsilon_{ee}^{trig.}}}}_{r_{\mu e}} \underbrace{\sqrt{\frac{\epsilon_{ee}^{reco.} \epsilon_{ee}^{trig.}}{\epsilon_{OF}^{reco.} \epsilon_{OF}^{trig.}}}}_{R_T} = \frac{1}{2} r_{\mu e} \cdot R_T \\ R(SF/OF) &= R(ee/OF) + R(\mu\mu/OF) = \frac{1}{2} (r_{\mu e}^{-1} + r_{\mu e}) R_T , \end{aligned} \quad (5.4)$$

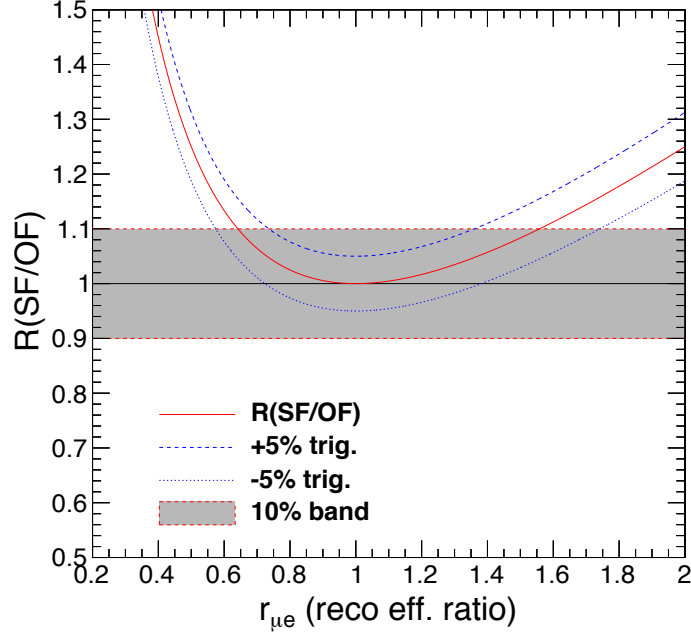


Figure 5.6: Stability of $R(\text{SF}/\text{OF})$ with respect to $r_{\mu e}$. The effect of a 5% uncertainty on R_T is also shown.

where the additional quantity R_T has been defined as

$$R_T \equiv 2 \frac{\sqrt{N_{ee} N_{\mu\mu}}}{N_{OF}} = \frac{\sqrt{\epsilon_{ee}^{\text{reco.}} \epsilon_{ee}^{\text{trig.}} \epsilon_{\mu\mu}^{\text{reco.}} \epsilon_{\mu\mu}^{\text{trig.}}}}{\epsilon_{OF}^{\text{reco.}} \epsilon_{OF}^{\text{trig.}}} . \quad (5.5)$$

This alternative parametrization in terms of $r_{\mu e}$ and R_T underlines the advantage of using the combined SF sample compared to the separate e^+e^- and $\mu^+\mu^-$ samples. While the separate transfer factors (i.e. $R(ee/OF)$ and $R(\mu\mu/OF)$) are directly affected by the differences in reconstruction and trigger efficiencies by the factors $r_{\mu e}$ or $r_{\mu e}^{-1}$, these differences partially cancel out in $R(\text{SF}/\text{OF})$. The effect of a variation of $r_{\mu e}$ on $R(\text{SF}/\text{OF})$ is illustrated in Fig. 5.6: a value of $r_{\mu e}$ as large as 1.20 only leads to a value of $R(\text{SF}/\text{OF})$ of about 1.02. The same cancellation also applies to the uncertainty on $r_{\mu e}$; this cancellation is the most striking feature of $R(\text{SF}/\text{OF})$.

The equations (5.3) and (5.4) open the door to two independent approaches for the calculation of the R ratios:

- (i) Control region approach: the transfer factors in (5.3) can be measured in the data control region defined in Sec. 5.2, which is close in phase space to the signal region;
- (ii) Factorization approach: $r_{\mu e}$ is measured in the DY-enriched control region (defined in Sec. 5.2), and R_T in an independent data control sample collected with independent triggers; the transfer factors can then be determined using equation (5.4).

While the second approach offers greater statistical power, the first method provides smaller systematic uncertainties since the measurements are carried out in a control region directly adjacent to the signal region.

Both independent approaches are presented below, and the results from both methods are combined in Sec. 5.3.2.3 to obtain the final result.

5.3.2.1 Control Region Approach

The transfer factors may depend on the dilepton mass and are therefore measured in 5 mass bins ($[20, 70]$, $[70, 120]$, $[120, 170]$, and $[170, 500]$ GeV), which are defined in such a way that the event yields in each bin are always at least 40, and thus approximately follow a Gaussian distribution.

Due to the proximity in phase space, the kinematics of the control region are very similar to those of the signal region; the differences in the transfer factors between the two are studied in the following using $t\bar{t}$ Monte Carlo simulation, which accounts for the vast majority of the flavor symmetric background. The transfer factors are derived for each mass bin based on the event yields in each final state in $t\bar{t}$ Monte Carlo simulation in the control and signal region. A set of ratios RR is introduced, which relate the transfer factors measured in the signal region (SR) to the measured values in the control region (CR),

$$\begin{aligned} RR(\text{SF}/\text{OF}) &= \frac{R(\text{SF}/\text{OF})[\text{SR}]}{R(\text{SF}/\text{OF})[\text{CR}]} \\ RR(ee/\text{OF}) &= \frac{R(ee/\text{OF})[\text{SR}]}{R(ee/\text{OF})[\text{CR}]} \\ RR(\mu\mu/\text{OF}) &= \frac{R(\mu\mu/\text{OF})[\text{SR}]}{R(\mu\mu/\text{OF})[\text{CR}]} \end{aligned}$$

Table 5.4: Measured values of ratios relating the transfer factor in the signal region to the transfer factor in the control region, using $t\bar{t}$ MC simulation; the values are indicated for the central (top) and forward (bottom) selection.

central	$m_{\ell\ell} \in [20, 70]$	$m_{\ell\ell} \in [70, 120]$	$m_{\ell\ell} \in [120, 170]$	$m_{\ell\ell} > 170 \text{ GeV}$
$RR(\text{SF}/OF)$	1.02 ± 0.01	1.00 ± 0.01	1.00 ± 0.02	1.03 ± 0.02
$RR(\mu\mu/OF)$	1.02 ± 0.02	0.97 ± 0.01	0.96 ± 0.02	0.97 ± 0.02
$RR(ee/OF)$	1.01 ± 0.02	1.04 ± 0.02	1.05 ± 0.02	1.11 ± 0.02
forward	$m_{\ell\ell} \in [20, 70]$	$m_{\ell\ell} \in [70, 120]$	$m_{\ell\ell} \in [120, 170]$	$m_{\ell\ell} > 170 \text{ GeV}$
$RR(\text{SF}/OF)$	1.01 ± 0.03	0.98 ± 0.02	1.03 ± 0.03	0.96 ± 0.03
$RR(\mu\mu/OF)$	1.02 ± 0.04	0.95 ± 0.03	1.00 ± 0.03	0.86 ± 0.03
$RR(ee/OF)$	1.01 ± 0.04	1.03 ± 0.03	1.08 ± 0.04	1.11 ± 0.04

The values of these ratios for the central and forward regions are indicated in Tab. 5.4.

The measured values of the transfer factors are shown in Fig. 5.7. While there is a visible dependence of $R(ee/OF)$ and $R(\mu\mu/OF)$ on $m_{\ell\ell}$ in MC simulation, $R(\text{SF}/OF)$ does not show any clear trend, which is the result of the compensation between $R(ee/OF)$ and $R(\mu\mu/OF)$. In data, the statistical uncertainty covers the $m_{\ell\ell}$ dependence to a large extent.

The application of the transfer factors can either be universal (i.e. the values of the transfer factors are fixed to the ones measured in the $m_{\ell\ell} \in [20, 70]$ GeV bin) or mass-dependent (i.e. the values of the transfer factors depend on $m_{\ell\ell}$). While the mass-dependent efficiency correction has a large impact on $R(ee/OF)$ and $R(\mu\mu/OF)$ at high mass, $R(\text{SF}/OF)$ has no noticeable $m_{\ell\ell}$ dependence (even in MC simulation), and the universal efficiency correction procedure is therefore adopted (for more detailed information see [96]).

The quantities measured in the $[20, 70]$ GeV region are summarized in Tab. 5.5 for the central region and in Tab. 5.6 for the forward region. The values of the alternative parametrization variables ($r_{\mu e}$, R_T) have also been measured in the control region to allow for a direct comparison with the results obtained in the factorization method in Sec. 5.3.2.2.

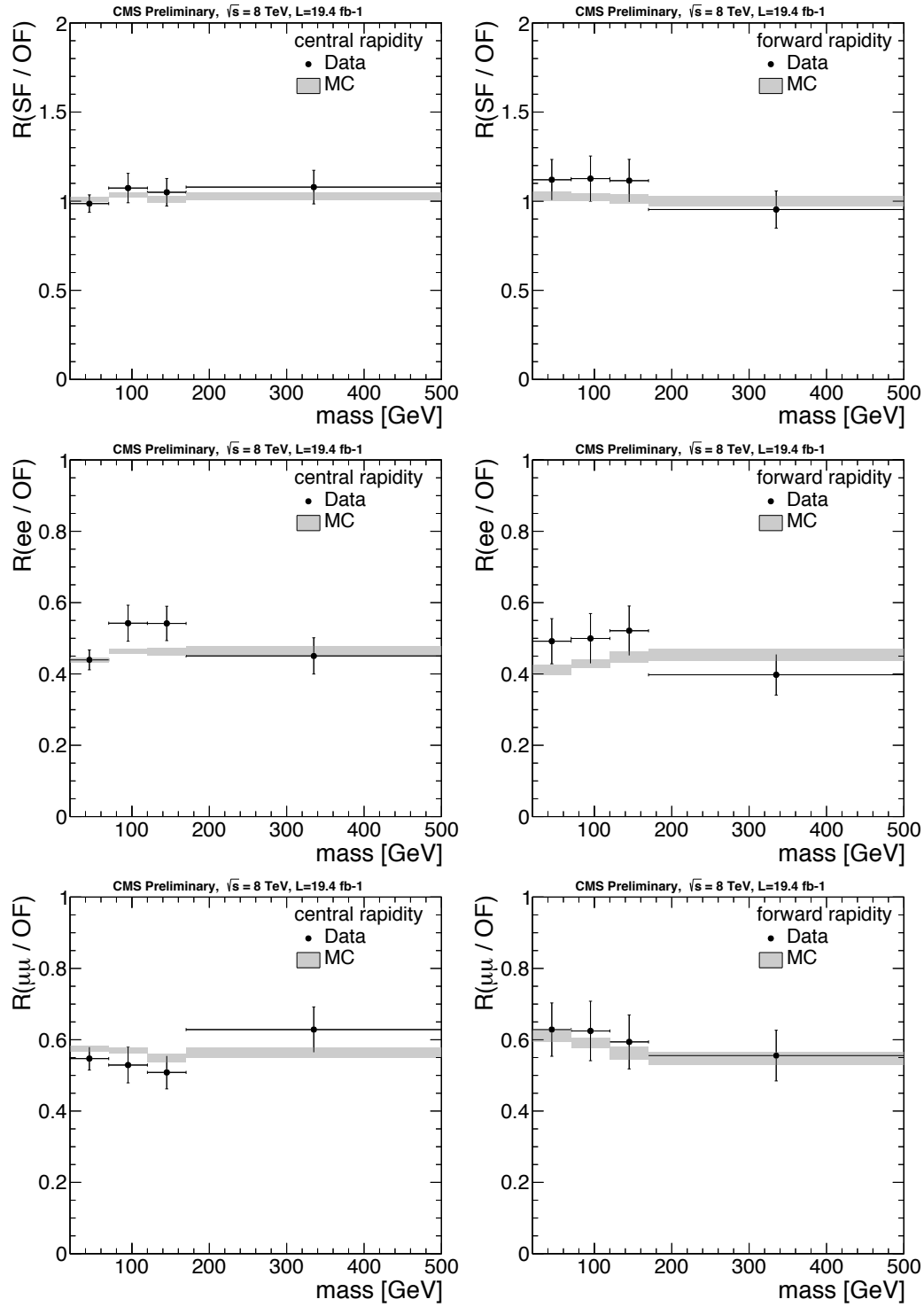


Figure 5.7: Measured values of $R(\text{SF}/\text{OF})$ (top), $R(\text{ee}/\text{OF})$ (middle), and $R(\mu\mu/\text{OF})$ (bottom) in data and $t\bar{t}$ MC simulation in the control region, as a function of the dilepton invariant mass. The left plots correspond to the central region; the right plots correspond to the forward region.

Table 5.5: Summary table for the central control region and $m_{\ell\ell} \in [20, 70]$ GeV.

	Data	MC
$R(SF/OF)[CR]$	$0.99 \pm 0.05 \pm 0.02$	1.01 ± 0.01
$R(\mu\mu/OF)[CR]$	$0.55 \pm 0.03 \pm 0.01$	0.574 ± 0.009
$R(ee/OF)[CR]$	$0.44 \pm 0.03 \pm 0.01$	0.439 ± 0.007
$r_{\mu e}[CR]$	1.12 ± 0.04	1.15 ± 0.01
$R_T[CR]$	0.98 ± 0.05	1.00 ± 0.01

Table 5.6: Summary table for the forward control region and $m_{\ell\ell} \in [20, 70]$ GeV.

	Data	MC
$R(SF/OF)[CR]$	$1.11 \pm 0.11 \pm 0.03$	1.03 ± 0.03
$R(\mu\mu/OF)[CR]$	$0.62 \pm 0.07 \pm 0.02$	0.61 ± 0.02
$R(ee/OF)[CR]$	$0.49 \pm 0.06 \pm 0.02$	0.41 ± 0.01
$r_{\mu e}[CR]$	1.13 ± 0.08	1.22 ± 0.02
$R_T[CR]$	1.11 ± 0.11	1.01 ± 0.03

5.3.2.2 Factorization Approach

The second method to determine the transfer factors is based on the alternative parametrization (using the $r_{\mu e}$ and R_T variables).

Determining $r_{\mu e}$

The sample used to derive $r_{\mu e}$ is the DY-enriched control sample defined in Sec. 5.2. Two or more jets are required in order to be sufficiently close in phase space to the signal region. An upper cut on E_T^{miss} at 50 GeV is used to suppress the $t\bar{t}$ contribution and to make the region statistically independent from the control region in which the transfer factors are measured directly.

The systematic uncertainty on $r_{\mu e}$ is assessed by studying a mix of simulated samples consisting of DY + jets and $t\bar{t}$. The mass dependence of $r_{\mu e}$ is illustrated in Fig. 5.8 for the DY-enriched control region and the signal region. A small trend can be observed in the signal region (which is dominated by $t\bar{t}$). Furthermore, a variation in $r_{\mu e}$ due to differences in the momentum scale between electrons and muons as well as some differences in physical processes (e.g. final state radiation) is observed. A systematic uncertainty of 10% (20%) for the central (forward) region is assigned in order to account for these effects (the dependence on the number of

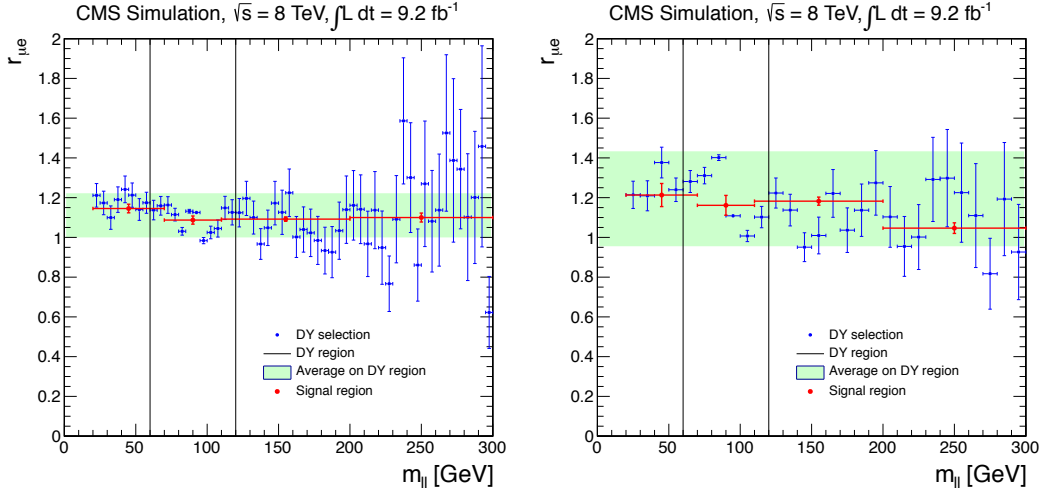


Figure 5.8: $r_{\mu e}$ values in a mix of MC simulated samples (consisting of $t\bar{t}$ and DY + jets) as a function of the invariant mass, for the central (left) and forward (right) selection. The red points represent the values obtained in the signal region selection (without a cut on $m_{\ell\ell}$), whereas the blue points correspond to the DY-enriched control region (without the $m_{\ell\ell}$ requirement) in which $r_{\mu e}$ is measured. The green band is centered at the $r_{\mu e}$ value obtained in the DY-enriched control region in the mass range $60 < m_{\ell\ell} < 120$ GeV (black box), the width of the band corresponds to the 10% (20%) uncertainty for the central (forward) selection.

jets, E_T^{miss} , and $m_{\ell\ell}$ has also been studied in data [97], with the same conclusions). The measured values are shown in Tab. 5.7.

Determining R_T

The second parameter, R_T , is measured in an orthogonal event sample collected with H_T triggers. By assuming that the reconstruction efficiencies between the two leptons are uncorrelated (which is valid if the opening angle between the leptons is not too small), equation (5.5) simplifies to

$$R_T^x = \frac{\sqrt{\epsilon_{ee}^{\text{trig.}} \epsilon_{\mu\mu}^{\text{trig.}}}}{\epsilon_{OF}^{\text{trig.}}} . \quad (5.6)$$

The efficiencies entering R_T^x are determined in a control region characterized by a requirement of $H_T > 200$ GeV (due to the selected H_T trigger thresholds), an invariant mass of $m_{\ell\ell} > 20$ GeV, and no explicit requirements on the jet multiplicity or E_T^{miss} . Any events contained in the signal region or the previous control region

are rejected from this sample to maintain statistical independence.

The dilepton trigger efficiencies in the H_T control region, $\epsilon^{\text{trig}, H_T}$, are computed as the ratio of the number of events simultaneously passing the H_T and dilepton triggers as well as the offline selection, divided by the number of events passing only the H_T trigger and the offline selection,

$$\epsilon^{\text{trig}, H_T} = \frac{N(H_T^{\text{trigger}} \wedge \text{OfflineSelection} \wedge \text{DoubleLepton}^{\text{trigger}})}{N(H_T^{\text{trigger}} \wedge \text{OfflineSelection})}. \quad (5.7)$$

The trigger efficiencies are measured in data and MC simulation. Since the H_T sample contains a mixture of $DY + \text{jets}$ and $t\bar{t}$ events that represent a potentially different phase space from the one considered in the signal region, the extrapolation to the signal region is determined using MC simulation,

$$\epsilon_{\text{data}}^{\text{trig}} = \epsilon_{\text{data}}^{\text{trig}, H_T} \cdot \left(\frac{\epsilon_{\text{MC}}^{\text{trig}, \text{SR}}}{\epsilon_{\text{MC}}^{\text{trig}, H_T}} \right). \quad (5.8)$$

The systematic bias, $\epsilon_{\text{MC}}^{\text{trig}, \text{SR}}/\epsilon_{\text{MC}}^{\text{trig}, H_T}$, obtained by this procedure is added to the systematic uncertainty. This bias is negligible in the central region and is of the order of 3% in the forward region, where both values refer to the $[20, 70]$ GeV mass bin. The dependence on the invariant mass, jet multiplicity, and E_T^{miss} was also studied [97], and an average systematic uncertainty of 5% is assigned to cover all effects related to the difference in phase space between the control sample and the signal region. The measured values are summarized in Tab. 5.7, and can be compared with the direct control region measurements in Tab. 5.5 and Tab. 5.6.

Table 5.7: Measured values of the parameters of the alternative parametrization ($r_{\mu e}$, trigger efficiencies, R_T), and final values. The letters in brackets indicate the control sample(s) used for the measurements.

	central	forward
$\epsilon_{ee} [H_T]$	$0.97 \pm 0.00 \pm 0.05$	$0.97 \pm 0.01 \pm 0.05$
$\epsilon_{\mu\mu} [H_T]$	$0.97 \pm 0.01 \pm 0.05$	$0.97 \pm 0.01 \pm 0.05$
$\epsilon_{e\mu} [H_T]$	$0.94 \pm 0.01 \pm 0.05$	$0.88 \pm 0.03 \pm 0.04$
$R(\text{SF}/\text{OF}) [DY, H_T]$	$1.03 \pm 0.01 \pm 0.06$	$1.11 \pm 0.04 \pm 0.08$
$R(ee/\text{OF}) [DY, H_T]$	$0.47 \pm 0.01 \pm 0.06$	$0.46 \pm 0.02 \pm 0.10$
$R(\mu\mu/\text{OF}) [DY, H_T]$	$0.56 \pm 0.01 \pm 0.07$	$0.65 \pm 0.03 \pm 0.14$
$r_{\mu e} [DY]$	$1.09 \pm 0.00 \pm 0.11$	$1.18 \pm 0.00 \pm 0.24$
$R_T [H_T]$	$1.03 \pm 0.01 \pm 0.06$	$1.10 \pm 0.04 \pm 0.07$

5.3.2.3 Combination

The two measurements are combined using a weighted average. The measurements are assumed to be independent, since they are extracted from exclusive, non-overlapping samples. The final measurements are presented in Tab. 5.8. The agreement between the two methods is remarkably good. It is interesting to note that the two R_T measurements are consistent within uncertainties, as is expected in the factorization limit of the reconstruction efficiencies.

The combined $R(\text{SF}/\text{OF})$ values are:

- $R(\text{SF}/\text{OF}) = 1.00 \pm 0.04$ in the central region;
- $R(\text{SF}/\text{OF}) = 1.11 \pm 0.07$ in the forward region.

The final background prediction is calculated by multiplying the number of opposite-flavor events in the signal region selection by the corresponding transfer factors, as shown in Tab. 5.9.

Table 5.8: Transfer factors obtained for the central and forward regions by the two methods and their combination using a weighted average. The measured $r_{\mu e}$ and R_T values are also given.

	central	forward
Control region		
$R(\text{SF}/\text{OF})$	$0.99 \pm 0.05 \pm 0.02$	$1.11 \pm 0.11 \pm 0.03$
$R(ee/\text{OF})$	$0.44 \pm 0.03 \pm 0.01$	$0.49 \pm 0.06 \pm 0.02$
$R(\mu\mu/\text{OF})$	$0.55 \pm 0.03 \pm 0.01$	$0.62 \pm 0.07 \pm 0.02$
$r_{\mu e}$	$1.116 \pm 0.040(\text{stat.})$	$1.124 \pm 0.079(\text{stat.})$
R_T	$0.979 \pm 0.049(\text{stat.})$	$1.106 \pm 0.112(\text{stat.})$
DY + jets and H_T regions		
$R(\text{SF}/\text{OF})$	$1.03 \pm 0.01 \pm 0.06$	$1.11 \pm 0.04 \pm 0.08$
$R(ee/\text{OF})$	$0.47 \pm 0.01 \pm 0.061$	$0.46 \pm 0.02 \pm 0.102$
$R(\mu\mu/\text{OF})$	$0.56 \pm 0.01 \pm 0.07$	$0.65 \pm 0.03 \pm 0.14$
$r_{\mu e}$	$1.09 \pm 0.00 \pm 0.11$	$1.18 \pm 0.00 \pm 0.24$
R_T	$1.03 \pm 0.01 \pm 0.062$	$1.10 \pm 0.04 \pm 0.07$
Combined		
$R(\text{SF}/\text{OF})$	1.00 ± 0.04	1.11 ± 0.07
$R(ee/\text{OF})$	0.45 ± 0.03	0.48 ± 0.05
$R(\mu\mu/\text{OF})$	0.55 ± 0.04	0.63 ± 0.07

Table 5.9: Estimate of the flavor symmetric background yields in the signal regions. The top row shows the raw OF yields, the following rows show the estimates after correcting the raw yield with the appropriate transfer factor.

	central	forward
OF yield	722	140
Flav. Sym. Bkgd (SF)	$722 \pm 27 \pm 29$	$155 \pm 13 \pm 10$
Flav. Sym. Bkgd (ee)	$325 \pm 12 \pm 22$	$67 \pm 6 \pm 7$
Flav. Sym. Bkgd ($\mu\mu$)	$397 \pm 15 \pm 22$	$88 \pm 7 \pm 10$

5.3.2.4 $Z \rightarrow \tau\tau$

The $Z \rightarrow \tau\tau$ process can lead to neutrinos and leptons in the final state; since the neutrinos carry some of the energy, the invariant mass of the two leptons is smaller than that of the Z boson, and the events populate the low mass range (i.e. the signal region). It is therefore important to study whether the method also holds for this background. The contribution from this background is only at the 5% level of the total flavor symmetric background (according to Monte Carlo simulation), so in order to increase the number of events for a more detailed study, the jet multiplicity and E_T^{miss} requirements were loosened to $E_T^{\text{miss}} > 50$ GeV and $N_{\text{jets}} \geq 2$.

The dilepton mass distributions for same-flavor and opposite-flavor events are illustrated in Fig. 5.9; the transfer factor $R(\text{SF}/\text{OF})$ is found to be consistent with 1.0 within MC statistical uncertainties. The $Z \rightarrow \tau\tau$ component of the DY + jets process is therefore covered by the flavor symmetric estimate.

5.3.2.5 Cross-Check with Uncorrelated Leptons Using WZ Events

It will be important to demonstrate that any putative excess is not due to a reconstruction bias. Therefore, in addition to the two previously presented methods, a cross-check has been developed that factors out trigger effects entirely.

The transfer factor $R(\text{SF}/\text{OF})$ can be measured in WZ events, where both the W and the Z boson decay leptonically, and the single-lepton trigger is fired by the highest p_T lepton coming from the Z . In this case, the two remaining leptons are uncorrelated in flavor and are not subject to any trigger effects and therefore permit an unbiased measurement of $R(\text{SF}/\text{OF})$.

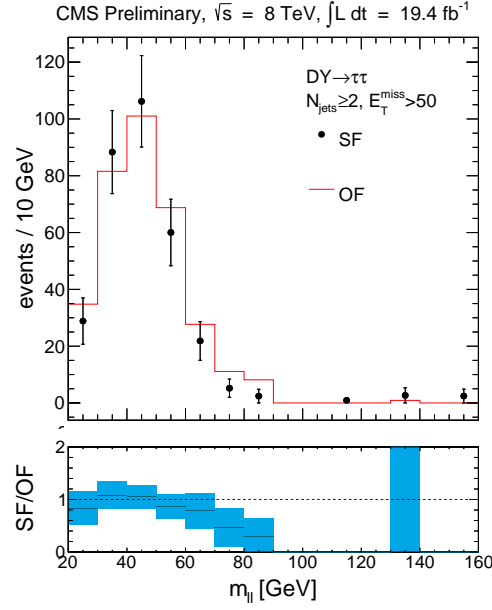


Figure 5.9: SF and OF yields as a function of $m_{\ell\ell}$ for $Z \rightarrow \tau\tau$ events, and the corresponding $R(SF/OF)$ value, for events with $N_{\text{jets}} \geq 2$ and $E_T^{\text{miss}} > 50$ GeV.

The data sample for the study was collected with single-lepton triggers. Events with three p_T ordered leptons, each satisfying $p_T > 20$ GeV, are selected. The leading p_T lepton fired a single lepton trigger and is also required to satisfy $p_T > 30$ GeV. The second lepton is chosen such that it forms an opposite-sign, same-flavor pair with the first lepton (the first two leptons therefore form the Z boson candidate). If multiple leptons satisfy the requirement, the lepton combination with the dilepton mass closest to that of the Z boson is chosen. If no lepton is found to make an opposite-sign same-flavor combination with the first lepton, the event is rejected. The remaining highest p_T lepton is the third lepton.

The second and third leading leptons of such events are used in the following, and the terms “same-flavor” and “opposite-flavor” refer to the relative flavor of these two sub-leading leptons.

The WZ purity, defined as the number of WZ events in the same-flavor final state compared to the total number of events in the same-flavor final state, is about 25% after the preselection, with the remainder being dominated by $Z + \text{jets}$ events. The main source of the $Z + \text{jets}$ background are $\mu\mu e$ events (due to Bremsstrahlung), which can be reduced significantly by imposing a requirement on the tripleton mass ($|m_{\ell_1\ell_2\ell_3} - m_Z| > 30$ GeV). The properties of the third lepton are exploited by

considering the transverse mass of the W ,

$$m_T = \sqrt{2E_T^{\text{miss}} p_T^{(3)} \cdot (1 - \cos \phi(\vec{E}_T^{\text{miss}}, \vec{p}_T^{(3)}))}, \quad (5.9)$$

where $p_T^{(3)}$ is the transverse momentum of the third lepton. A requirement of $m_T > 40 \text{ GeV}$ further enhances the WZ purity. The presence of neutrinos coming from the W decay is exploited by requiring the presence of missing transverse energy ($E_T^{\text{miss}} > 30 \text{ GeV}$), and the first two leptons are required to form a dilepton mass roughly compatible with the Z mass ($|m_{\ell_1 \ell_2} - m_Z| < 10 \text{ GeV}$).

The WZ purity increases from 25% (in the preselection) to about 88% in the final selection. Since the $ZZ \rightarrow 4\ell$ process also produces two uncorrelated leptons, the relevant purity² is even higher (approximately 94%).

The selection was tested at MC truth level, where a ratio of $R(\text{SF}/\text{OF}) = 1.01 \pm 0.01$ was obtained, leading to the conclusion that the selection does not bias the ratio.

Combinatorial Background

The WZ process also contains a non-flavor symmetric component from events where the lepton from the W fires the trigger and forms an opposite-sign SF pair with a lepton from the Z . In that case, both the second and third lepton are from the Z and are therefore correlated. In order to reduce the impact of these events, the sub-leading dilepton mass is required to be inconsistent with the Z mass ($|m_{\ell_2 \ell_3} - m_Z| > 5 \text{ GeV}$). The remaining effect has been assessed in MC simulation, and the results are shown in Tab. 5.10. The ratio of SF to OF events in a WZ MC sample is

$$R_{\text{comb}, WZ} = 1.055 \pm 0.009 \text{ (MC stat)}, \quad (5.10)$$

which is used to correct the final result in data.

Table 5.10: Number of SF and OF events in a WZ Monte Carlo sample and a subsample containing only correct combinations (i.e. first lepton from Z).

	All WZ events	Correct combination
Same flavor	233.8 ± 1.5	224.0 ± 0.8
opposite-flavor	221.6 ± 1.5	220.0 ± 0.8
$R(\text{SF}/\text{OF})$	1.055 ± 0.010	1.018 ± 0.010

²The relevant purity is the relative fraction of flavor symmetric events in the sample.

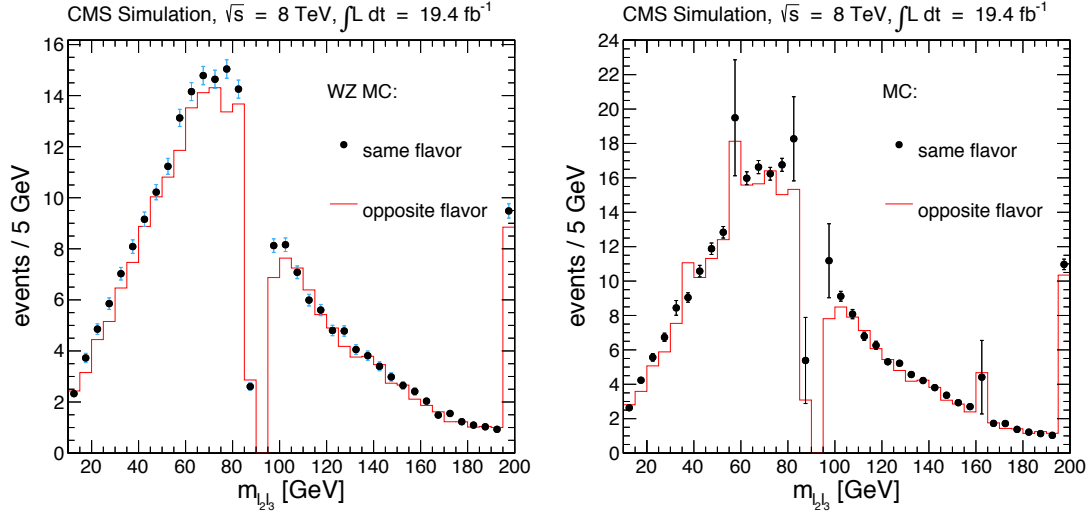


Figure 5.10: Comparison of the dilepton mass of the uncorrelated lepton pair in WZ MC (left), a mixture of all MC samples (right).

Results in Monte Carlo Simulation

The analysis is first carried out using a mix of all Monte Carlo simulated samples. A total of 277.8 SF and 260.5 OF events is found. The raw ratio is $R_{\text{raw}}^{\text{MC}}(SF/OF) = 1.066 \pm 0.009$ (MC stat), which needs to be corrected for the combinatorial factor $R_{\text{comb},WZ}$ from (5.10). The result in Monte Carlo simulation is therefore

$$R_{\text{corr}}^{\text{MC}}(SF/OF) = 1.01 \pm 0.01 \text{ (MC stat)} \pm 0.06 \text{ (sys)} .$$

Results in Data

When applying the method to data, 311 SF events and 318 OF events are found. The raw ratio is $R_{\text{raw}}^{\text{data}}(SF/OF) = 0.98 \pm 0.07$ (stat), after correcting for bad combinations from WZ through $R_{\text{comb},WZ}$ from (5.10), the result in data is

$$R_{\text{corr}}^{\text{data}}(SF/OF) = 0.93 \pm 0.07 \text{ (stat)} \pm 0.06 \text{ (sys)} .$$

The measurement of $R(SF/OF)$ is compatible with 1.0 and does not show any indication of a reconstruction effect.

The comparison of the dilepton mass of the uncorrelated lepton pair ($m_{\ell_2 \ell_3}$) for same-flavor and opposite-flavor is shown for WZ Monte Carlo simulation and the mix of all Monte Carlo simulated samples in Fig. 5.10 and data in Fig. 5.11. A

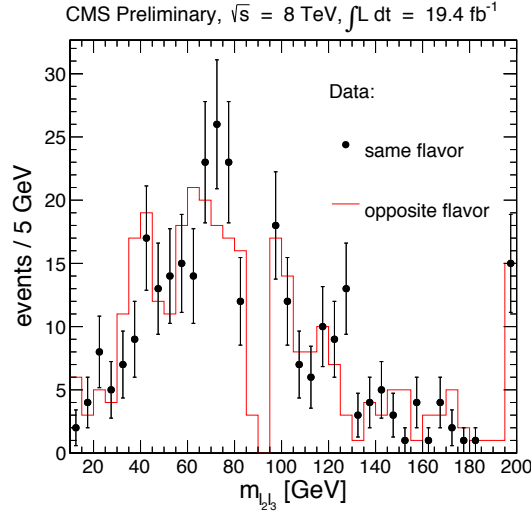


Figure 5.11: Comparison of the dilepton mass of the uncorrelated lepton pair in data.

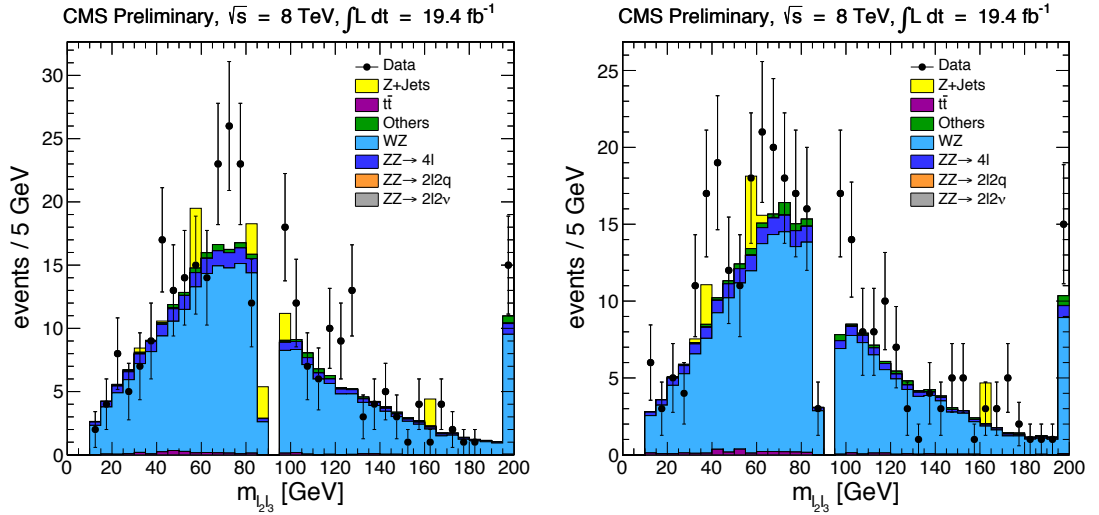


Figure 5.12: Data/MC comparison of the dilepton mass of the uncorrelated lepton pair for SF (left) and OF events (right)

data/MC comparison as a function of the dilepton mass of the uncorrelated lepton pair is shown in Fig. 5.12.

5.3.3 SM $Z + \text{jets}$

SM backgrounds with a reconstructed Z boson (mainly $Z + \text{jets}$, but also ZZ , WZ , $t\bar{t} Z$) are estimated using two data-driven methods: the Jet- Z balance (JZB) and E_T^{miss} templates methods [107].

The JZB method is summarized in Sec. 5.3.3.1, followed by its application to the E_T^{miss} spectrum in Sec. 5.3.3.2 to estimate the yield of SM Z events in the Z peak region ($81 \text{ GeV} < m_{\ell\ell} < 101 \text{ GeV}$), with all other selection criteria being the same as in the signal region. The second method to estimate the yield of SM Z events in the Z peak region, called the E_T^{miss} templates method, is summarized in Sec. 5.3.3.3. The extrapolation factor, $R_{\text{in/out}}$, relating the number of $Z + \text{jets}$ events in the signal mass region ($20 \text{ GeV} < m_{\ell\ell} < 70 \text{ GeV}$) to that in the Z peak region, is then derived in Sec. 5.3.3.4. Finally, the estimates in the Z peak region from the two different methods (JZB and E_T^{miss} templates) are combined and extrapolated to the low mass region in Sec. 5.3.3.5, leading to the final estimate of the $Z + \text{jets}$ background in the signal region.

5.3.3.1 The JZB Method

The JZB method [107] provides an estimate of the $Z + \text{jets}$ background by using the JZB variable, which measures the imbalance between the p_T of the Z boson candidate and the p_T of the hadronic system,

$$JZB = \left| -\sum_{\text{jets}} \vec{p}_T \right| - \left| \vec{p}_T^{(Z)} \right| \approx \left| -E_T^{\text{miss}} - \vec{p}_T^{(Z)} \right| - \left| \vec{p}_T^{(Z)} \right|. \quad (5.11)$$

In the simplest case, with only one jet, and E_T^{miss} due to detector reconstruction and resolution effects, the variable can be thought of as E_T^{miss} with additional sign information indicating the source of E_T^{miss} : while jet energy undermeasurements tend to lead to negative values, jet energy overmeasurements mostly lead to positive values of the JZB observable. The two cases are, however, not equiprobable, with undermeasurements being slightly more probable (due to energy losses), leading to larger negative tails.

The JZB distribution approximates a Gaussian distribution with increasing jet multiplicity; this is due to angular randomization of the mis-measured jet with respect to the direction of the Z boson candidate. The angular randomization leads to instrumental effects canceling each other out already in 3-jet events, where the most probable configuration is the one in which the 2 leading jets are back-to-back [108].

The method was devised to predict the E_T^{miss} contribution from $Z + \text{jets}$ events [109] and was first applied to data using 34 pb^{-1} of 7 TeV CMS data in 2010 [110], using equation (5.11) with a correction for the peak position (the same method was applied as well for the following result with 191 pb^{-1} of 7 TeV CMS data in 2011 [111]). An additional correction was introduced for the subsequent update in 2011 [112] to account for the reconstruction bias in the response, which was also used in the 7 TeV paper with the full dataset [107]. A further correction for the pile-up dependent offset in the peak position has been added since then, and the JZB method has been extended to provide a prediction for the E_T^{miss} distribution (described in Sec. 5.3.3.2) as well.

The corrections are explained in more detail in the following.

Response Correction

The hadronic recoil in the JZB variable is estimated by using the measured E_T^{miss} and subtracting the Z momentum. The response, defined as the ratio between the hadronic recoil and the momentum of the Z boson,

$$R_{JZB} = \frac{\left| -\vec{E}_T^{\text{miss}} - \vec{p}_T^{(Z)} \right|}{\left| \vec{p}_T^{(Z)} \right|}, \quad (5.12)$$

has been studied as a function of the p_T of the Z boson. A fit with a flat line to the response as a function of p_T is then carried out in the p_T range of $[100, 400] \text{ GeV}$; a reconstruction bias of 6% for data and 4% for Monte Carlo simulation is observed (see Fig. 5.13). While the correction has a negligible effect on the final event yields, it allows to recover the p_T invariance of the JZB peak position for large p_T , as can be seen in Fig. 5.14

Pile-up Dependent Peak Correction

Pile-up jets can lead to events from lower jet multiplicities entering the jet selection, leading to an imbalance and therefore a shift in the JZB distribution. To illustrate this effect, a selection with ≥ 3 jets is made and the selection is split into events with at least 3 jets from the hard collision and events with less than 3 jets from the hard collision (therefore containing at least one jet from pile-up). The corresponding JZB distributions are shown in Fig. 5.15, where a clear shift between the two can be observed.

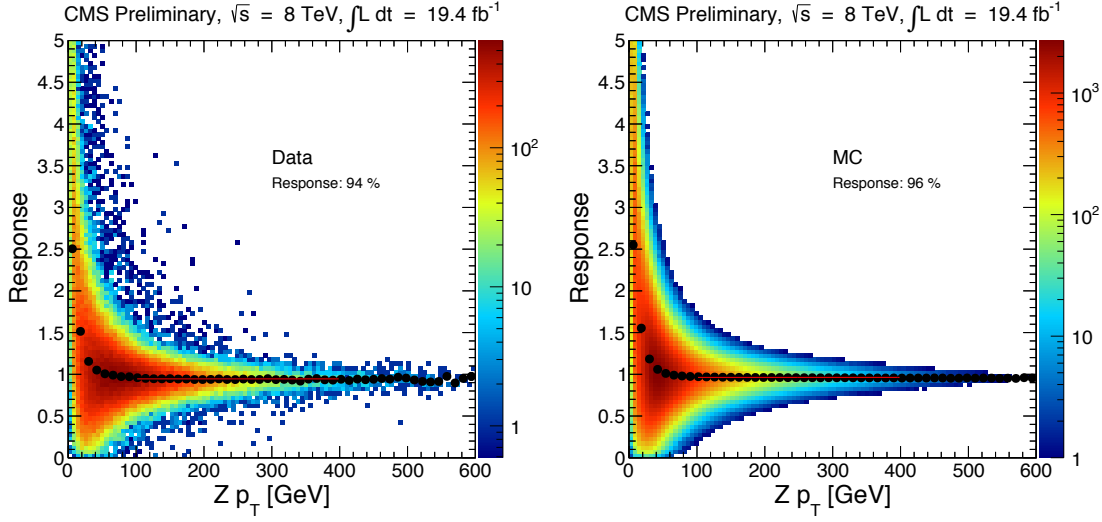


Figure 5.13: Response measured in data (left) and Monte Carlo simulation (right). The points show the profile of the 2D histogram. The red curve shows the result of a flat line fit to the [100,400] GeV region.

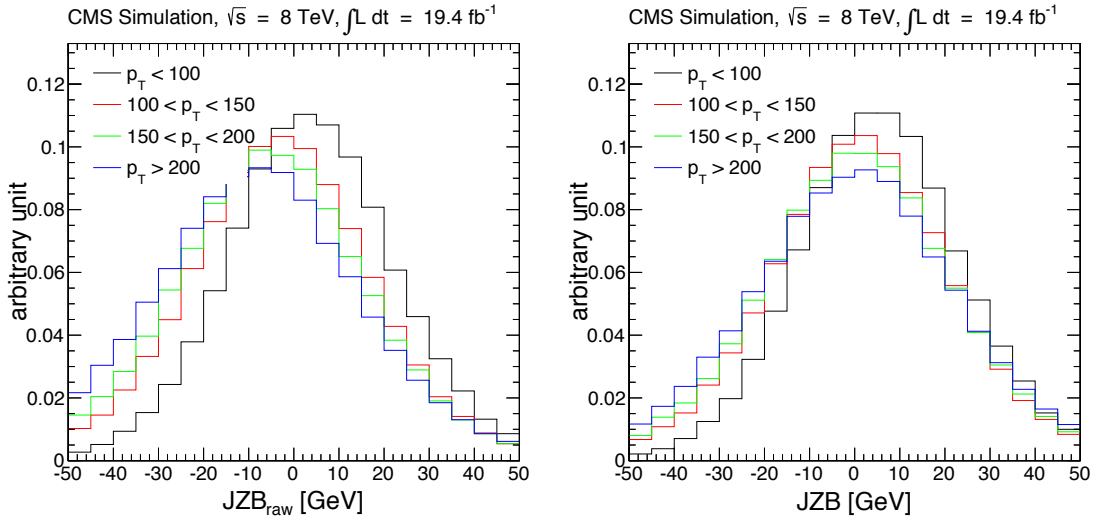


Figure 5.14: JZB distribution for several ranges in p_T of the Z boson candidate before the response correction (left) and after the response correction (right); the correction recovers the p_T invariance of the JZB peak position.

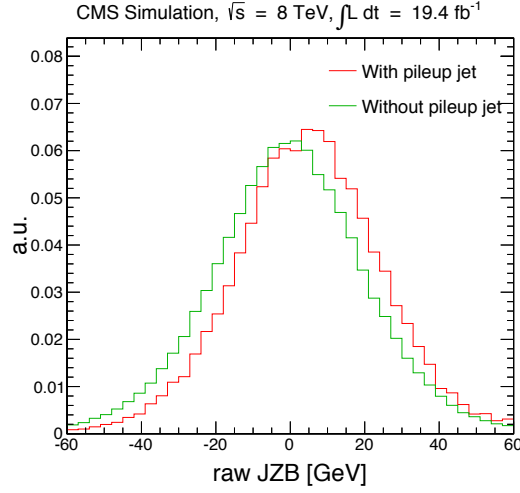


Figure 5.15: JZB distributions for a selection with at least three jets; one selection contains at least three jets from the hard collision (green) whereas the second contains less than three jets from the hard collision (red); events with less than three jets from the hard collision may still enter the selection due to additional jets present in the events. A clear shift between the distributions is visible.

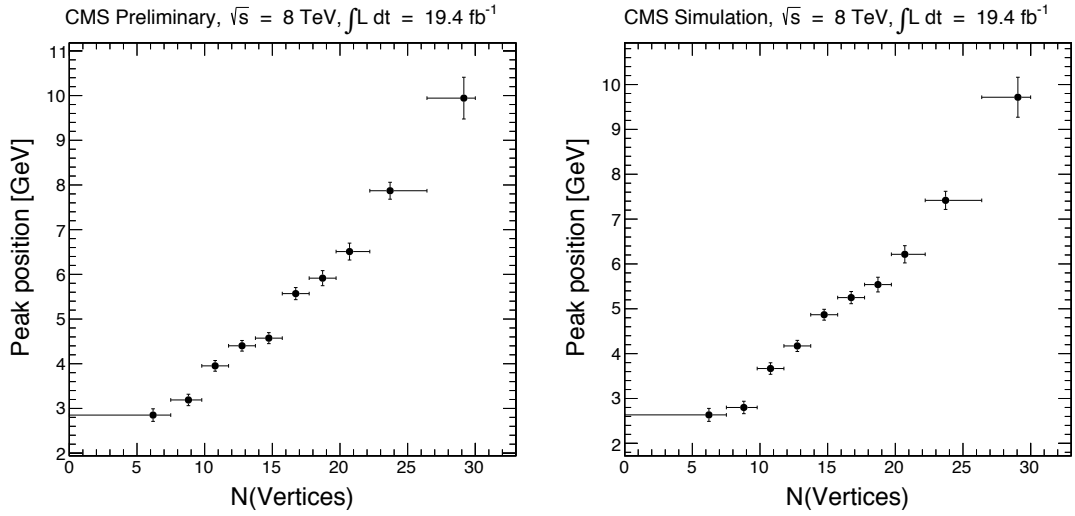


Figure 5.16: Peak position of the JZB distribution as a function of the number of vertices in the event, in data (left) and Monte Carlo simulation (right).

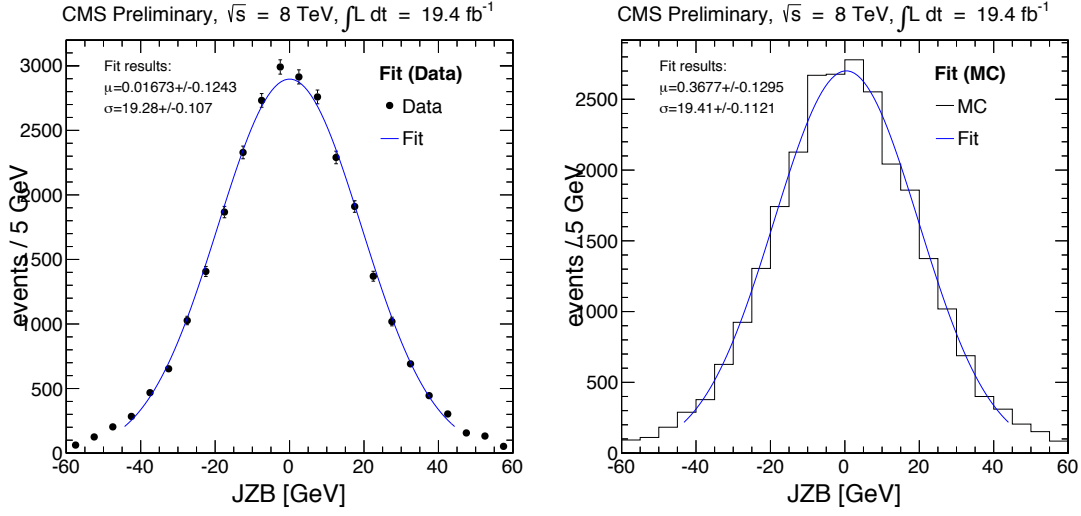


Figure 5.17: Fit to the response and pile-up corrected JZB distribution for data (left) and Monte Carlo simulated samples (right) to extract the peak correction.

The peak position of the JZB distribution is extracted by an iterative Gaussian fit to the core of the JZB distribution for different bins of the number of primary vertices. For the first iteration of each fit, σ is assumed to be 10 GeV and the initial peak position is set to the mean of the JZB distribution in the $[-60, 60]$ GeV range. The peak position after the iterative Gaussian fit is shown as a function of the number of primary vertices in Fig. 5.16, where a clear trend can be seen. The slope, extracted through a fit with a polynomial of degree one, is used as a pile-up correction term in the general JZB definition in addition to the resolution correction.

Peak Correction

The position of the peak of the JZB distribution is sensitive to the jet energy scale. In order to be robust against miscalibration of the jet energy scale, the position of the peak, μ , is used to redefine the origin of the JZB variable. The remaining peak position after the resolution and pile-up corrections is determined by an iterative Gaussian fit to the core of the JZB distribution in the $\mu \pm \sigma$ range (as in the pile-up dependent peak correction). The result of a fit to the core of the JZB distribution in data and Monte Carlo simulation is shown in Fig. 5.17. The final value of the correction is below a GeV.

Summary of Corrections

In summary, the response correction compensates the dependence of the peak on the transverse momentum of the Z candidate, while the pile-up correction does

Table 5.11: Typical values for the different corrections of the JZB distribution for data and Monte Carlo simulation.

correction	variable	value (data)	value (MC)
response correction	α	0.06	0.04
pile-up correction	β	0.30 GeV	0.27 GeV
peak correction	μ	0.02 GeV	0.37 GeV

the same as a function of the number of vertices. The peak is then invariant as a function of the momentum of the Z candidate and the number of vertices, and is shifted to zero by the peak correction. The fully corrected JZB variable is given by

$$JZB_{corr} = \underbrace{\left| -E_T^{\vec{miss}} - \vec{p}_T^{(\ell\ell)} \right| - \left| \vec{p}_T^{(\ell\ell)} \right|}_{JZB_{raw}} + \alpha p_T^{\ell\ell} - \beta N_{vtx} - \mu, \quad (5.13)$$

where α is the response correction, β is the slope of the peak correction as a function of the number of primary vertices (N_{vtx}) and μ is the residual global peak correction. Typical values of the corrections are given in Tab. 5.11 for data and Monte Carlo simulation.

The JZB estimate consists of two components, the Z + jets prediction and the flavor symmetric background estimate. The Z + jets background is estimated by the JZB method by considering the contribution to the left of the peak position to predict the one to the right of the peak position; for a given JZB requirement $JZB > X$, the estimate is therefore the contribution up to $JZB < -X$. The estimate needs to be corrected for flavor symmetric backgrounds to the left of the peak which would also enter the prediction; this leads to an additional term. The JZB Z + jets prediction is therefore

$$N_{Z\text{-pred}}(JZB > X) = N(\text{SF}, JZB < -X) - R(\text{SF}/\text{OF}) \cdot N(\text{OF}, JZB < -X). \quad (5.14)$$

The full prediction also needs to include flavor symmetric backgrounds to the right ($JZB > X$), therefore the full JZB estimate, for Z + jets and flavor symmetric backgrounds, is given by

$$N_{\text{pred}}(JZB > X) = N(\text{SF}, JZB < -X) - R(\text{SF}/\text{OF}) \cdot N(\text{OF}, JZB < -X) + R(\text{SF}/\text{OF}) \cdot N(\text{OF}, JZB > X). \quad (5.15)$$

The full estimate (5.15) was used in the previous preliminary searches for SUSY using the JZB method [107, 110–112] to obtain a robust prediction of the backgrounds as a function of the JZB variable. However, equation (5.14) can also be

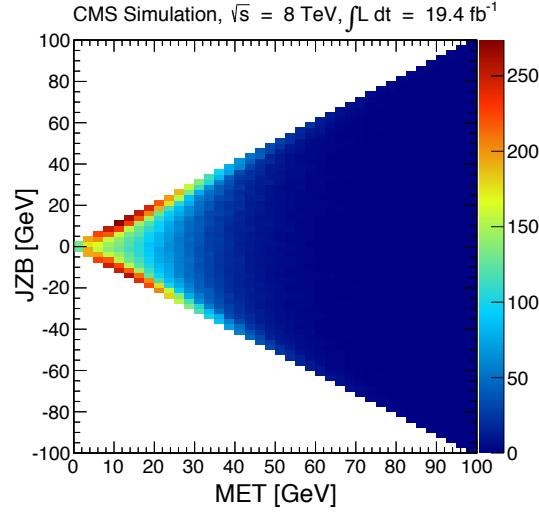


Figure 5.18: Illustration of the correlation between the raw JZB variable and E_T^{miss} : the raw JZB variable is bounded from above and below by E_T^{miss} .

used to derive a prediction of the $Z + \text{jets}$ background as a function of E_T^{miss} , which is discussed below.

5.3.3.2 E_T^{miss} prediction from JZB

Based on the definition of the raw JZB variable in equation (5.11), it is not only possible to derive an upper bound in terms of the missing transverse energy,

$$\text{JZB} \leq \sqrt{(E_T^{\text{miss}})^2 + 2E_T^{\text{miss}} p_T + (p_T)^2} - p_T = E_T^{\text{miss}},$$

but also lower bounds,

$$\text{if } p_T \geq E_T^{\text{miss}}: \quad \text{JZB} \geq \sqrt{(E_T^{\text{miss}})^2 - 2E_T^{\text{miss}} p_T + (p_T)^2} - p_T = -E_T^{\text{miss}}$$

$$\text{if } p_T \leq E_T^{\text{miss}}: \quad \text{JZB} \geq \sqrt{(E_T^{\text{miss}})^2 - 2E_T^{\text{miss}} p_T + (p_T)^2} - p_T = E_T^{\text{miss}} - 2p_T \geq -E_T^{\text{miss}}.$$

The absolute value of the JZB observable for a given event is therefore bounded by the value of the E_T^{miss} observable,

$$|\text{JZB}| \leq E_T^{\text{miss}},$$

where the sign of the JZB variable reflects the angle between the E_T^{miss} and the dilepton pair.

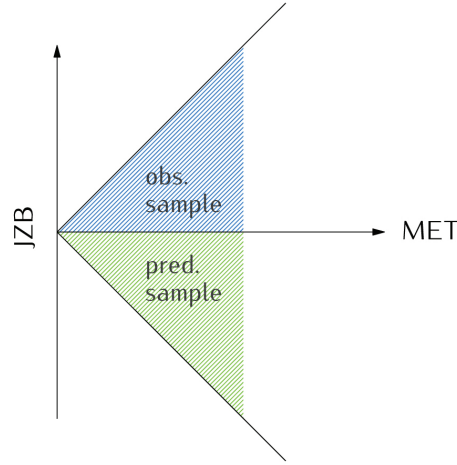


Figure 5.19: Illustration of the procedure to derive a Z prediction as a function of E_T^{miss} using the JZB variable: the JZB variable permits an even division of events into two subsamples (“observed” sample and “prediction” sample) due to the symmetry of the JZB distribution. The “prediction” sample can then be used to derive an estimate of the Z content of the “observed” sample.

The E_T^{miss} and JZB values are illustrated in Fig. 5.18 using a sample of simulated Drell-Yan events; the bounds on JZB are clearly visible. The fact that $Z + \text{jets}$ events evenly populate the left and right side of the JZB distribution can not only be used to predict the JZB distribution to the right of the peak by considering the distribution to the left of the peak (as discussed in Sec. 5.3.3.1), but the symmetry can also be used to obtain an estimate in terms of E_T^{miss} by splitting the sample into two subsamples,

- (i) “observed” sample: subsample containing all events to the right of the peak of the JZB distribution ($\text{JZB} > 0$);
- (ii) “prediction” sample: subsample used to compute the prediction, containing events to the left of the peak of the JZB distribution ($\text{JZB} < 0$).

The idea of splitting the sample using the JZB sign information is illustrated in Fig. 5.19. The Z estimate from equation (5.14) can therefore be reformulated in terms of E_T^{miss} to obtain an estimate of the Z background in the “observed” sample by using the “prediction” sample,

$$N_{Z\text{-pred}}(E_T^{\text{miss}} > X, \text{JZB} > 0) = N(\text{SF}, E_T^{\text{miss}} > X, \text{JZB} < 0) \\ - R(\text{SF}/\text{OF}) \cdot N(\text{OF}, E_T^{\text{miss}} > X, \text{JZB} < 0) . \quad (5.16)$$

A direct application of equation (5.16), however, leads to a mismatch between the E_T^{miss} spectra of the “observed” and “prediction” samples, which is due to the additional corrections present in equation (5.13). The E_T^{miss} distribution of the “prediction” sample is therefore modified using the ansatz

$$E_{T,\text{corr}}^{\text{miss}} = E_T^{\text{miss}} + \lambda \alpha p_T, \quad (5.17)$$

where α is the response correction discussed in Sec. 5.3.3.1, and λ is an additional parameter characterizing the modification. The E_T^{miss} spectrum in the “observed sample” is compared to the predicted E_T^{miss} distribution (including the modification) for different values of λ using a Drell-Yan sample in Fig. 5.20; the best value is found to be $\lambda = -1$ (note that $\lambda = 0$ leads back to the original E_T^{miss} distribution). The corrected variable is therefore

$$E_{T,\text{corr}}^{\text{miss}} = E_T^{\text{miss}} - \alpha p_T. \quad (5.18)$$

In spite of selecting the Z window for the prediction, the data sample does not only contain Z candidates but also other backgrounds. The additional backgrounds are also taken into consideration by adding the flavor symmetric estimate in analogy to Sec. 5.3.2 and equation (5.15).

The method has been tested using a sample of simulated Drell-Yan events; the predicted and observed E_T^{miss} spectra are shown Fig. 5.21. Excellent agreement is observed for the higher jet multiplicity selection, whereas the two jet selection also performs well; the higher jet multiplicity bin is expected to provide better agreement, since the JZB method approximates a Gaussian distribution only with increasing jet multiplicity (as explained in Sec. 5.3.3.1). The two jet bin is, however, far less relevant in the final prediction since the E_T^{miss} cut in this region is tighter (at $E_T^{\text{miss}} > 150$ GeV). A systematic uncertainty of 20% is assigned to cover residual differences in the high jet multiplicity selection, and a 30% uncertainty is assigned for the prediction with lower jet multiplicity.

The method has also been tested using a set of Monte Carlo simulated samples (illustrated in Fig. 5.22), where very good agreement has been observed. The method is then applied to data; the distributions are shown in Fig. 5.23.

The Z + jets component of the JZB-based estimate is given by

$$N_{Z+\text{jets}}^{\text{est}} = 2 \cdot (N_{e^+e^-} + N_{\mu^+\mu^-} - R(\text{SF/OF})N_{\text{OF}}), \quad (5.19)$$

where $N_{e^+e^-}$, $N_{\mu^+\mu^-}$, and N_{OF} are the yields in the “prediction sample”; the uncertainty on $R(\text{SF/OF})$ is also propagated to the estimate. The estimation from the

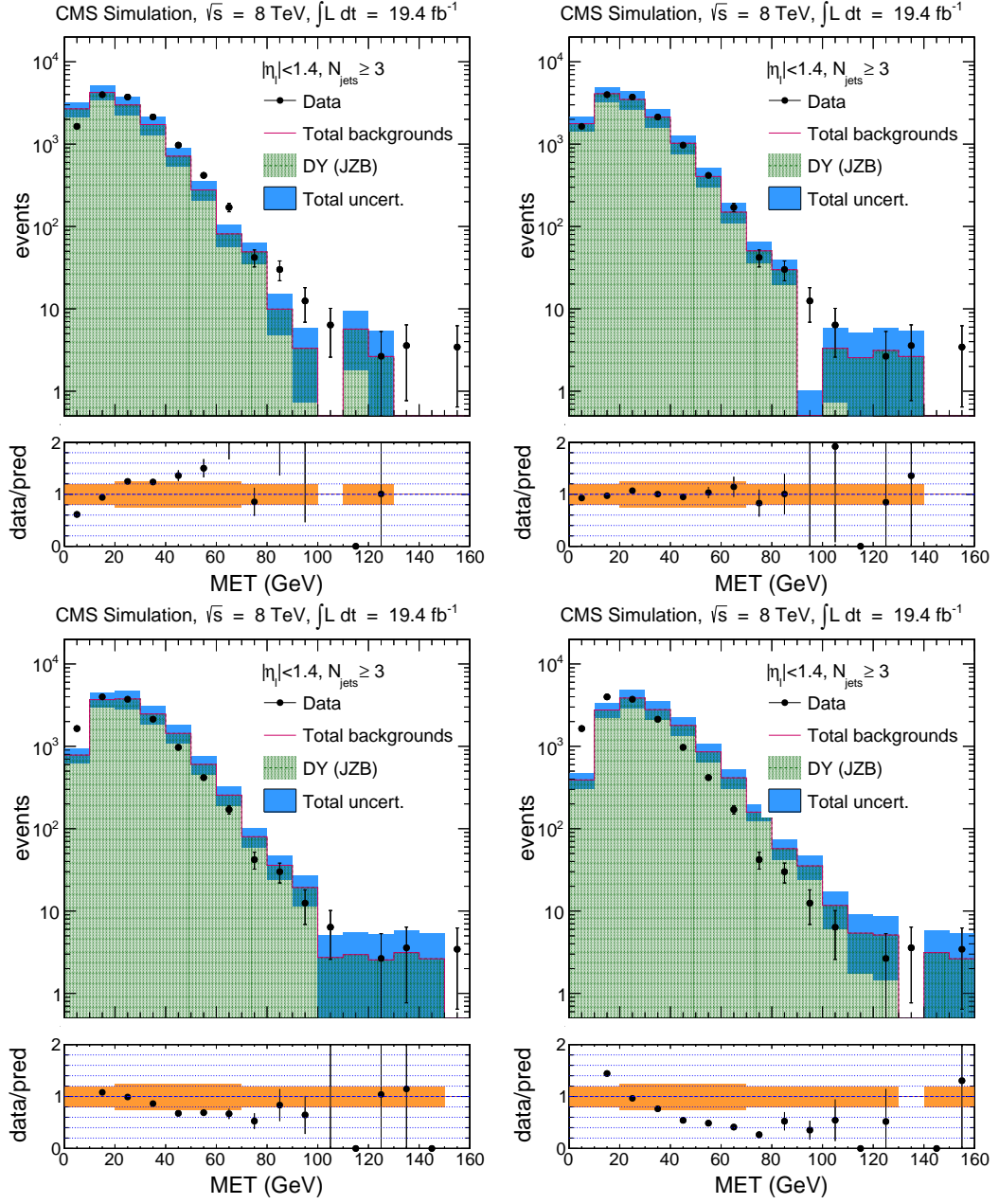


Figure 5.20: Comparisons of predicted and observed E_T^{miss} distribution in a sample of simulated Drell-Yan events for different values of the modification parameter λ : the different cases shown are $\lambda = -2$ (top left), $\lambda = -1$ (top right), $\lambda = 0$ (bottom left), and $\lambda = +1$ (bottom right). The best value is found to be $\lambda = -1$.

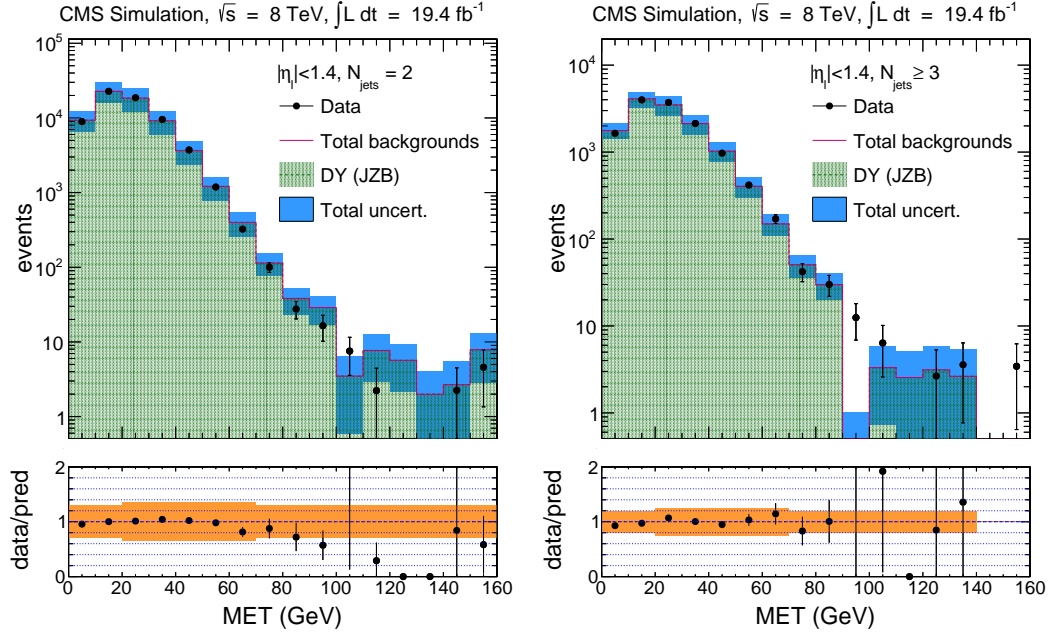


Figure 5.21: Observed and predicted E_T^{miss} distribution in a sample of simulated Drell-Yan events, for events with two jets (left) and three jets (right).

“predicted” sample is multiplied by a factor of two in order to obtain a $Z + \text{jets}$ prediction of the full sample and not only the subsample.

The signal region Z mass window prediction is also provided separately for the e^+e^- and $\mu^+\mu^-$ final states,

$$N_{Z+\text{jets}, e^+e^-}^{\text{est}} = 2 \cdot (N_{e^+e^-} - R(ee/OF)N_{OF})$$

$$N_{Z+\text{jets}, \mu^+\mu^-}^{\text{est}} = 2 \cdot (N_{\mu^+\mu^-} - R(\mu\mu/OF)N_{OF}) .$$

The predictions for the different jet multiplicities are combined to provide one estimate for the Z mass window in the signal region for the central selection and one for the forward selection.

The Z prediction for the Z window is 104 ± 25 (stat) ± 18 (sys) for the central signal region, and 14.2 ± 14.6 (stat) ± 2.8 (sys) for the forward signal region.

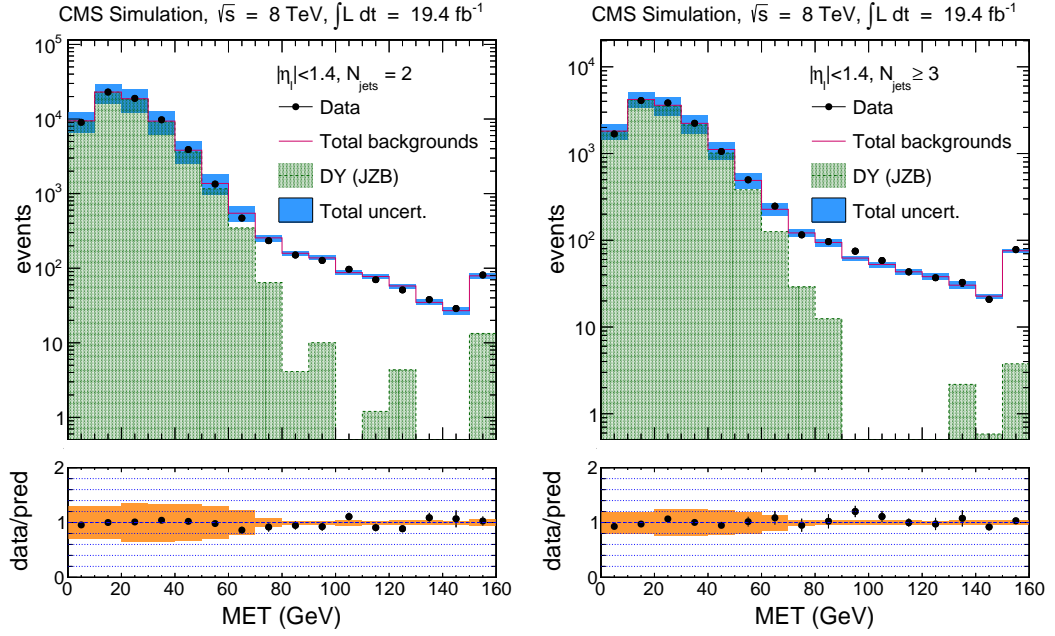


Figure 5.22: Observed and predicted E_T^{miss} distribution in a full mix of Monte Carlo samples for events with two jets (left) and three jets (right).

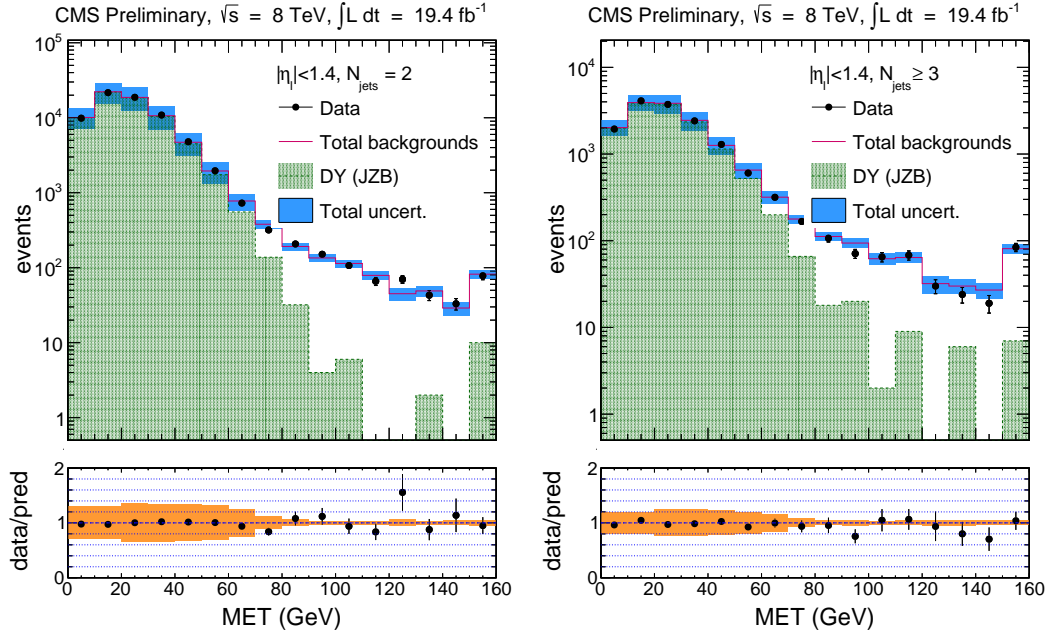


Figure 5.23: Observed and predicted E_T^{miss} distribution in data for events with two jets (left) and three jets (right).

5.3.3.3 Z Prediction From The E_T^{miss} Templates Method

The second method [107, 113] used to obtain an estimate of the SM Z yield is based on the premise that the E_T^{miss} in $Z + \text{jets}$ events stems from the hadronic recoil system and not from the leptons forming the Z boson candidate. The E_T^{miss} spectrum can therefore be determined in a statistically independent data control sample that consists of events with “fake” E_T^{miss} (i.e. no true E_T^{miss}). A $\gamma + \text{jets}$ sample is used since both $Z + \text{jets}$ and $\gamma + \text{jets}$ events contain a well-measured object recoiling against hadronic jets.

The E_T^{miss} distribution is measured in bins of the jet multiplicity and the scalar sum of jet transverse energies to account for kinematic differences between the hadronic systems in the control and signal samples. The E_T^{miss} distributions obtained in this way are then normalized to unit area and represent the prototypes for the E_T^{miss} template estimate.

The E_T^{miss} prediction for each Z event is the template with matching jet multiplicity, scalar sum of the transverse jet momentum, and transverse momentum of the Z candidate. The final predicted E_T^{miss} distribution is the sum of the individual E_T^{miss} predictions of all Z events; additional contributions from $t\bar{t}Z$, ZZ , and WZ are added based on MC. The E_T^{miss} prediction for a given selection can then be obtained from the predicted E_T^{miss} distribution.

The systematic uncertainty in the E_T^{miss} template prediction is based on a MC closure study, the variation of the photon selection criteria used to obtain the templates, and the PU reweighting procedure.

The predicted Z yields in the Z peak region ($81 < m_{\ell\ell} < 101$ GeV) based on the E_T^{miss} templates method are 133 ± 7 (stat) ± 32 (sys) for the central signal region and 56.9 ± 3.6 (stat) ± 14.0 (sys) for the forward signal region.

The E_T^{miss} template prediction presented in this Section and the estimate from the previous Section are combined in Sec. 5.3.3.5.

5.3.3.4 Low Mass Extrapolation

The previous estimates are computed specifically for the Z mass window range ($81 < m_{\ell\ell} < 101$ GeV); the result can be extrapolated to the low mass region (i.e. the signal region of the counting experiment) using the extrapolation factor $R_{\text{in/out}}$. This factor is determined from the dilepton invariant mass distribution in SF events in the DY-enriched control region (introduced in Sec. 5.2) after sub-

tracting the same distribution in opposite-flavor events (Figs. 5.24 and 5.25). The distribution is composed of almost only lepton pairs from a Z/γ^* and thus provides a reliable estimate of the differential Z/γ^* invariant mass distribution. The distribution is slightly different for electron and muon pairs, mainly because of significantly larger final state radiation (FSR) in the former case. This leads to a longer di-electron tail on the left side of the Z peak, as well as a slight depletion of the low mass region with respect to di-muon events. As a result, $R_{\text{in/out}}$ is systematically smaller in di-electron events, an effect which is confirmed in MC simulation.

The determination of $R_{\text{in/out}}$ is done in a region that differs from the signal regions in the jet multiplicity and $E_{\text{T}}^{\text{miss}}$ selection. No dependence of $R_{\text{in/out}}$ on $E_{\text{T}}^{\text{miss}}$ is expected, since $\text{DY} + \text{jets}$ only produce instrumental $E_{\text{T}}^{\text{miss}}$. A dependence with the jet multiplicity could in principle be observed because of the different kinematics in 2-jets and 3-jets $Z + \text{jets}$ events impacting the lepton reconstruction efficiency. In Fig. 5.26, a comparison is shown between the $m_{\ell\ell}$ distribution in the region where $R_{\text{in/out}}$ is determined and the $m_{\ell\ell}$ distribution in a region with higher $E_{\text{T}}^{\text{miss}}$ and jet multiplicity; the comparison demonstrates that the two measured shapes are indeed similar.

However, the variation of the invariant mass distribution with these requirements is a potential source of systematic uncertainty which needs to be quantified. This variation is studied in data and MC simulation. The results are shown in Fig. 5.27 for $E_{\text{T}}^{\text{miss}}$, and in Fig. 5.28 for the number of jets. $E_{\text{T}}^{\text{miss}}$ requirements above 40 GeV significantly reduce the statistics and the stability of the estimate. However, no significant $R_{\text{in/out}}$ variation with respect to the $E_{\text{T}}^{\text{miss}}$ selection is observed, neither in MC simulation nor in data. The ratio as a function of the number of jets indicates a possible increase of $R_{\text{in/out}}$ as the number of jets increases, both in data and MC simulation. For completeness, the comparison between the $m_{\ell\ell}$ distributions in data and MC simulation is also shown in Fig. 5.29.

Based on this study, a systematic uncertainty of 25% is assigned to $R_{\text{in/out}}$ in order to account for a possible bias due to the extrapolation to higher $E_{\text{T}}^{\text{miss}}$ and jet multiplicities, as well as differences between electrons and muons in the combined sample.

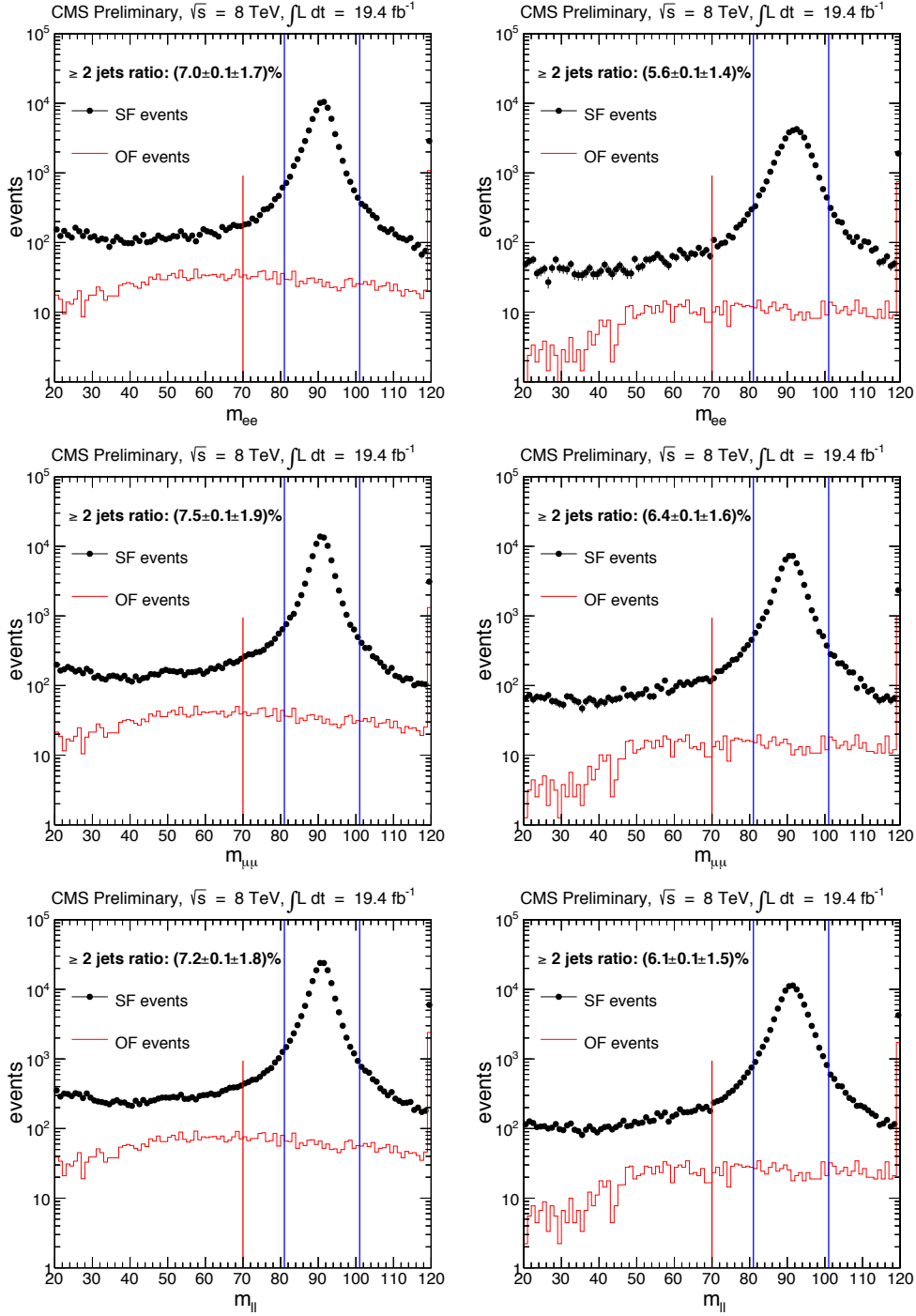


Figure 5.24: $m_{\ell\ell}$ distribution in SF events with at least 2 jets and $E_T^{\text{miss}} < 50$ GeV, after the central (left) and forward (right) lepton selections in **data**. The top, middle, and bottom plots show the e^+e^- , $\mu^+\mu^-$, and combined distributions. The corresponding opposite-flavor distribution is shown in red. The boundaries of the Z peak ($81 < m_{\ell\ell} < 101$ GeV) and signal ($20 < m_{\ell\ell} < 70$ GeV) mass regions are also shown.

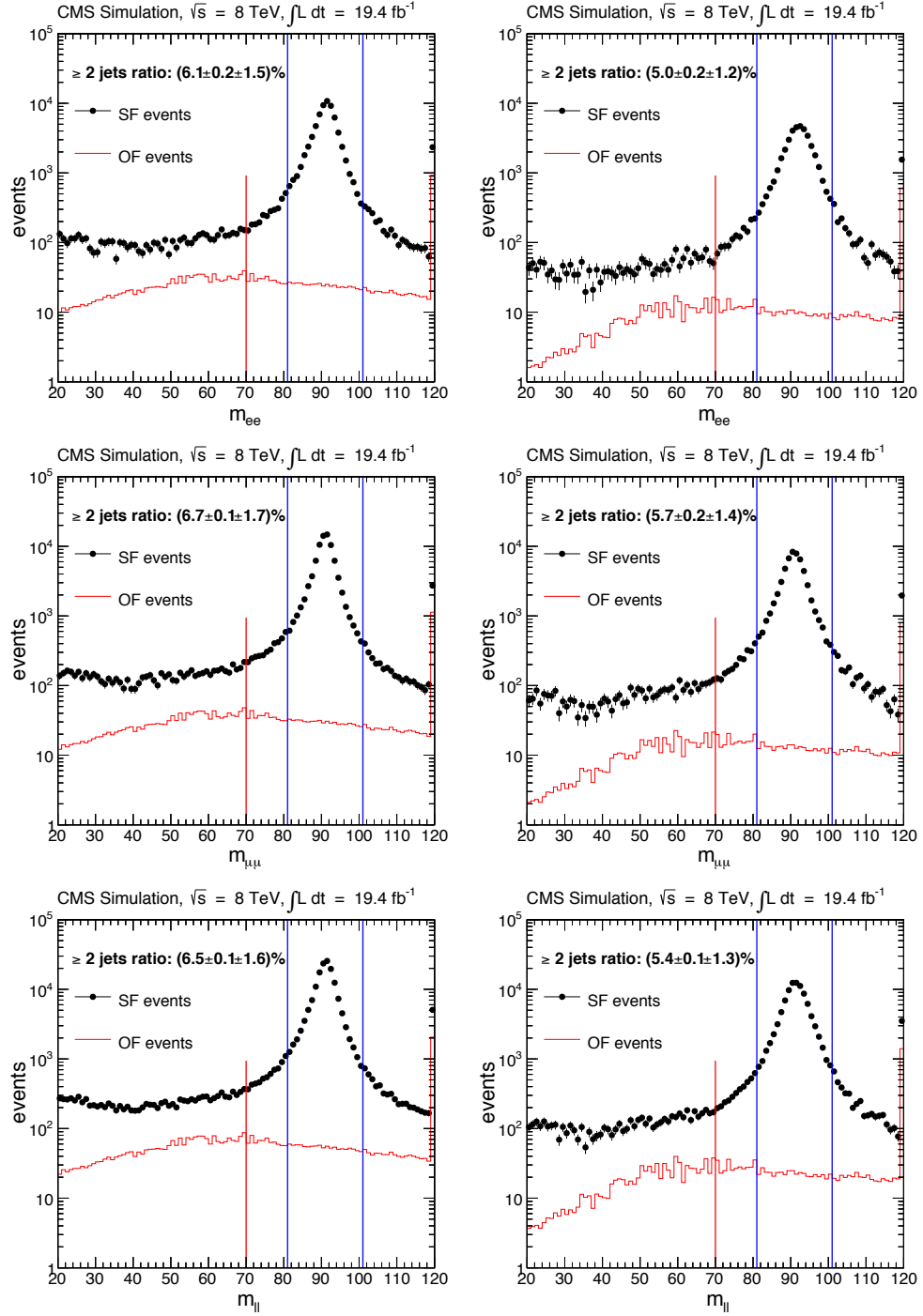


Figure 5.25: $m_{\ell\ell}$ distribution in SF events with at least 2 jets and $E_T^{\text{miss}} < 50$ GeV, after the central (left) and forward (right) lepton selections in MC simulation. The top, middle, and bottom plots show the e^+e^- , $\mu^+\mu^-$, and combined distributions. The corresponding opposite-flavor distribution is shown in red. The boundaries of the Z peak ($81 < m_{\ell\ell} < 101$ GeV) and signal ($20 < m_{\ell\ell} < 70$ GeV) mass regions are also shown.

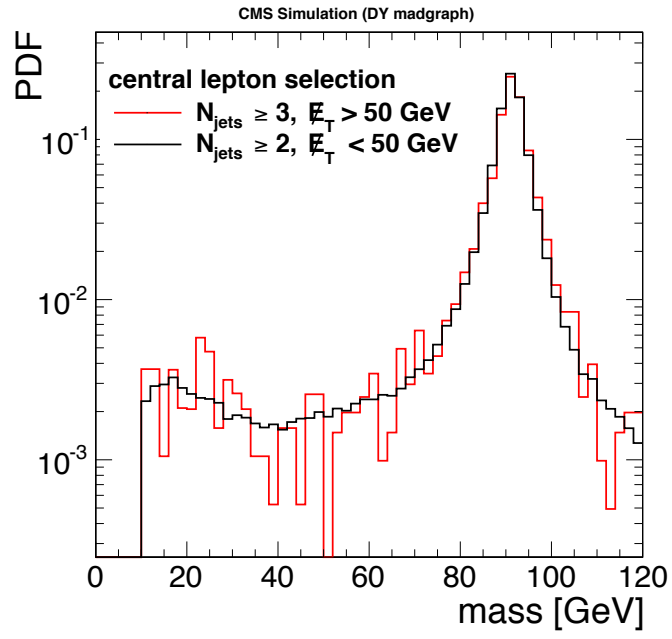


Figure 5.26: Shape comparison of the dilepton mass DY MC, for 2-jet events with $E_T^{\text{miss}} < 50 \text{ GeV}$ and 3-jet events with $E_T^{\text{miss}} > 50 \text{ GeV}$.

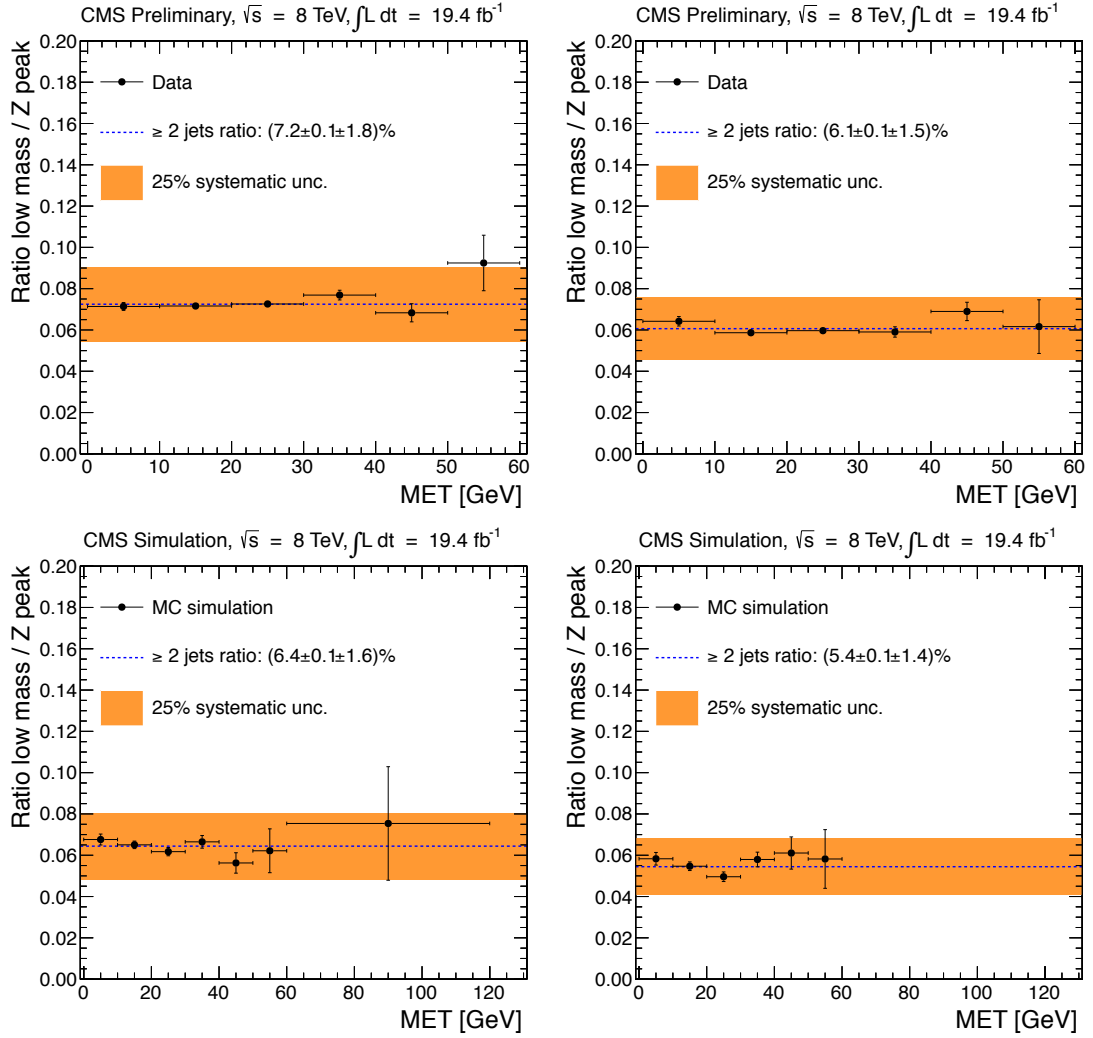


Figure 5.27: Variation of the $R_{\text{in/out}}$ ratio as a function of E_T^{miss} requirement in data (top) and MC simulation (bottom), after the central (left) and forward (right) lepton selections.

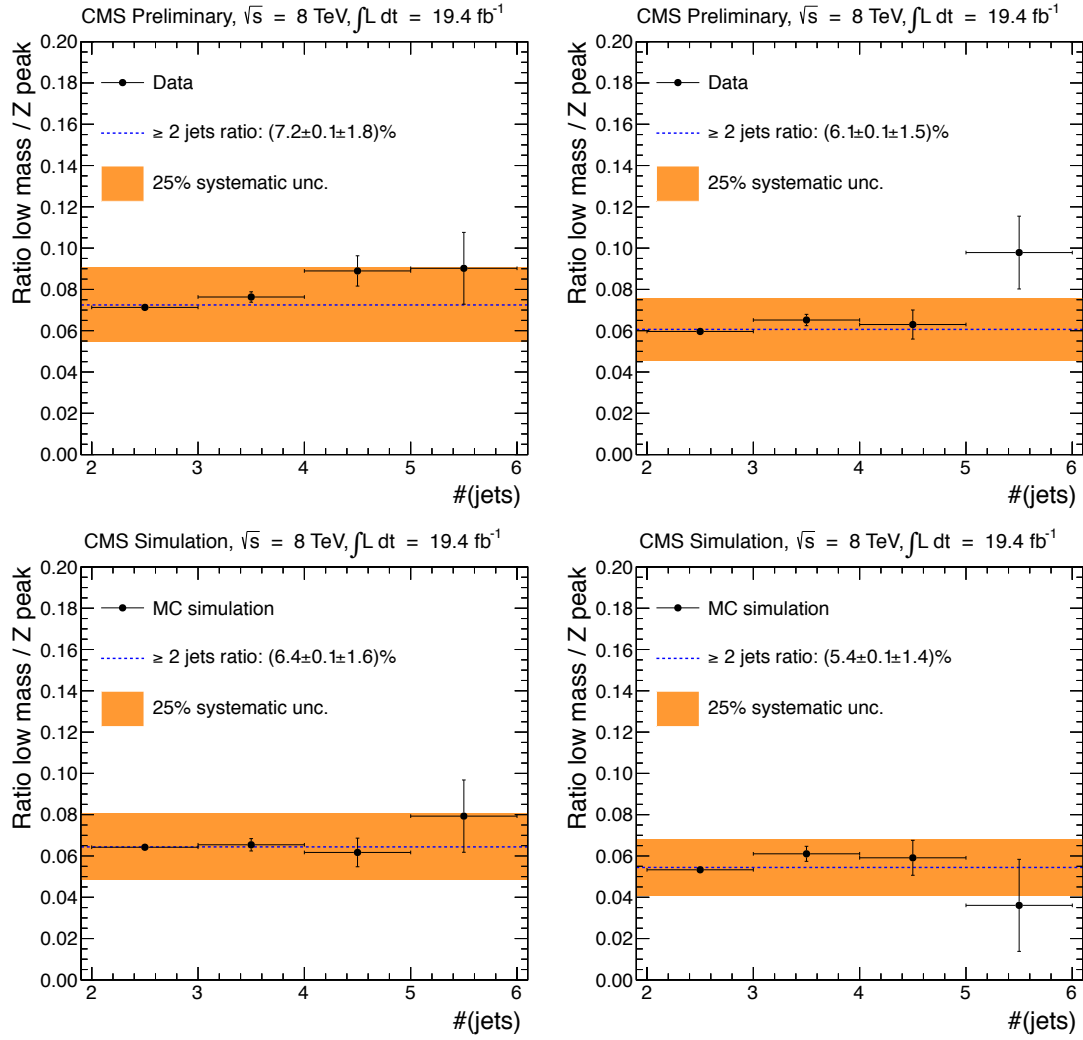


Figure 5.28: Variation of the $R_{\text{in/out}}$ ratio as a function of the number of jets requirement in data (top) and MC simulation (bottom), after the central (left) and forward (right) lepton selections. The last jet multiplicity bin also includes all higher multiplicities.

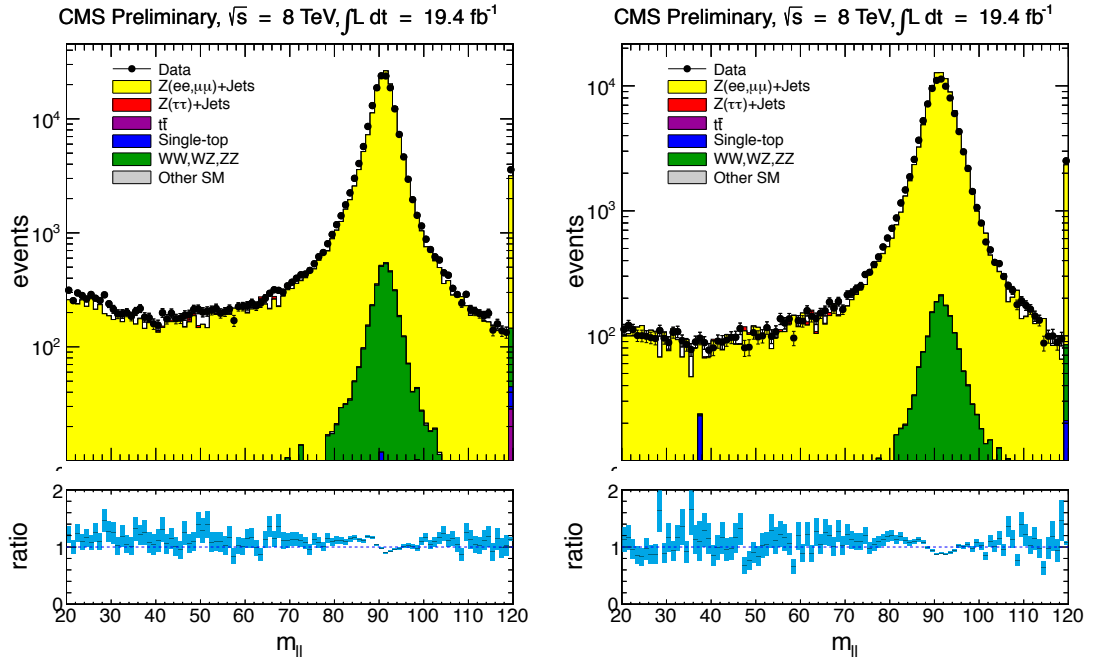


Figure 5.29: Comparison of the $m_{\ell\ell}$ distributions in data and MC simulation after the central (left) and forward (right) lepton selections.

5.3.3.5 Final Z + jets Estimate

With the JZB-based estimate in the Z mass window region (from Sec. 5.3.3.2), the E_T^{miss} templates-based estimate in the Z mass window region (from Sec. 5.3.3.3), and the extrapolation factor $R_{\text{in/out}}$ (from Sec. 5.3.3.4), a combined estimate of the Z background in the low mass signal region can be computed. The results for both methods, with the extrapolation factor and the low mass Z + jets estimates, are provided in Tab. 5.12. The estimates have also been split up into the different final states. The estimates in the central region agree reasonably well; the prediction from the E_T^{miss} templates and JZB-based estimate are about 0.6σ apart. The predictions in the forward region are about 2σ apart. Note, however, that the JZB estimate in the forward region is based on very few events. The final estimates in the low-mass signal region (used in the counting experiment) are 8.5 ± 2.7 events for the central selection and 2.2 ± 1.4 events for the forward selection. The Z + jets background is therefore very small compared to the flavor symmetric background (about two orders of magnitude smaller).

Table 5.12: Estimate of the Z background yields in the Z peak region and extrapolation to the signal mass region for the full dataset.

	central		
	e^+e^-	$\mu^+\mu^-$	SF
Z estimate (JZB)	$57.9 \pm 17.0 \pm 10.1$	$46.1 \pm 17.1 \pm 8.0$	$104 \pm 25 \pm 18$
Z estimate (MET templates)	$63.2 \pm 4.3 \pm 15.3$	$69.5 \pm 4.0 \pm 16.9$	$133 \pm 7 \pm 32$
Z estimate (Combined)	61.1 ± 12.4	58.2 ± 12.5	118 ± 22
$R_{\text{in/out}}$	$7.0 \pm 0.1 \pm 1.8\%$	$7.5 \pm 0.1 \pm 1.9\%$	$7.2 \pm 0.1 \pm 1.8\%$
Signal region estimate	4.3 ± 1.4	4.4 ± 1.5	8.5 ± 2.7
	forward		
	e^+e^-	$\mu^+\mu^-$	SF
Z estimate (JZB)	$10.3 \pm 10.0 \pm 1.9$	$3.9 \pm 10.0 \pm 1.4$	$14.2 \pm 14.6 \pm 2.8$
Z estimate (MET templates)	$24.4 \pm 1.8 \pm 6.0$	$32.3 \pm 2.2 \pm 7.9$	$56.9 \pm 3.6 \pm 14.0$
Z estimate (Combined)	20.5 ± 6.3	21.0 ± 13.9	36 ± 21
$R_{\text{in/out}}$	$5.6 \pm 0.1 \pm 1.4\%$	$6.4 \pm 0.1 \pm 1.6\%$	$6.1 \pm 0.1 \pm 1.5\%$
Signal region estimate	1.1 ± 0.5	1.3 ± 1.0	2.2 ± 1.4

5.3.4 Fake Leptons

An additional background source are processes with non-prompt leptons ("fakes"); this type of background is defined as containing a lepton that did not originate from a prompt decay³. One source of such fake leptons are jets which are reconstructed as electrons, but real leptons from heavy flavor decays and electrons from γ conversions may also contribute.

Three different methods are used to check whether this type of background is covered by the flavor symmetric estimate: the first approach makes use of Monte Carlo simulated samples to study the OF-SF mapping in more detail, whereas the second approach measures the background in data by using the "loose-to-tight" extrapolation, and the third utilizes same-sign events.

5.3.4.1 Contributions from Fake Leptons in Simulated Events

Intuitively, the contribution to the opposite-flavor final state is expected to be higher than that to the same-flavor final state, since the probability f_e for a "fake" electron to be reconstructed is higher than that of a muon (f_μ) and the reconstruction efficiency r_μ for muons is higher than for electrons (r_e). The most likely combination containing a "fake" is therefore a "true" muon with a "fake" electron, forming an opposite-flavor dilepton pair. Formally, the difference between the contribution to the same-flavor and the opposite-flavor final state due to backgrounds containing a "fake" lepton is given by

$$N_{SF} - N_{OF} = r_e f_e + r_\mu f_\mu - (r_e f_\mu + r_\mu f_e) = (r_e - r_\mu)(f_e - f_\mu) \quad (5.20)$$

which must be negative since $r_e < r_\mu$ and $f_e > f_\mu$.

The conclusion is checked using a mix of MADGRAPH W + jets and hadronic, semi-leptonic as well as fully leptonic $t\bar{t}$ MADGRAPH simulated samples. The leptons used in the analysis selection are matched to generator level particles and categorized accordingly into mutually exclusive groups ("true" dileptonic events containing two true leptons, and "fake" dileptonic events containing at least one "fake" lepton). The union of the two groups comprises all events in the sample. The W + jets sample as well as the $t\bar{t}$ hadronic and semi-leptonic samples do not contain any "true" dileptonic events, while a fraction of "fake" dileptonic events in the $t\bar{t}$ samples stems from the fully leptonic $t\bar{t}$ sample⁴.

³Examples of prompt decays include decays of W and Z bosons.

⁴The fake dilepton events in the fully leptonic $t\bar{t}$ sample stem from a missed real prompt lepton, while a reconstructed lepton was matched to a "fake".

The contribution from “fake” dilepton pairs is studied for three different selections,

- (i) a loose lepton preselection of all events passing the dilepton selection at reconstruction level (i.e. two leptons with $p_T > 20 \text{ GeV}$ and either $|\eta| < 1.4$ or $|\eta| > 1.6$, and no requirement on the number of jets or large E_T^{miss});
- (ii) the central signal region;
- (iii) and the forward signal region.

The event yields for all three selections, along with the $R(\text{SF}/\text{OF})$ value of the contributions, are shown in Tab. 5.13. As expected, the opposite-flavor event yields are at least consistent with the same-flavor yields and in most cases significantly higher. The dilepton mass distributions are shown in Fig. 5.30 and Fig. 5.31.

In summary, the event yields of $W + \text{jets}$ and $t\bar{t}$ processes with “fake” leptons are negligible and the flavor symmetric estimate fully accounts (and even slightly overestimates) the contribution.

5.3.4.2 Loose-to-Tight Method

A second approach, referred to as “loose-to-tight method”, is based on data control samples and has been extensively used in another dilepton analysis [114, 115]. Two different selections are considered, one corresponding to the nominal selection, and a second, looser selection with isolation and identification relaxed with respect to

Table 5.13: Number of events with fake dileptons in $W + \text{jets}$ ($W + \text{heavy flavor}$ included) and $t\bar{t}$ processes, after lepton preselection (no jets and E_T^{miss} cuts) and signal region selection, for 9.2 fb^{-1} .

	N(ee)	N($\mu\mu$)	N(SF)	N(OF)	R(SF/OF)
loose lepton preselection					
$W + \text{jets}$	358 ± 82.1	18.8 ± 18.8	377 ± 84.3	565 ± 103	0.667 ± 0.026
$t\bar{t}$	49.2 ± 1.1	28.7 ± 0.9	77.9 ± 1.4	78 ± 1.4	0.999 ± 0.026
signal region (central)					
$W + \text{jets}$	< 1	< 1	< 1	< 1	< 1
$t\bar{t}$	3.6 ± 0.6	3.5 ± 0.7	7.2 ± 0.9	6.3 ± 1.0	1.13 ± 0.23
signal region (forward)					
$W + \text{jets}$	< 1	< 1	< 1	< 1	< 1
$t\bar{t}$	1.1 ± 0.3	1.2 ± 0.4	2.3 ± 0.4	2.8 ± 0.5	0.82 ± 0.22

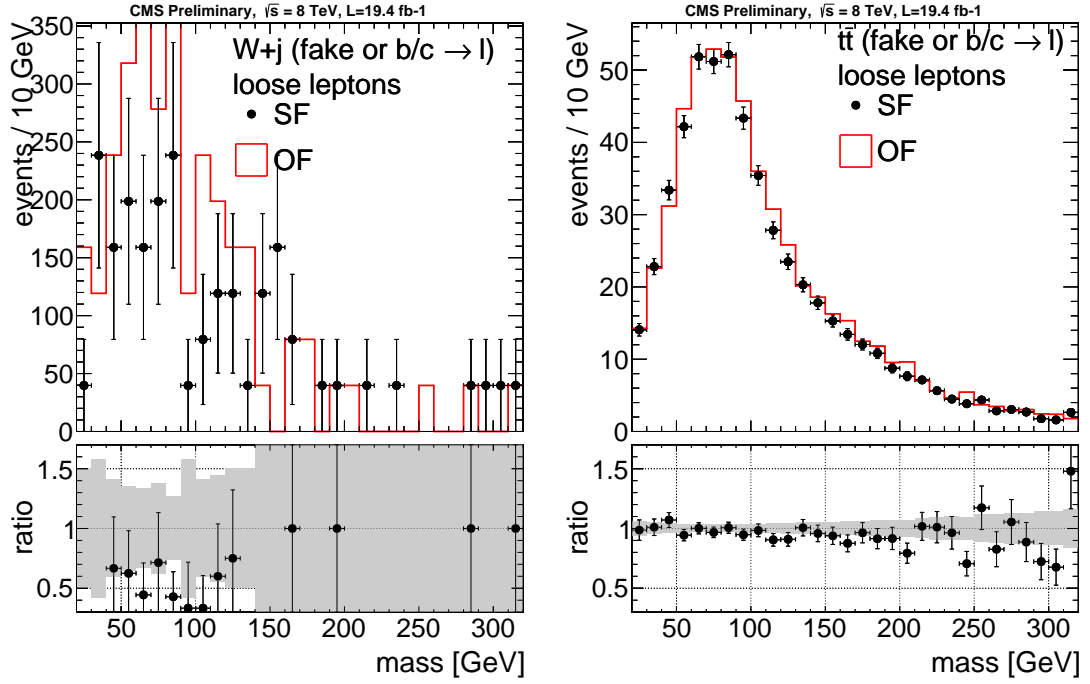


Figure 5.30: Same-flavor and opposite-flavor yields as a function of $m_{\ell\ell}$ for a sample of simulated $W + \text{jets}$ and $t\bar{t}$ events (**1 prompt lepton + 1 fake lepton**) with at least one of the reconstructed leptons to be matched to a generated non-prompt lepton (e.g., $B \rightarrow \ell\nu X$) or a fake lepton coming from mis-identification of hadrons (e.g., π^0 , ρ , $\pi^\pm K^\pm$); for the central signal region (left) and the forward signal region (right).

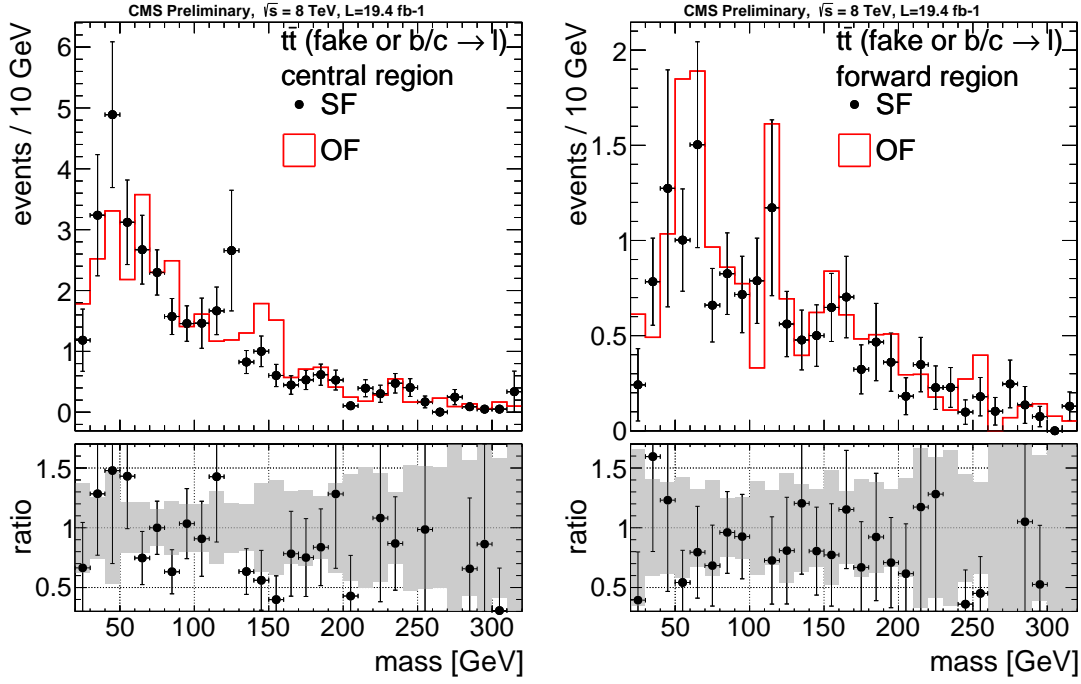


Figure 5.31: SF and OF yields as a function of $m_{\ell\ell}$ for $t\bar{t}$ (1 prompt lepton + 1 fake lepton) process reconstructed in the dilepton final state with at least one of the reconstructed leptons to be matched to a generated non-prompt lepton (e.g., $B \rightarrow \ell\nu X$) or a fake lepton coming from mis-identification of hadrons (e.g., π^0 , ρ , $\pi^\pm K^\pm$); for the central signal region (left) and the forward signal region (right).

the nominal (“tight”) selection. The probability, f , for a non-prompt lepton to pass the tight selection can be estimated by calculating the ratio between the number of tight and loose leptons in a QCD enriched region. Similarly, the probability, p , of a prompt lepton to pass the tight selection can be derived by calculating the ratio between tight and loose leptons in a $Z + \text{jets}$ enriched region. Once the probabilities have been determined, the number of events containing two tight, one tight and one loose, and two loose leptons in the signal region can be unfolded into the real number of expected non-prompt events (as discussed in [114]). The systematic uncertainty on the final estimate is 50% (as discussed in [114, 115]).

For the present study, the loose selection for muons only differs from the tight selection in the isolation. For electrons, both isolation and identification cuts are relaxed to essentially match the selection performed by the trigger. The values obtained for the probabilities f and p are

$$\begin{aligned} f_\mu &= 0.082 \pm 0.003 & p_\mu &= 0.94 \pm 0.01 \\ f_e &= 0.112 \pm 0.002 & p_e &= 0.88 \pm 0.01 . \end{aligned}$$

The number of events expected in the central and forward region for the tight-tight, tight-loose, and loose-loose combinations are summarized with the unfolded number of fakes in Tab. 5.14.

Table 5.14: Number of events passing the tight-tight, tight-loose, and loose-loose selections in the central and forward regions, and total fake estimates for different flavors including statistical uncertainty (first) and 50% systematic uncertainty.

central					
	ee	$\mu\mu$	$e\mu$	SF	OF
N_{tt}	196	236	312	432	312
N_{tl}	54	104	169	158	169
N_{ll}	6	12	12	18	12
Fakes	$0.3 \pm 1.0 \pm 0.2$	$7 \pm 1 \pm 3$	$12 \pm 2 \pm 6$	$7 \pm 1 \pm 4$	$12 \pm 2 \pm 6$
forward					
	ee	$\mu\mu$	$e\mu$	SF	OF
N_{tt}	25	47	72	72	72
N_{tl}	26	25	35	51	35
N_{ll}	3	2	2	5	2
Fakes	$2.6 \pm 0.7 \pm 1.3$	$1.7 \pm 0.5 \pm 0.9$	$2.3 \pm 0.7 \pm 1.2$	$4.3 \pm 0.8 \pm 2.2$	$2.3 \pm 0.7 \pm 1.2$

Table 5.15: Number of events with same sign leptons in the two signal regions.

	ee	$\mu\mu$	$e\mu$	SF	OF	SF-OF
central	4	4	8	8	8	0
forward	1	1	4	2	4	-2

The contribution of non-prompt leptons to the signal region, after subtracting the OF estimate, is determined to be $-5 \pm 1 \pm 8$ in the central region and $2 \pm 1 \pm 2$ in the forward region.

In summary, the loose-to-tight method confirms the conclusions from the first method: there is no significant contribution from “fakes” and the contribution is accounted for by the flavor symmetric estimate (and in fact slightly over-estimated). Furthermore, the results also show that the contribution from QCD multijet production is negligible.

5.3.4.3 Same-Sign Event Method

The third approach to estimate the contribution from non-prompt leptons is based on their charge symmetry: since fake leptons are equally likely to have positive or negative charge, events with two same-sign leptons can be used to estimate the contribution from non-prompt leptons to the same-flavor final state (provided that no same-sign BSM physics contribution is present in the low-mass signal region).

The number of events with same-sign leptons in the two signal regions is shown in Tab. 5.15. The number of opposite-flavor events is equal or greater than the number of same-flavor events, confirming the previous conclusions that the flavor symmetric estimate fully accounts for this background.

5.3.5 Rare Backgrounds

A number of rare SM processes that could potentially contribute to the signal region on top of the previously considered backgrounds have also been considered. These processes are either flavor symmetric (such as diboson production of WW or top pair production with a W boson, $t\bar{t}W$) or flavor asymmetric (such as diboson production of WZ or ZZ , and top pair production with a Z boson, $t\bar{t}Z$).

Flavor symmetric components of rare backgrounds are already accounted for by the flavor symmetric estimate, and a part of the non-flavor symmetric component is also accounted for by the Z prediction. The rare backgrounds are considered separately

using Monte Carlo simulation. However, since many of these processes have never been measured in data, their cross-section is only known from theory, so a 50% systematic uncertainty on the yields obtained from MC simulation is assigned, and any additional effects due to data/MC differences in trigger and reconstruction efficiencies are neglected.

The yields in the same-flavor and opposite-flavor final states are summarized in Tab. 5.16. The relevant estimate is the difference between the two, since the remainder is already part of the flavor symmetric estimate.

Table 5.16: Total expected yields in the central and forward region. The uncertainties in the prediction of the individual processes are statistical only while a 50% systematic uncertainty is applied to the total prediction. A factor of 0.5 is used to split between ee and $\mu\mu$. Differences in the factor are well covered by the 50% uncertainty.

central signal region				
Sample	σ [pb]	SF	OF	SF–OF
$t\bar{t} Z$	0.208	3.07 ± 0.25	2.28 ± 0.10	0.21 ± 0.32
WZ	1.06	2.95 ± 0.17	2.15 ± 0.15	0.80 ± 0.06
$ZZ \rightarrow 2\ell 2\nu$	0.3	1.03 ± 0.13	0.17 ± 0.04	0.89 ± 0.06
$ZZ \rightarrow 2\ell 2q$	2.449	1.77 ± 0.21	1.18 ± 0.17	0.59 ± 0.27
$ZZ \rightarrow 4\ell$	0.1769	0.110 ± 0.008	0.053 ± 0.006	0.059 ± 0.011
$t\bar{t} H$	0.13	2.40 ± 0.08	2.36 ± 0.08	0.04 ± 0.11
Total prediction		10.5 ± 0.4	8.0 ± 0.4	$2.5 \pm 0.6 \pm 1.3$
ee prediction		4.6 ± 0.2	4.0 ± 0.2	$0.6 \pm 0.4 \pm 0.4$
$\mu\mu$ prediction		5.9 ± 0.2	4.0 ± 0.2	$1.9 \pm 0.4 \pm 1.1$

forward signal region				
Sample	σ [pb]	SF	OF	SF–OF
$t\bar{t} Z$	0.208	0.57 ± 0.11	0.70 ± 0.11	-0.11 ± 0.15
WZ	1.06	0.95 ± 0.11	0.57 ± 0.08	0.38 ± 0.13
$ZZ \rightarrow 2\ell 2\nu$	0.3	0.19 ± 0.04	0.04 ± 0.017	0.15 ± 0.04
$ZZ \rightarrow 2\ell 2q$	2.449	0.36 ± 0.11	0.25 ± 0.08	0.13 ± 0.13
$ZZ \rightarrow 4\ell$	0.1769	0.040 ± 0.006	0.032 ± 0.004	0.008 ± 0.008
$t\bar{t} H$	0.13	0.40 ± 0.04	0.40 ± 0.04	0.02 ± 0.04
Total prediction		2.50 ± 0.19	1.9 ± 0.15	$0.6 \pm 0.2 \pm 0.4$
ee prediction		0.97 ± 0.11	0.95 ± 0.08	$0.02 \pm 0.23 \pm 0.02$
$\mu\mu$ prediction		1.54 ± 0.15	0.95 ± 0.08	$0.59 \pm 0.17 \pm 0.30$

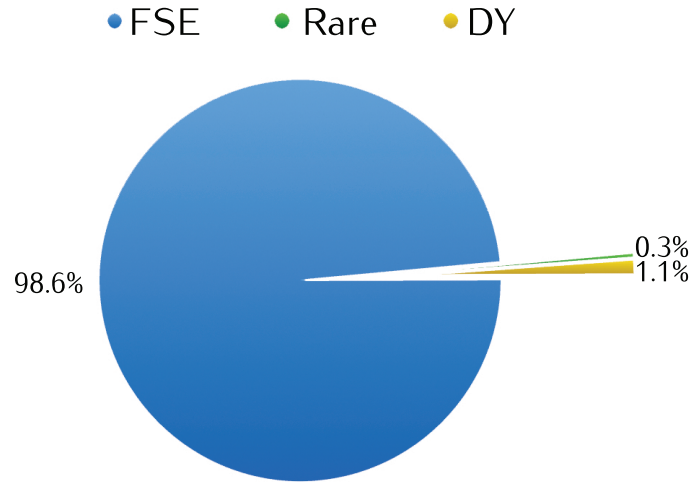


Figure 5.32: Relative importance of the different background estimates: the flavor symmetric estimate (“FSE”) is the most dominant contribution, followed by the Drell-Yan estimate (“DY”) contributing at the 1% level, and rare backgrounds (“rare”) contributing approximately 3 times less. Backgrounds from non-prompt leptons are not shown since they have been determined to be negligible.

The total contribution in the central region same-flavor channel is 10.5 ± 0.4 and for the opposite-flavor channel 8.0 ± 0.4 . In total, a residual contribution from rare backgrounds of $2.5 \pm 0.5 \pm 1.3$ events ($0.6 \pm 0.2 \pm 0.4$ events) is therefore expected for the central (forward) region. The rare backgrounds are therefore more than two orders of magnitude smaller than the flavor symmetric background.

5.3.6 Summary of Backgrounds

The backgrounds determined in the previous Sections are summarized in Tab. 5.17 and their relative importance is illustrated in Fig. 5.32. The flavor symmetric estimate has been determined using two independent methods based on data control samples; it is by far the most dominant contribution to the background estimate (approximately 98.5% of the total estimates). The Drell-Yan estimate plays a much smaller role (about 1.1%), and has also been determined with two independent methods. The rare backgrounds are even smaller (about 0.3% of the estimates), and backgrounds from non-prompt leptons have been determined to be negligible using three different methods. The estimates are compared to the observed yields in Sec. 5.5.

Table 5.17: Event yields estimated in the signal regions; statistical and systematic uncertainties are shown for the dominant flavor symmetric background; the uncertainties are added in quadrature for the sub-dominant backgrounds.

	central	forward
Flavor Symmetric Estimate	$722 \pm 27 \pm 29$	$155 \pm 13 \pm 10$
Drell-Yan Estimate	8.5 ± 2.7	2.2 ± 1.4
Rare Background Estimate	2.5 ± 1.5	0.6 ± 0.4
Total Estimates	733 ± 40	158 ± 16

5.4 Kinematic Edge Fit

In addition to the counting experiment, a fit to the dilepton mass spectrum is carried out to search for a kinematic edge. Many beyond the Standard Model scenarios, including supersymmetry, feature kinematic edges from cascade decays in which opposite-sign lepton pairs are produced (a typical example is $\tilde{\chi}_2^0 \rightarrow \ell\bar{\ell} \rightarrow \tilde{\chi}_1^0 \ell\bar{\ell}$). Due to the nature of the decay, the two leptons are correlated in flavor; lepton flavor mixing is assumed to be minimal⁵.

Unlike the counting experiment, the fit is directly sensitive to the mass hierarchy of the model since the kinematic edge position is related to the masses of the particles involved in the decay (see Sec. 2.4).

The different shapes used in the fit are discussed in Sec. 5.4.1, followed by the fit procedure in Sec. 5.4.2. The fit is then applied to a mix of Monte Carlo samples, with and without injected signal, in Sec. 5.4.3.

5.4.1 Background Model

The complete model used in the fit consists of three separate components (or “shapes”) which are discussed in the following, starting with the flavor symmetric backgrounds (Sec. 5.4.1.1), followed by the backgrounds containing a Z (Sec. 5.4.1.2), and then the signal shape (Sec. 5.4.1.3).

The full model is summarized in Sec. 5.4.1.4.

⁵For a discussion of kinematic edges in scenarios with flavor splitting see e.g. [116, 117].

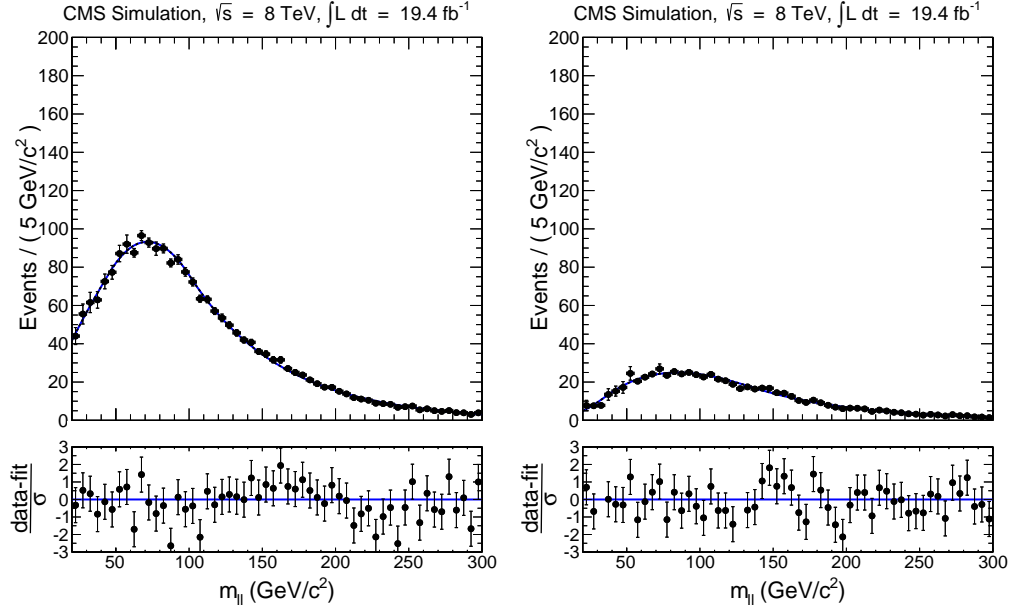


Figure 5.33: Fit of the flavor symmetric shape to the opposite-flavor sample in Monte Carlo simulated samples for the central (left) and forward (right) region.

5.4.1.1 Model for Flavor Symmetric Backgrounds

The model \mathcal{P}_{FS} describing the dilepton invariant mass distribution of the flavor symmetric background (which consists mainly of top pair production) is divided into three segments, with boundaries $m_{\ell\ell}^{(1)}$ and $m_{\ell\ell}^{(2)}$, and individual definitions for each segment:

$$\mathcal{P}_{FS}(m_{\ell\ell}) = \begin{cases} \mathcal{P}_{FS,1}(m_{\ell\ell}) = c_1 \cdot m_{\ell\ell}^\alpha & \text{if } 20 < m_{\ell\ell} < m_{\ell\ell}^{(1)} \\ \mathcal{P}_{FS,2}(m_{\ell\ell}) = \sum_{i=0}^3 c_{2,i} \cdot m_{\ell\ell}^i & \text{if } m_{\ell\ell}^{(1)} < m_{\ell\ell} < m_{\ell\ell}^{(2)} \\ \mathcal{P}_{FS,3}(m_{\ell\ell}) = c_3 \cdot e^{-\beta m_{\ell\ell}} & \text{if } m_{\ell\ell}^{(2)} < m_{\ell\ell} < 300. \end{cases}$$

The flavor symmetric (FS) model therefore contains 8 parameters and two boundaries. There are several constraints on the shape:

- (i) The probability density function (PDF) is required to be normalized,

$$\int_{20}^{m_{\ell\ell}^{(1)}} \mathcal{P}_{FS,1}(m_{\ell\ell}) dm_{\ell\ell} + \int_{m_{\ell\ell}^{(1)}}^{m_{\ell\ell}^{(2)}} \mathcal{P}_{FS,2}(m_{\ell\ell}) dm_{\ell\ell} + \int_{m_{\ell\ell}^{(2)}}^{300} \mathcal{P}_{FS,3}(m_{\ell\ell}) dm_{\ell\ell} = 1 ;$$

(ii) The PDF is required to be continuous and smooth at both boundaries,

$$\begin{aligned}\mathcal{P}_{FS,1}(m_{\ell\ell}^{(1)}) &= \mathcal{P}_{FS,2}(m_{\ell\ell}^{(1)}) \\ \mathcal{P}_{FS,2}(m_{\ell\ell}^{(2)}) &= \mathcal{P}_{FS,3}(m_{\ell\ell}^{(2)}) \\ \mathcal{P}'_{FS,1}(m_{\ell\ell}^{(1)}) &= \mathcal{P}'_{FS,2}(m_{\ell\ell}^{(1)}) \\ \mathcal{P}'_{FS,2}(m_{\ell\ell}^{(2)}) &= \mathcal{P}'_{FS,3}(m_{\ell\ell}^{(2)}) ,\end{aligned}$$

where \mathcal{P}' denotes the derivative with respect to the invariant mass;

(iii) The boundaries are required to be ordered ($m_{\ell\ell}^{(1)} \stackrel{!}{<} m_{\ell\ell}^{(2)}$).

The flavor symmetric model is therefore left with three free parameters and two boundaries, which are varied in the fit.

While the three samples (di-electron, di-muon and opposite-flavor) have different normalizations, the FS shape parameters derived above are common to all three (since the three samples share the same kinematics). The parameters of the flavor symmetric model are therefore

$$\vec{p}_{FS} = (c_{2,0}, c_{2,1}, c_{2,3}, m_{\ell\ell}^{(1)}, m_{\ell\ell}^{(2)}) . \quad (5.21)$$

Independent sets of parameters exist for the central and forward regions. The fit to the opposite-flavor final state for the central and forward regions in Monte Carlo simulated samples is shown in Fig. 5.33, illustrating the flavor symmetric background model.

5.4.1.2 Model for Backgrounds Containing a Z

The shape for backgrounds containing a Z is based on the sum of an exponential function and a convolution⁶ of a Breit-Wigner function $\mathcal{P}_{BW}(m_{\ell\ell}; m_Z, \sigma_Z)$, with physical mean m_Z and width σ_Z , and a double-sided Crystal-Ball function $\mathcal{P}_{DSCB}(m_{\ell\ell})$ defined as

$$\mathcal{P}_{DSCB}(m_{\ell\ell}) = \begin{cases} A_1(B_1 - \frac{m_{\ell\ell} - \mu_{CB}}{\sigma_{CB}})^{-n_1} & \text{if } \frac{m_{\ell\ell} - \mu_{CB}}{\sigma_{CB}} < -\alpha_1 \\ \exp\left(-\frac{(m_{\ell\ell} - \mu_{CB})^2}{2\sigma_{CB}^2}\right) & \text{if } -\alpha_1 < \frac{m_{\ell\ell} - \mu_{CB}}{\sigma_{CB}} < \alpha_2 \\ A_2(B_2 + \frac{m_{\ell\ell} - \mu_{CB}}{\sigma_{CB}})^{-n_2} & \text{if } \frac{m_{\ell\ell} - \mu_{CB}}{\sigma_{CB}} > \alpha_2 , \end{cases}$$

⁶The convolution component is based on the $H \rightarrow ZZ \rightarrow 4\ell$ signal shape [118].

where

$$A_i = \left(\frac{n_i}{|\alpha_i|} \right)^{n_i} \cdot \exp \left(-\frac{|\alpha_i|^2}{2} \right) \quad \text{and} \quad B_i = \frac{n_i}{|\alpha_i|} - |\alpha_i|.$$

The DY model is therefore given by

$$\mathcal{P}_{DY}(m_{\ell\ell}) = f_{exp} \mathcal{P}_{exp}(m_{\ell\ell}) + (1 - f_{exp}) \int \mathcal{P}_{DSCB}(m_{\ell\ell}) \mathcal{P}_{BW}(m_{\ell\ell} - m') dm',$$

where f_{exp} is the relative weight of the exponential and the convoluted shape. The model is fit separately for electrons and muons in the DY-enriched control region in order to extract the shape, which is then used with all shape parameters fixed in the signal region. The shapes for di-electron events and di-muon events are shown in Fig. 5.34 for the central and forward regions.

The electron and muon models use different values for the double-sided Crystal Ball function, and the relative normalization (f_{exp}) between the exponential and the convoluted function. They do, however, use the same values for m_Z^{pdg} and σ_Z^{pdg} (fixed to PDG values[7]). The full parameter set in the fit for electrons is

$$\vec{p}_Z^e = (\mu_{CB}^{ee}, \sigma_{CB}^{ee}, \alpha_1^{ee}, \alpha_2^{ee}, n_1^{ee}, n_2^{ee}, f_{exp}^{ee}, \mu_{exp}^{ee}) , \quad (5.22)$$

and for muons

$$\vec{p}_Z^\mu = (\mu_{CB}^{\mu\mu}, \sigma_{CB}^{\mu\mu}, \alpha_1^{\mu\mu}, \alpha_2^{\mu\mu}, n_1^{\mu\mu}, n_2^{\mu\mu}, f_{exp}^{\mu\mu}, \mu_{exp}^{\mu\mu}) .$$

Independent sets of parameters exist for the central and forward regions. The initial values of the normalization parameters are given by the $Z + \text{jets}$ estimates from Sec. 5.3.3.

5.4.1.3 Signal Model

The signal component is based on an edge model for two subsequent two-body decays with endpoint $m_{\ell\ell}^{edge}$, including a model for the dilepton mass resolution, $\sigma_{\ell\ell}$,

$$\mathcal{P}_S(m_{\ell\ell}) = \frac{1}{\sqrt{2\pi}\sigma_{\ell\ell}^2} \int_0^{m_{\ell\ell}^{edge}} y \cdot \exp \left(-\frac{(m_{\ell\ell} - y)^2}{2\sigma_{\ell\ell}^2} \right) dy.$$

The function describes a triangle convoluted with a Gaussian to account for the mass resolution. The parameter sets are therefore

$$\vec{p}_S^e = (m_{\ell\ell}^{edge}, \sigma_{CB}^{ee})$$

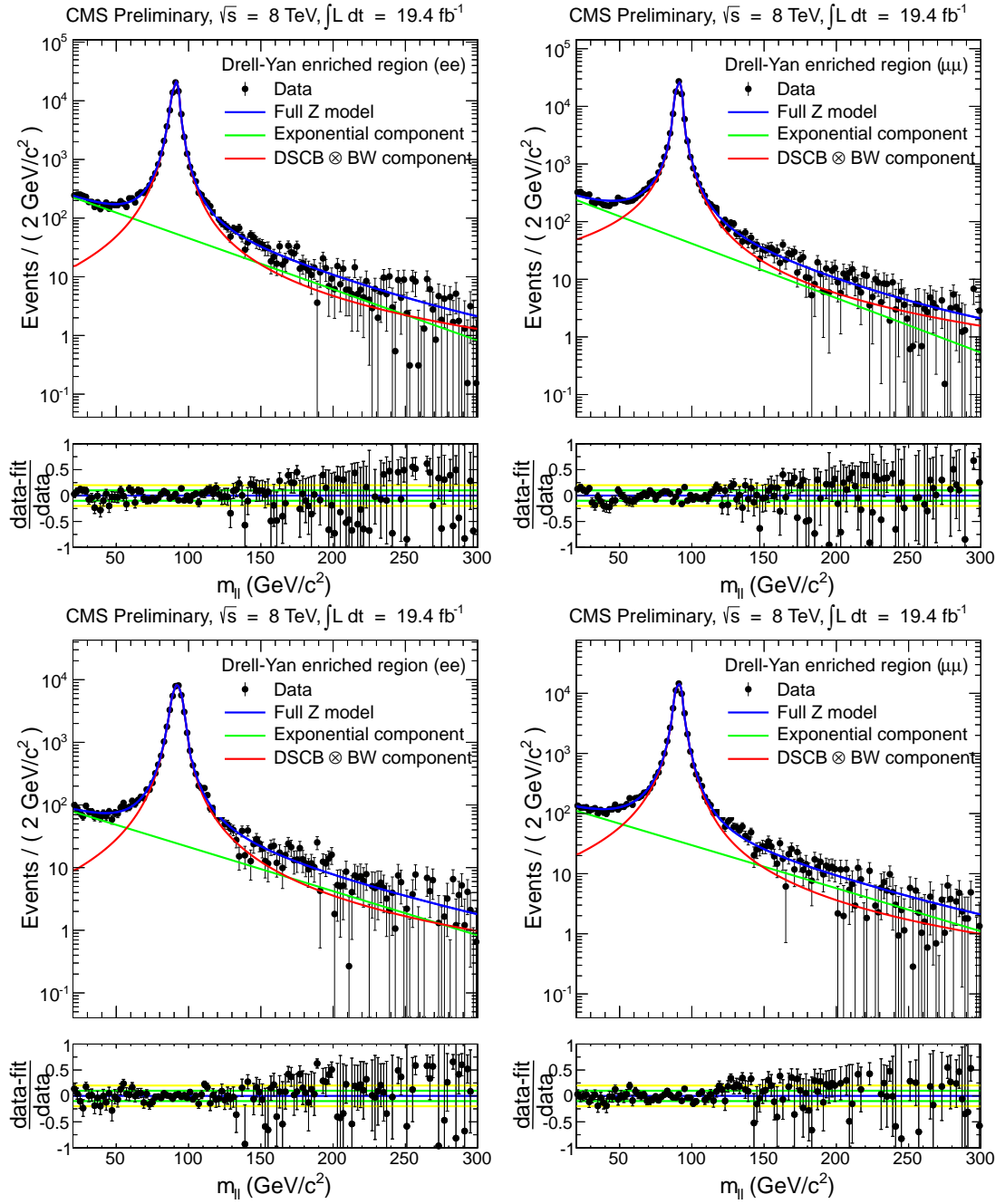


Figure 5.34: Fitted shape for backgrounds containing a Z for di-electron events (left) and di-muon events (right) for the central (top) and forward regions (bottom). The fitted shape consists of an exponential (green) and a peak model (red), the sum (blue) of which describes the backgrounds containing a Z. In the ratio plot, the blue line is located at 1.0, whereas a variation by 10% is indicated by the green lines and a variation by 20% by the yellow lines.

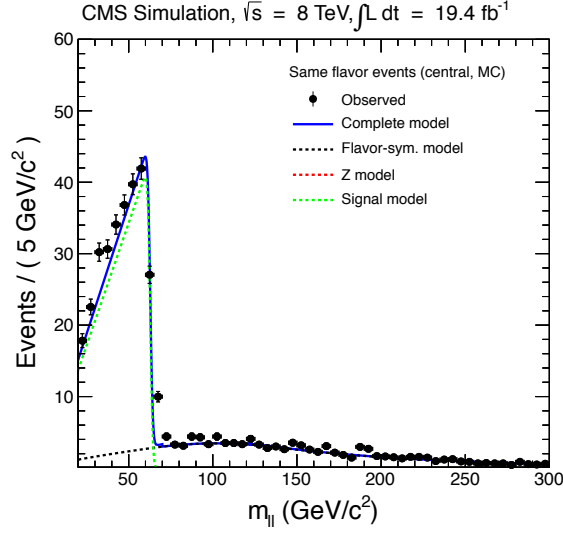


Figure 5.35: Illustration of the signal model (green) using a pMSSM point (described in Sec. 2.4.1); note that a small flavor symmetric contribution (black) also exists, while the Z model is not visible in this illustration.

for electrons and

$$\vec{p}_S^\mu = (m_{\ell\ell}^{edge}, \sigma_{CB}^{\mu\mu})$$

for muons, with each parameter set existing for the central and forward region. The resolutions σ_{CB}^i are those of the Drell-Yan shape (determined in the DY-enriched control region), and the edge position $m_{\ell\ell}^{edge}$ is the same for electrons and muons, and also for the central and forward region; it is the only parameter shared between the central and forward region since it is characteristic of the mass hierarchy of a given model.

The signal shape is illustrated⁷ in Fig. 5.35. A small flavor symmetric contribution from mis-combinations, described by the flavor symmetric shape, is also visible.

5.4.1.4 Complete Model

The model for the opposite-flavor final state is given by

$$\begin{aligned} \mathcal{P}_{OF}^C(m_{\ell\ell}) &= N_{FS}^C \mathcal{P}_{FS}^C(m_{\ell\ell}) \\ \mathcal{P}_{OF}^F(m_{\ell\ell}) &= N_{FS}^F \mathcal{P}_{FS}^F(m_{\ell\ell}) , \end{aligned}$$

⁷The signal shape in the illustration was not obtained using the full fit procedure but only serves illustrative purposes.

where the superscripts denote the region (central or forward). Two additional quantities need to be introduced to be able to find expressions for the di-electron and di-muon final states: the fraction f_{ee} is defined as the number of di-electron events divided by the number of same-flavor events, and represents the electron fraction in the same-flavor sample. Analogously, $f_{\mu\mu}$ represents the muon fraction in the same-flavor sample. Both fractions are defined separately for the central and forward region, and they sum to unity,

$$\begin{aligned} f_{ee}^C + f_{\mu\mu}^C &= 1 \\ f_{ee}^F + f_{\mu\mu}^F &= 1. \end{aligned}$$

The models for the di-electron and di-muon final states do not only contain a flavor symmetric component but also the additional components for backgrounds with a Z as well as the signal shape,

$$\begin{aligned} \mathcal{P}_{ee}^C(m_{\ell\ell}) &= f_{ee}^C (R_{SF/OF}^C N_{FS}^C \mathcal{P}_{FS}^C(m_{\ell\ell}) + N_Z^C \mathcal{P}_{Z,ee}^C(m_{\ell\ell}) + N_S^C \mathcal{P}_S^C(m_{\ell\ell}, \sigma_{ee}^C)) \\ \mathcal{P}_{\mu\mu}^C(m_{\ell\ell}) &= f_{\mu\mu}^C (R_{SF/OF}^C N_{FS}^C \mathcal{P}_{FS}^C(m_{\ell\ell}) + N_Z^C \mathcal{P}_{Z,\mu\mu}^C(m_{\ell\ell}) + N_S^C \mathcal{P}_S^C(m_{\ell\ell}, \sigma_{\mu\mu}^C)) \end{aligned}$$

for the central region and

$$\begin{aligned} \mathcal{P}_{ee}^F(m_{\ell\ell}) &= f_{ee}^F (R_{SF/OF}^F N_{FS}^F \mathcal{P}_{FS}^F(m_{\ell\ell}) + N_Z^F \mathcal{P}_{Z,ee}^F(m_{\ell\ell}) + N_S^F \mathcal{P}_S^F(m_{\ell\ell}, \sigma_{ee}^F)) \\ \mathcal{P}_{\mu\mu}^F(m_{\ell\ell}) &= f_{\mu\mu}^F (R_{SF/OF}^F N_{FS}^F \mathcal{P}_{FS}^F(m_{\ell\ell}) + N_Z^F \mathcal{P}_{Z,\mu\mu}^F(m_{\ell\ell}) + N_S^F \mathcal{P}_S^F(m_{\ell\ell}, \sigma_{\mu\mu}^F)) \end{aligned}$$

for the forward region. In the following, the normalizations are abbreviated as follows:

$$\begin{aligned} N_{FS}^e &= f_{ee} \cdot (R_{SF/OF} \cdot N_{FS}) & N_{FS}^\mu &= f_{\mu\mu} \cdot (R_{SF/OF} \cdot N_{FS}) \\ N_Z^e &= f_{ee} \cdot N_Z & \text{and} & & N_Z^\mu &= f_{\mu\mu} \cdot N_Z \\ N_S^e &= f_{ee} \cdot N_S & & & N_S^\mu &= f_{\mu\mu} \cdot N_S, \end{aligned}$$

where the region superscripts (C and F) have been suppressed. The normalizations N_i^e and N_i^μ are therefore not floating parameters but analytical expressions of floating parameters. The signal normalization factors (N_S^C and N_S^F) are fixed to zero for the null hypothesis.

The relative electron fractions (f_{ee}) for both regions are strongly constrained by the total size of the same-flavor datasets,

$$\begin{aligned} N_{ee} &= f_{ee} \cdot (R_{SF/OF} N_{FS} + N_Z + N_S) \\ N_{\mu\mu} &= \underbrace{(1 - f_{ee})}_{f_{\mu\mu}} \cdot (R_{SF/OF} N_{FS} + N_Z + N_S), \end{aligned}$$

where the superscripts indicating the region have been suppressed.

5.4.2 Procedure

The fit is carried out in different steps:

- (i) An initial fit is carried out in the DY-enriched control region to extract the DY shape, separately for electrons and muons, and for the central and forward region. Due to the size of the DY-enriched control region dataset, the uncertainties on the fitted parameters for the Drell-Yan shape are very small, making a variation of the DY-shape related variables in the full fit unnecessary; the DY shape has been varied in the fit and no significant change has been observed.
- (ii) A fit is then carried out in the signal region using an extended unbinned maximum likelihood fit, which is performed simultaneously for the dilepton invariant mass distribution in the di-electron, di-muon, and opposite-flavor final state, for both the central and the forward region concurrently.

The fit in (ii) is carried out twice, once for the null hypothesis (H_0) for which the signal normalizations are fixed at zero ($N_S^C = N_S^F = 0$) and once for the signal hypothesis (H_1) for which both signal normalizations are allowed to float freely.

The likelihood of the simultaneous fit in step (ii) is given by

$$\begin{aligned}
\mathcal{L}(m_{\ell\ell}; \mathbf{p}) &= \prod_{e^+e^- \in C} \left[N_{FS}^{e,C} \cdot \mathcal{P}_{FS}(m_{\ell\ell}; \mathbf{p}_{FS}^C) + N_Z^{e,C} \cdot \mathcal{P}_Z(m_{\ell\ell}; \mathbf{p}_Z^{e,C}) + N_S^{e,C} \cdot \mathcal{P}_S(m_{\ell\ell}; \mathbf{p}_S^{e,C}) \right] \\
&\times \prod_{\mu^+\mu^- \in C} \left[N_{FS}^{\mu,C} \cdot \mathcal{P}_{FS}(m_{\ell\ell}; \mathbf{p}_{FS}^C) + N_Z^{\mu,C} \cdot \mathcal{P}_Z(m_{\ell\ell}; \mathbf{p}_Z^{\mu,C}) + N_S^{\mu,C} \cdot \mathcal{P}_S(m_{\ell\ell}; \mathbf{p}_S^{\mu,C}) \right] \\
&\times \prod_{e^\pm\mu^\mp \in C} \left[N_{FS}^{OF,C} \cdot \mathcal{P}_{FS}^C(m_{\ell\ell}; \mathbf{p}_{FS}^C) \right] \\
&\times \prod_{e^+e^- \in F} \left[N_{FS}^{e,F} \cdot \mathcal{P}_{FS}(m_{\ell\ell}; \mathbf{p}_{FS}^F) + N_Z^{e,F} \cdot \mathcal{P}_Z(m_{\ell\ell}; \mathbf{p}_Z^{e,F}) + N_S^{e,F} \cdot \mathcal{P}_S(m_{\ell\ell}; \mathbf{p}_S^{e,F}) \right] \\
&\times \prod_{\mu^+\mu^- \in F} \left[N_{FS}^{\mu,F} \cdot \mathcal{P}_{FS}(m_{\ell\ell}; \mathbf{p}_{FS}^F) + N_Z^{\mu,F} \cdot \mathcal{P}_Z(m_{\ell\ell}; \mathbf{p}_Z^{\mu,F}) + N_S^{\mu,F} \cdot \mathcal{P}_S(m_{\ell\ell}; \mathbf{p}_S^{\mu,F}) \right] \\
&\times \prod_{e^\pm\mu^\mp \in F} \left[N_{FS}^{OF,F} \cdot \mathcal{P}_{FS}^F(m_{\ell\ell}; \mathbf{p}_{FS}^F) \right] \\
&\times \mathcal{N} \times \mathcal{G}(\mathbf{p}; \text{constraints}),
\end{aligned}$$

where

$$\begin{aligned}
\mathcal{N} = & \frac{e^{N_{FS}^{e,C} + N_Z^{e,C} + N_S^{e,C}} (N_{FS}^{e,C} + N_Z^{e,C} + N_S^{e,C})^{n_{e^+e^-}^C}}{n_{e^+e^-}^C!} \\
& \times \frac{e^{N_{FS}^{\mu,C} + N_Z^{\mu,C} + N_S^{\mu,C}} (N_{FS}^{\mu,C} + N_Z^{\mu,C} + N_S^{\mu,C})^{n_{\mu^+\mu^-}^C}}{n_{\mu^+\mu^-}^C!} \\
& \times \frac{e^{N_{FS}^{OF,C}} (N_{FS}^{OF,C})^{n_{OF}^C}}{n_{OF}^C!} \\
& \times \frac{e^{N_{FS}^{e,F} + N_Z^{e,F} + N_S^{e,F}} (N_{FS}^{e,F} + N_Z^{e,F} + N_S^{e,F})^{n_{e^+e^-}^F}}{n_{e^+e^-}^F!} \\
& \times \frac{e^{N_{FS}^{\mu,F} + N_Z^{\mu,F} + N_S^{\mu,F}} (N_{FS}^{\mu,F} + N_Z^{\mu,F} + N_S^{\mu,F})^{n_{\mu^+\mu^-}^F}}{n_{\mu^+\mu^-}^F!} \\
& \times \frac{e^{N_{FS}^{OF,F}} (N_{FS}^{OF,F})^{n_{OF}^F}}{n_{OF}^F!}
\end{aligned}$$

is a normalization factor, and n_i^j (with $i \in \{e^+e^-, \mu^+\mu^-, OF\}$ and $j \in \{C, F\}$) are the number of processed events in the corresponding subsample. The likelihood has only one variable, the invariant dilepton mass $m_{\ell\ell}$.

Penalties are added to take the measured values of $R(\text{SF}/\text{OF})$ for both regions into account. The penalties are implemented by using Gaussian PDFs centered at the measured value of $R(\text{SF}/\text{OF})$ with the total uncertainty on the measured value of $R(\text{SF}/\text{OF})$ being used as the width of the Gaussian PDF,

$$\mathcal{G} \left(\frac{N_{FS}^e + N_{FS}^\mu}{N_{FS}^{OF}}; R(\text{SF}/\text{OF})^{comb}, \sigma_{R(\text{SF}/\text{OF})^{comb}} \right),$$

for each region, where the values of $R(\text{SF}/\text{OF})^{comb}$ and $\sigma_{R(\text{SF}/\text{OF})^{comb}}$ are the results of the combination described in Sec. 5.3.2.

An overview of the floating parameters in the fit in the signal region is given in Tab. 5.18, while the parameters in the fit in the DY-enriched control region (to extract the Drell-Yan shape) are summarized in Tab. 5.19 (these parameters are frozen in the full fit). The superscripts denoting the region were omitted to improve readability.

Table 5.18: Overview of all floating parameters in the full fit in the signal region, including their status, initial value and parameter range. Note that the parameters pertaining to the Drell-Yan shape (summarized in Tab. 5.19) are fixed and that each parameter exists once for each region with the notable exception of $m_{\ell\ell}^{edge}$.

	Parameter	status	initial value	range
	N_{FS}^{OF}, N_Z, N_S	floating	-	$] -\infty, \infty [$
	$R(\text{SF/OF})$	constrained	$R(\text{SF/OF})^{comb}$	$R(\text{SF/OF})^{comb} \pm 3 \cdot \sigma_{R(\text{SF/OF})^{comb}}$
	f_{ee}	floating	-	$[0, 1]$
\vec{p}_{FS}	$m_{\ell\ell}^{(1)} [\text{GeV}]$	floating	50	$[30, 80]$
	$m_{\ell\ell}^{(2)} [\text{GeV}]$	floating	120	$[100, 160]$
	$c_{2,0}$	floating	2000	$[-8000, 8000.0]$
	$c_{2,1}$	floating	120	$[-800, 800]$
	$c_{2,3}$	floating	0.01	$[0.0001, 0.1]$
\vec{p}_S	$m_{\ell\ell}^{edge} [\text{GeV}]$	floating	-	$[35, 300]$

Table 5.19: Overview of all floating parameters in the fit in the Drell-Yan enriched control region, including their status, initial value and parameter range; each parameter is defined (and fitted) separately for the central and forward region.

	Parameter	status	initial value	minimum	maximum
\vec{p}_Z^e	μ_{CB}^{ee} [GeV]	floating	3.0	-10	10
	σ_{CB}^{ee} [GeV]	floating	1.6	0	20
	α_1^{ee}	floating	1.16	0	10
	α_2^{ee}	floating	2.5	0	10
	n_1^{ee}	floating	2.9	0	20
	n_2^{ee}	floating	1.04	0	20
	f_{exp}^{ee}	floating	0.003	0	1000
	μ_{exp}^{ee} [GeV ⁻¹]	floating	-0.032	-0.2	0
\vec{p}_Z^μ	$\mu_{CB}^{\mu\mu}$ [GeV]	floating	3.0	-10	10
	$\sigma_{CB}^{\mu\mu}$ [GeV]	floating	1.6	0	20
	$\alpha_1^{\mu\mu}$	floating	1.16	0	10
	$\alpha_2^{\mu\mu}$	floating	2.5	0	10
	$n_1^{\mu\mu}$	floating	2.9	0	20
	$n_2^{\mu\mu}$	floating	1.04	0	20
	$f_{exp}^{\mu\mu}$	floating	0.003	0	1000
	$\mu_{exp}^{\mu\mu}$ [GeV ⁻¹]	floating	-0.026	-0.2	0

Table 5.20: Use of floating parameters for the different components; parameters used for the normalization are marked with an "n", parameters used for the shape are ticked (\checkmark). Note that parameters in \vec{p}_Z^i are frozen in the fit in the signal region.

	Parameter	$N_{FS}\mathcal{P}_{FS}$	$N_{FS}^e\mathcal{P}_{FS}$	$N_{FS}^\mu\mathcal{P}_{FS}$	$N_Z^e\mathcal{P}_{Z,ee}$	$N_Z^\mu\mathcal{P}_{Z,\mu\mu}$	$N_S^e\mathcal{P}_{S,ee}$	$N_S^\mu\mathcal{P}_{S,\mu\mu}$
	N_{FS}^{OF}	n	n	n				
	N_Z				n	n		
	N_S						n	n
	$R(\text{SF}/\text{OF})$		n	n				
	f_{ee}		n	n	n	n	n	n
\vec{p}_{FS}	$m_{\ell\ell}^{(1)}$	\checkmark	\checkmark	\checkmark				
	$m_{\ell\ell}^{(2)}$	\checkmark	\checkmark	\checkmark				
	$c_{2,0}$	\checkmark	\checkmark	\checkmark				
	$c_{2,1}$	\checkmark	\checkmark	\checkmark				
	$c_{2,3}$	\checkmark	\checkmark	\checkmark				
\vec{p}_S	$m_{\ell\ell}^{edge}$						\checkmark	\checkmark
\vec{p}_Z^e	μ_{CB}^{ee}				\checkmark			
	σ_{CB}^{ee}				\checkmark		\checkmark	
	α_1^{ee}				\checkmark			
	α_2^{ee}				\checkmark			
	n_1^{ee}				\checkmark			
	n_2^{ee}				\checkmark			
	f_{exp}^{ee}				\checkmark			
	μ_{exp}^{ee}				\checkmark			
\vec{p}_Z^μ	$\mu_{CB}^{\mu\mu}$					\checkmark		
	$\sigma_{CB}^{\mu\mu}$					\checkmark		
	$\alpha_1^{\mu\mu}$					\checkmark		
	$\alpha_2^{\mu\mu}$					\checkmark		
	$n_1^{\mu\mu}$					\checkmark		
	$n_2^{\mu\mu}$					\checkmark		
	$f_{exp}^{\mu\mu}$					\checkmark		
	$\mu_{exp}^{\mu\mu}$					\checkmark		
								\checkmark

5.4.3 Application to Monte Carlo Simulation

The fit is carried out using Monte Carlo simulation with and without an injected signal. The statistical significance of a possible excess over the background-only expectation is assessed with

$$Z^2 = -2 \ln \left(\frac{\max_{\Theta \in \Omega_0} \mathcal{L}(\Theta)}{\max_{\Theta \in \Omega} \mathcal{L}(\Theta)} \right)$$

where Ω is the full parameter space of all parameters Θ discussed in this Section, and

$$\Omega_0 = \{ \Theta \mid (\Theta \in \Omega) \wedge (N_S^C = 0) \wedge (N_S^F = 0) \wedge (m_{\ell\ell}^{edge} = 20) \}$$

is the restricted parameter space of H_0 . Note that since Ω_0 is a subset of Ω , any solution in Ω_0 minimizing \mathcal{L} is also a solution available in Ω , and the likelihood for the signal hypothesis is therefore always as large as the one in the null hypothesis.

Case Without an Injected Signal (Background Only)

The fit is carried out for the set of Monte Carlo simulated samples without any injected signal, first under the null hypothesis (illustrated in Fig. 5.36), and then under the signal hypothesis (see Fig. 5.37). In the absence of a signal, the fit reconstructs a signal yield compatible with zero, leading only to a very small improvement of the likelihood for H_1 over H_0 , and therefore low significance ($Z = 0.7\sigma$, $N_S^C = -18.2 \pm 43.6$, $N_S^F = -19.7 \pm 20.3$). The result of the fit in the absence of signal is shown in Fig. 5.36 for the null hypothesis and in Fig. 5.37 for the signal hypothesis.

Case With an Injected Signal

The fit is carried out again using a mix of Monte Carlo samples with an injected signal (the benchmark point introduced in Sec. 2.4.1); the results are shown in Fig. 5.38 for the null hypothesis and in Fig. 5.39 for the signal hypothesis. The likelihood significantly improves when evaluating H_1 as opposed to H_0 , and a large signal yield is obtained for the central region ($Z = 8.0\sigma$, $N_S^C = 256 \pm 16$, $N_S^F = 9.7 \pm 6.5$). The result of the fit with an injected signal is shown in Fig. 5.38 for the null hypothesis and in Fig. 5.39 for the signal hypothesis. The leptons from the injected signal are very central, which is visible in Fig. 5.39 (where the forward category has a very small signal component), and is also reflected in the fitted signal yields.

A scan of the p-value as a function of the edge position (shown in Fig. 5.40) was carried out for both the case without injected signal and the case with an injected signal (featuring a mass edge at 62.4 GeV, see Sec. 2.4.1). The kinematic edge maximizing the likelihood is determined to be at $m_{\ell\ell}^{edge} = 62.3 \pm 0.6$ GeV. Note that the likelihood of the model including the signal shape is always at least as large as the one not including the signal shape (since Ω_0 is a subset of Ω). The computed significance is therefore positive definite, and the maximum p-value is $p = 0.5$.

Conclusions from Application to Monte Carlo Simulated Samples

The cross-checks using Monte Carlo simulated samples have shown that the fit reconstructs a signal yield compatible with zero in the absence of signal, and a signal yield incompatible with zero in the presence of an injected signal. The fit also obtained a mass edge position compatible with the true mass edge of the injected signal. The p-value as a function of the dilepton mass does not feature a narrow spike at the mass edge but is rather broad. This is expected due to the following considerations:

- (i) Mass edge hypothesis m_i with $m_i < m_{\ell\ell}^{edge,true}$:
The set of events with $m_{\ell\ell} < m_i$ are better described by H_1 than H_0 , but events in $m_i < m_{\ell\ell} < m_{\ell\ell}^{edge,true}$ are not described well by either hypothesis. The number of events in this interval decreases as m_i approaches the true mass edge position, therefore leading to p-values increasingly closer to the minimum.
- (ii) Mass edge hypothesis $m_i = m_{\ell\ell}^{edge,true}$:
The set of events with $m_{\ell\ell} < m_i$ is better described by the full model of H_1 , and this set includes all signal events. The set of events between the assumed mass edge and the true mass edge is empty; the p-value is at its minimum.
- (iii) Mass edge hypotheses $m_i > m_{\ell\ell}^{edge,true}$:
For hypothesized mass edges above the true mass edge, the set of events in the interval $m_{\ell\ell}^{edge,true} < m_{\ell\ell} < m_i$ is described by the model including the signal shape in spite of the absence of any signal events; the signal hypothesis therefore does not lead to any improvement for these points, and the p-values become increasingly larger as the number of events in the set increases.

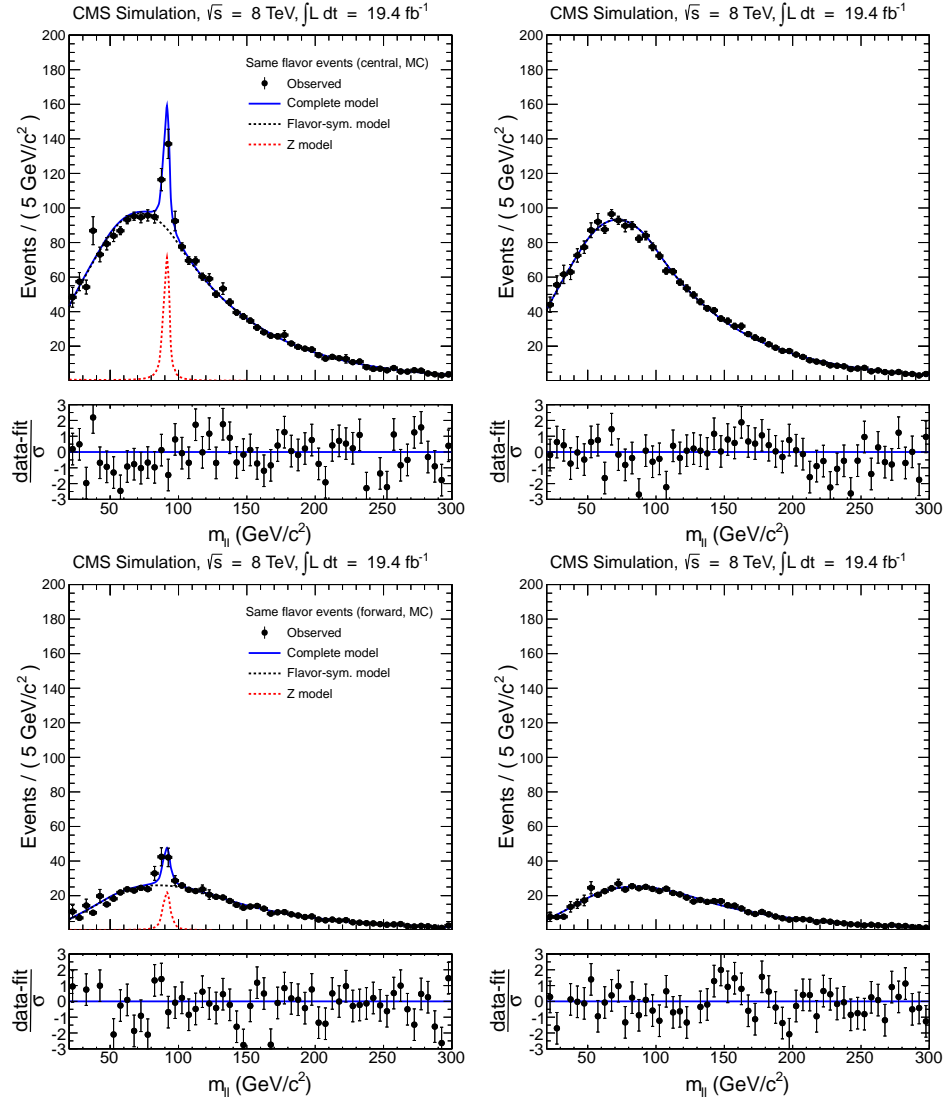


Figure 5.36: Result of fit in signal region for same-flavor (left) and opposite-flavor (right) events in the central (top) and forward (bottom) region for Monte Carlo simulation **without injected signal** evaluating the **null hypothesis**.

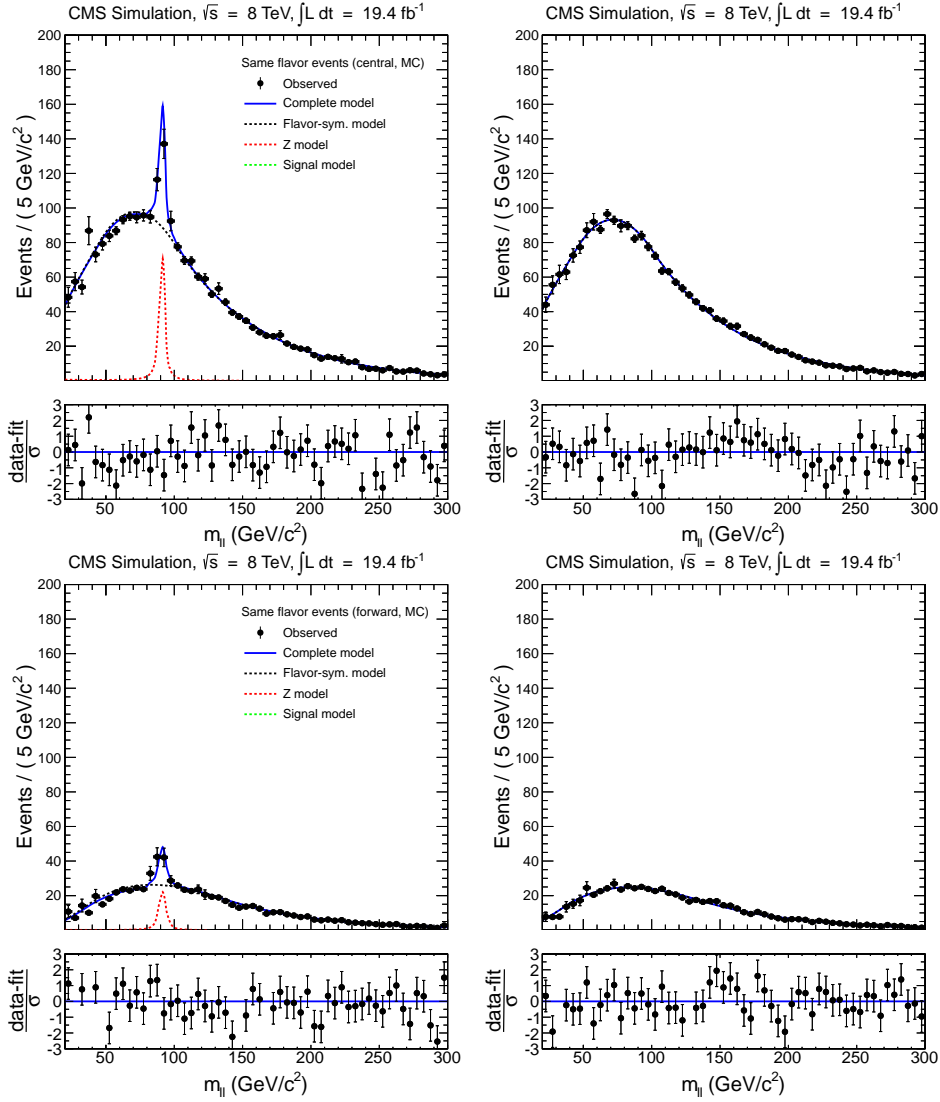


Figure 5.37: Result of fit in signal region for same-flavor (left) and opposite-flavor (right) events in the central (top) and forward (bottom) region for Monte Carlo simulation **without injected signal** evaluating the **signal hypothesis**.

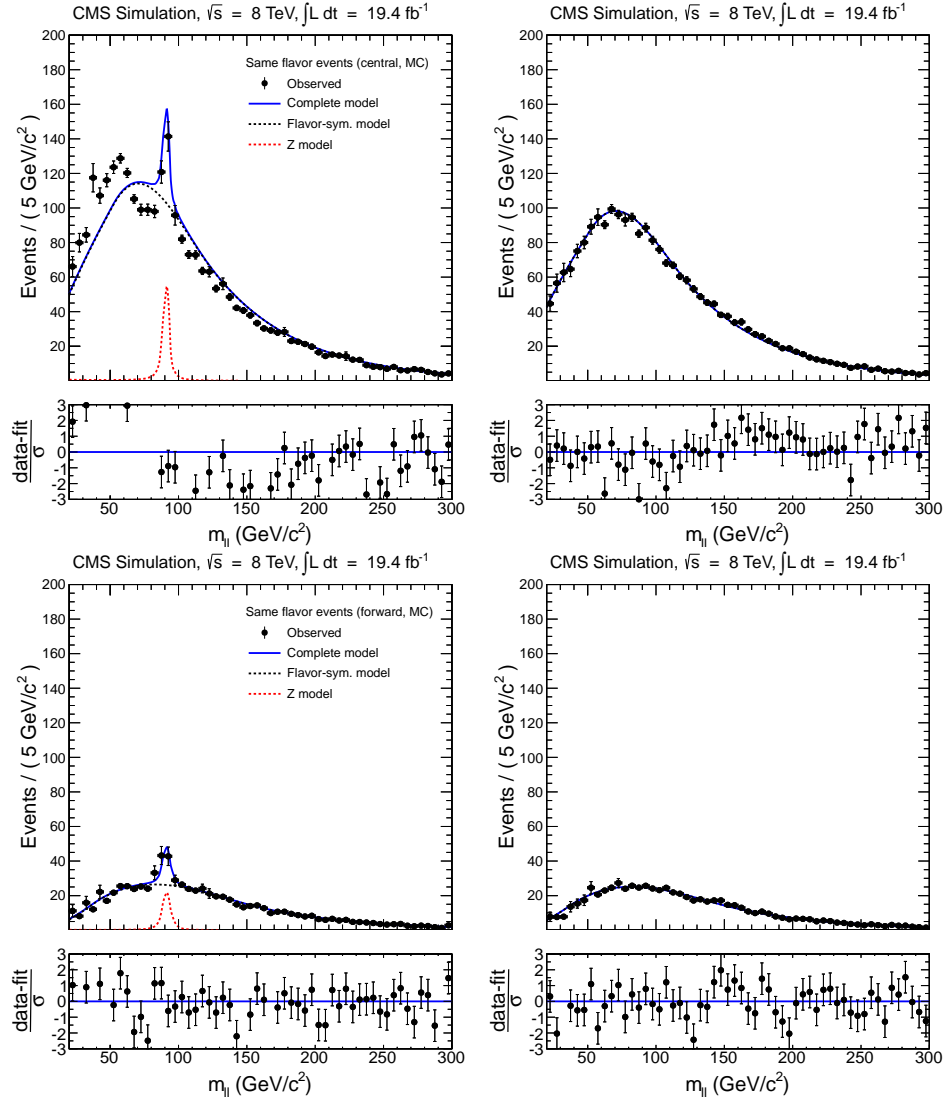


Figure 5.38: Result of fit in signal region for same-flavor (left) and opposite-flavor (right) events in the central (top) and forward (bottom) region for Monte Carlo simulation **with an injected signal** evaluating the **null hypothesis**.

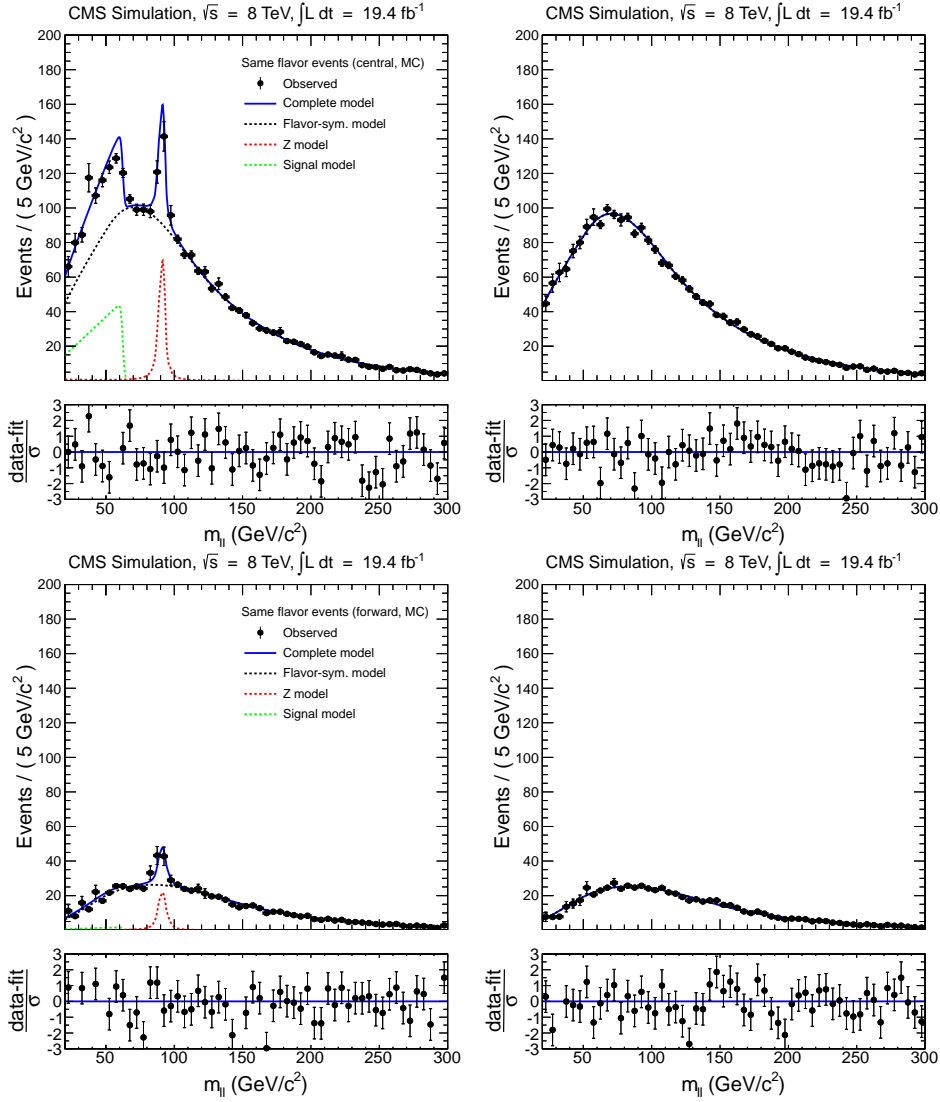


Figure 5.39: Result of fit in signal region for same-flavor (left) and opposite-flavor (right) events in the central (top) and forward (bottom) region for Monte Carlo simulation with an injected signal evaluating the signal hypothesis.

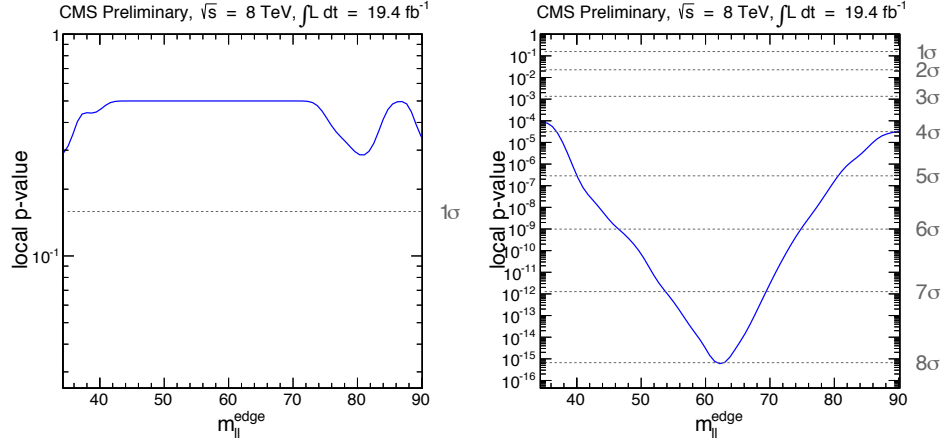


Figure 5.40: Scan of the log likelihood as a function of the edge position $m_{\ell\ell}^{edge}$ in Monte Carlo simulation without (left) and with (right) an injected signal. The true edge position is at 62.4 GeV, the reconstructed edge position is at 62.3 ± 0.6 GeV.

5.4.4 Comparison with Previous Searches for a Kinematic Edge

The present work is based on previous searches for a kinematic edge in CMS [106, 119, 120], but extends upon the previous iterations in many aspects. The flavor symmetric model has been replaced by an updated description with three segments, significantly improving the description of the flavor symmetric background. The Drell-Yan shape has been replaced; in the present work the low-mass rising tail has been included, and a more elaborate shape has been used for the peak component. The Drell-Yan shape is determined in an independent large statistics control region before the signal region fit, extracting a fixed shape and therefore also the resolution entering the signal model. Thanks to the two separate Z window estimates presented previously in Sec. 5.3.3, the fit now also contains a reference value for the Z background. The fit is not only carried out in the e^+e^- , $\mu^+\mu^-$ and OF final states simultaneously, but also for the central and forward region, which are linked only by the edge position (which is a parameter shared between all final states and regions). Furthermore, the fit takes advantage of the same-flavor to opposite-flavor transfer factors discussed in Sec. 5.3.2, by computing the value of $R(\text{SF}/\text{OF})$ for both regions in the fit and using the measured values as constraints.

5.5 Results

5.5.1 Counting Experiment

The dilepton mass distribution is shown in Fig. 5.41, where the background shape contains only the dominant flavor symmetry and SM $Z + \text{jets}$ background estimates (the rare backgrounds are not included but only make up approximately 0.3% of the full estimate). The full observed and predicted yields for the counting experiment are listed in Tab. 5.21. An excess has been found, and the significance has been computed using a profile likelihood method [121], taking into account statistical and systematic uncertainties. The significance has been determined to be 2.5σ for the central region and 0.2σ for the forward region. The results make use of the full CMS dataset; nonetheless, given the current integrated luminosity, the excess is still compatible with a statistical fluctuation.

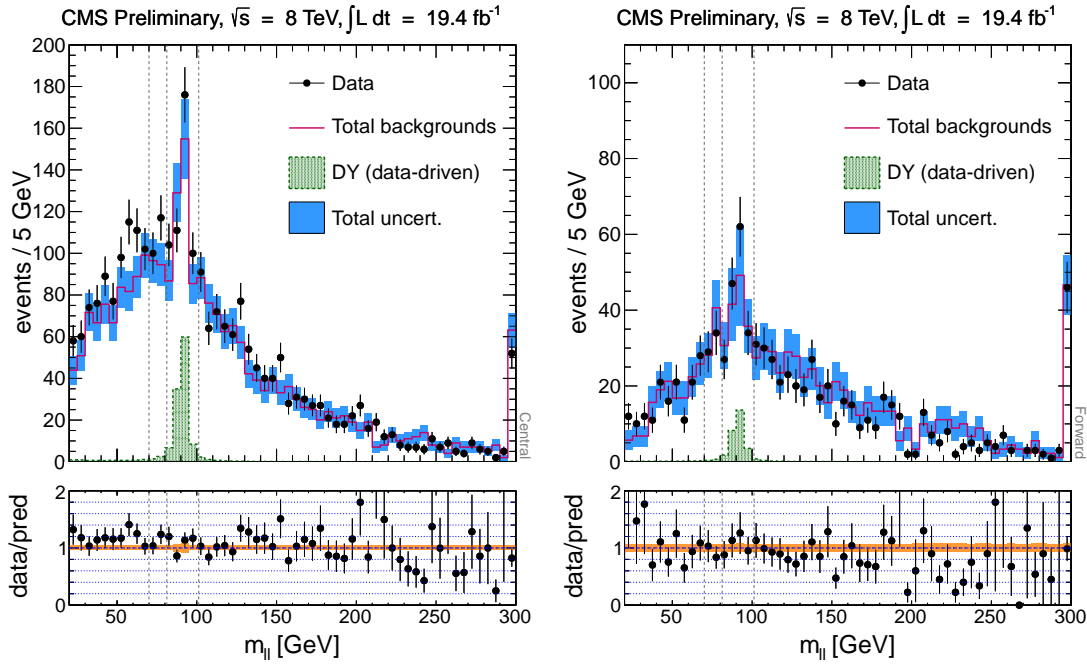


Figure 5.41: Comparison between the estimated and observed mass distributions in the central (left) and forward (right) signal regions. The blue band shows the total uncertainty on the background estimate. The bottom plots show the ratio between estimated and observed distributions. The uncertainties on the data points are statistical only, and the systematic uncertainty is indicated as an orange band.

Table 5.21: Event yields measured and estimated in the signal regions. Significances are calculated using the profile likelihood method [121]. Statistical and systematic uncertainties on the sub-dominant backgrounds are added in quadrature.

	central	forward
Observed	860	163
Flavor Symmetric Estimate	$722 \pm 27 \pm 29$	$155 \pm 13 \pm 10$
Drell-Yan Estimate	8.5 ± 2.7	2.2 ± 1.4
Rare Backgrounds	2.5 ± 1.5	0.6 ± 0.4
Total Estimates	733 ± 40	158 ± 16
Observed – Estimated	127^{+48}_{-49}	5^{+20}_{-21}
Significance	2.5σ	0.2σ

5.5.2 Search for a Kinematic Edge

The dilepton mass distributions in the central and forward signal regions are shown for the same-flavor and opposite-flavor final states in Fig. 5.42 for the null hypothesis. The fit has also been carried out for the alternative hypothesis, for which the resulting dilepton mass distributions are presented in Fig. 5.43.

A signal yield of 125.7 ± 41.2 in the central region (and 21.5 ± 20.1 in the forward region) is obtained when evaluating the signal hypothesis, with an edge position located at 78.7 ± 1.4 GeV. The results of the fit including the yields of the different model components are summarized in Tab. 5.22. The integrated yields of all model components in the low mass region are provided in Tab. 5.23 to allow for a comparison of the result of the fit with the estimates of the counting experiment (from Tab. 5.21); the agreement is very good.

The significance obtained in the fit is $Z = 2.96\sigma$ and the p-value is found to be $p_0 = 0.0015$. The difference between the negative log likelihood for any mass edge and the negative log likelihood for the best fitted value \hat{m}_{ll}^{edge} is shown, as a function of the edge position, in Fig. 5.44 (left) for a region close to the best fitted value. The local p-value is shown as a function of the edge position in Fig. 5.44 (right).

The effect of freezing the shape-related parameters of the Drell-Yan shape has been

studied by varying the relative weight of the exponential (which is directly related to the fitted value of $R_{\text{in/out}}$) by 25%. A negligible effect on the significance has been observed [96], justifying the freezing.

Table 5.22: Integrated yields of the different model components resulting from the unbinned maximum likelihood fit.

	central	forward
Z background	157.8 ± 22.9	70.6 ± 15
Flavor symmetric background	2270 ± 44	745 ± 25
$R(\text{SF/OF})$	1.026	1.018
Signal events	126 ± 41	21.5 ± 20.1
$m_{\ell\ell}^{\text{edge}}$	78.7 ± 1.4	
Significance [σ]	2.96	

Table 5.23: Integrated yields of the different model components of the unbinned maximum likelihood fit; the integration is restricted to the low-mass signal region to allow for a comparison with the estimates from the counting experiment listed in Tab. 5.21.

	central	forward
Z background	9.9 ± 1.0	3.7 ± 0.6
Flavor symmetric background	748 ± 17	146 ± 6
Signal events	97.7 ± 22.8	16.7 ± 11.1

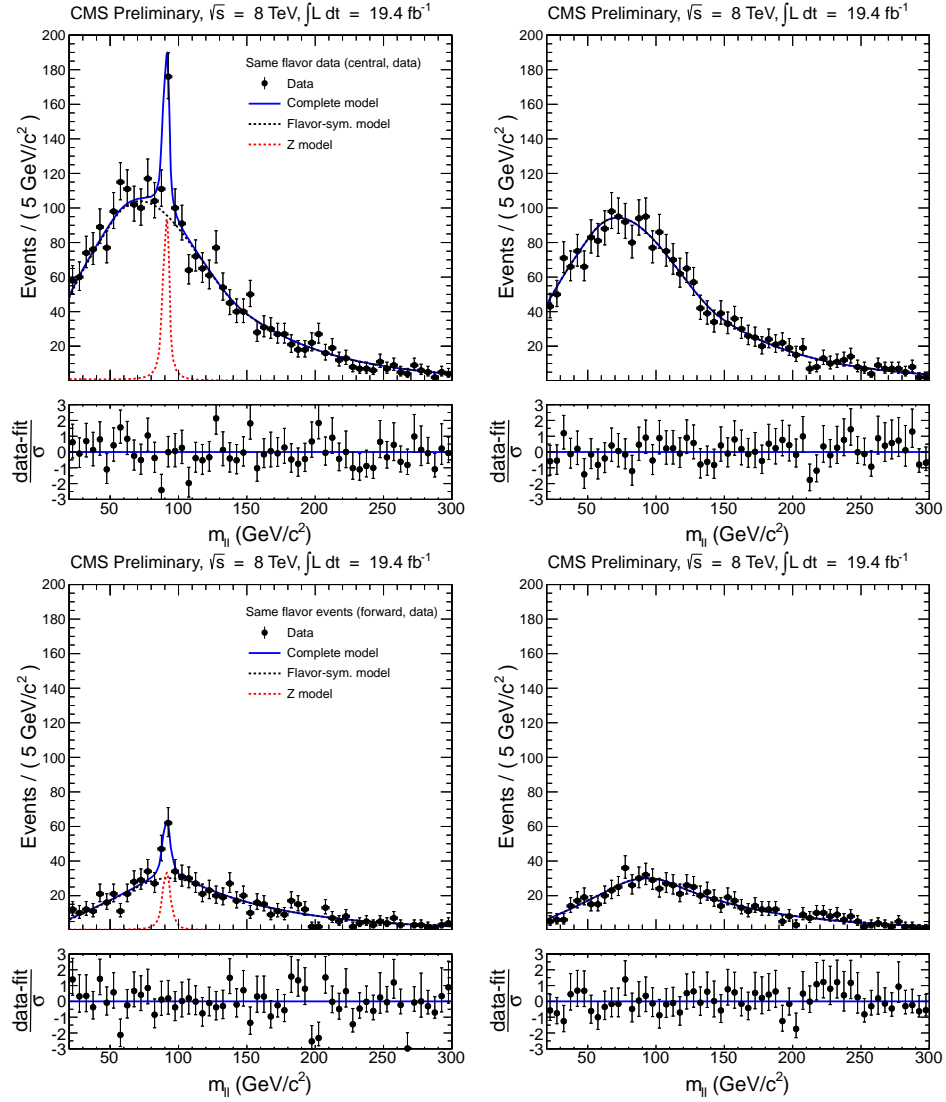


Figure 5.42: Result of fit in signal region for same-flavor (left) and opposite-flavor (right) events for **data** evaluating the **null hypothesis** in the central (top) and forward region (bottom).

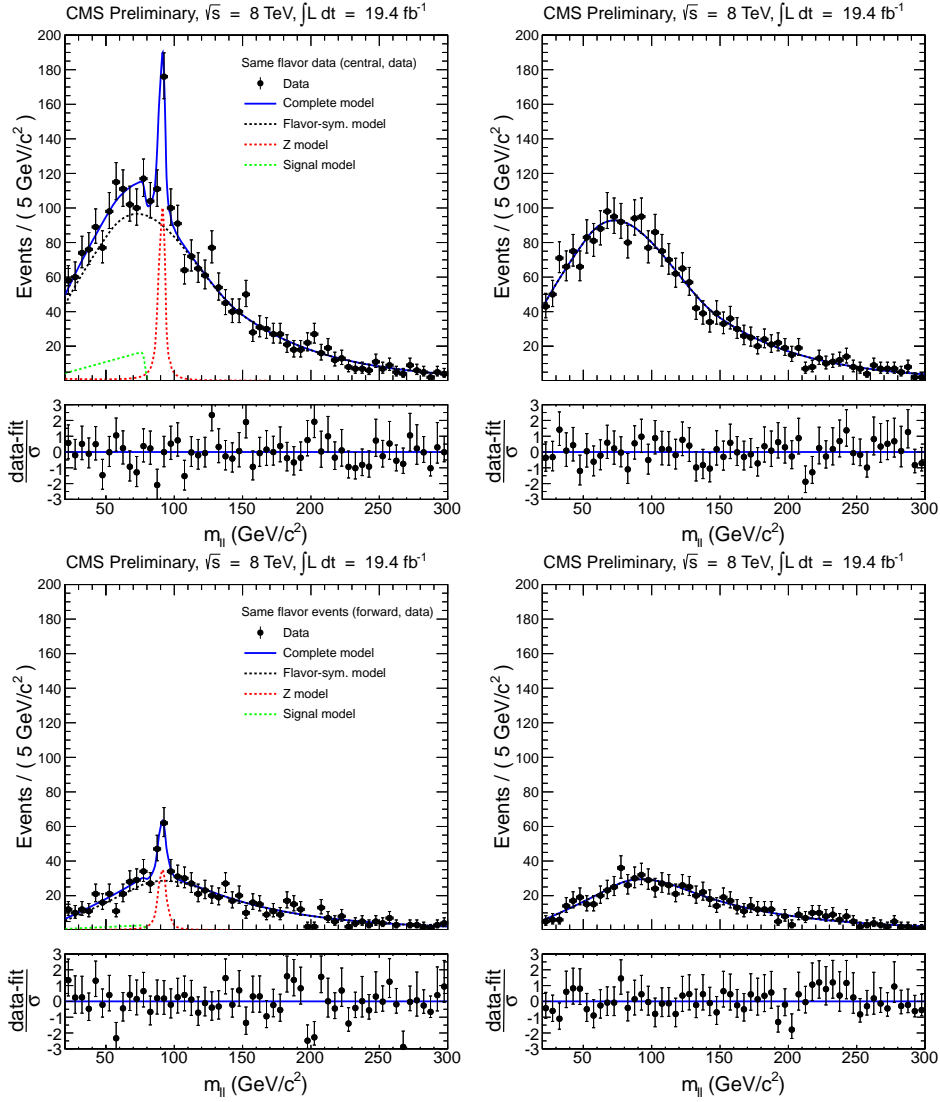


Figure 5.43: Result of fit in signal region for same-flavor (left) and opposite-flavor (right) events for **data** evaluating the **signal hypothesis** in the central (top) and forward region (bottom).

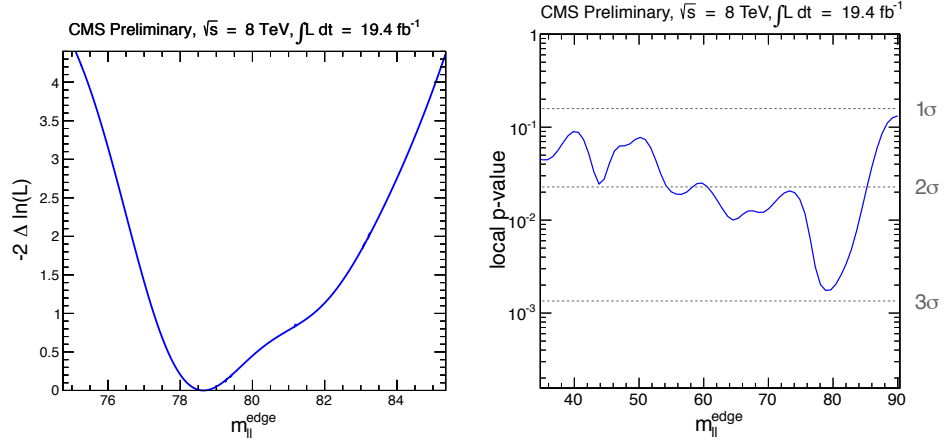


Figure 5.44: Scan of negative log likelihood of signal hypothesis compared to best fitted value $\hat{m}_{\ell\ell}^{\text{edge}}$ in the central region as a function of the edge position $m_{\ell\ell}^{\text{edge}}$ (left) and scan of the p-value (right).

5.6 Interpretation

The fit results from Sec. 5.5 were used to compute 95% confidence level upper limits on the signal yields for the central and forward selection. The limits were computed following the Higgs analysis limit setting procedure adhered to by CMS and ATLAS [121] using a modified frequentist criterion CL_s [122, 123]. The method is briefly summarized in Sec. 5.6.1 and applied to the results in Sec. 5.6.2.

5.6.1 Limit Setting Procedure

The method starts by considering a generic signal yield s and a generic background yield b , which can either be just one bin (as in a counting experiment), multiple bins, or unbinned probability density functions (as in a fit). A signal strength modifier μ is introduced to change the cross-section of a given signal (while the branching ratios remain invariant).

Both the prediction of the background and the signal have uncertainties which are handled by nuisance parameters θ (with default values $\tilde{\theta}$). The background and signal expectations therefore become dependent on θ , $s(\theta)$ and $b(\theta)$. Sources of uncertainty are either taken to be 100% correlated (or anti-correlated) or fully uncorrelated; partially uncorrelated uncertainties are either decomposed into fully correlated components and fully independent components, or declared fully (un)correlated.

The likelihood function $\mathcal{L}(\text{data}|\mu, \theta)$ can then be constructed as

$$\mathcal{L}(\text{data}|\mu, \theta) = \text{Poisson}(\text{data}|\mu \cdot s(\theta) + b(\theta)) \cdot p(\theta), \quad (5.23)$$

where “data” is either actual experimental observation or pseudo-data to construct sampling distributions, and $p(\theta)$ is the probability density function (PDF) associated with the systematic uncertainties. The expression $\text{Poisson}(\text{data}|\mu s + b)$ either stands for a product of Poisson probabilities (in the case of a counting experiment with one or multiple bins) or, as in the present case, for an unbinned likelihood over k events in the data sample,

$$k^{-1} \prod_i (\mu S f_s(x_i) + B f_b(x_i)) \cdot e^{-(\mu S + B)}, \quad (5.24)$$

where $f_s(x_i)$ and $f_b(x_i)$ are PDFs of signal and background, respectively, of an observable x , and S (B) is the total expected event rate for signal (background).

The test statistic \tilde{q}_μ [124] is constructed based on the profile likelihood ratio,

$$\tilde{q}_\mu = -2 \ln \left(\frac{\mathcal{L}(\text{data}|\mu, \hat{\theta}_\mu)}{\mathcal{L}(\text{data}|\hat{\mu}, \hat{\theta})} \right), \quad \text{with a constraint } 0 \leq \hat{\mu} \leq \mu. \quad (5.25)$$

The likelihood in the numerator is maximized while keeping μ constant, therefore only optimizing the nuisance parameters; the value of the nuisance parameters at the maximum for the numerator are denoted $\hat{\theta}_\mu$. On the other hand, the signal strength modifier μ is not kept constant when maximizing the likelihood in the denominator; the values at the global maximum are denoted $\hat{\mu}$ and $\hat{\theta}$. The final yield is required to be positive definite, imposing a constraint on μ , i.e. $\mu \geq 0$; furthermore, an upper bound is imposed to obtain a one-sided confidence interval.

Next, the observed value of the test statistic \tilde{q}_μ^{obs} for the given signal strength modifier μ is determined, and the nuisance parameters $\hat{\theta}_0^{obs}$ (for the background-only hypothesis) and $\hat{\theta}_\mu^{obs}$ (for the background-and-signal hypothesis) best describing the data are established.

Toy Monte Carlo pseudo-data is generated to construct the probability density functions $f(\tilde{q}_\mu|\mu, \hat{\theta}_\mu^{obs})$ and $f(\tilde{q}_\mu|0, \hat{\theta}_0^{obs})$, assuming $\mu = 0$ for the background-only hypothesis (H_0), and a signal strength μ in the background-and-signal hypothesis (H_1). The PDFs make it possible to define the p-values with the actual observation

for the two hypotheses,

$$\begin{aligned}
p_\mu &= P(\tilde{q}_\mu \geq \tilde{q}_\mu^{obs} | \text{signal+background}) = \int_{\tilde{q}_\mu^{obs}}^{\infty} d\tilde{q}_\mu f(\tilde{q}_\mu | \mu, \tilde{\theta}_\mu^{obs}) \equiv \text{CL}_{s+b}(\mu) \\
1 - p_b &= P(\tilde{q}_\mu \geq \tilde{q}_\mu^{obs} | \text{background}) = \int_{\tilde{q}_0^{obs}}^{\infty} d\tilde{q}_\mu f(\tilde{q}_\mu | \mu = 0, \tilde{\theta}_0^{obs}) \equiv \text{CL}_b(\mu) .
\end{aligned}
\tag{5.26}$$

The p -value for the background-and-signal hypothesis is given by $p_\mu = \text{CL}_{s+b}$, and the p -value for the background-only hypothesis is given by $p_b = 1 - \text{CL}_b$; the latter represents the probability of a background leading to a distribution at least as signal-like as the one observed. The CL_s quantity is then defined as the ratio of the two confidence levels,

$$\text{CL}_s(\mu) = \frac{\text{CL}_{s+b}(\mu)}{\text{CL}_b(\mu)} . \tag{5.27}$$

A signal hypothesis is excluded at $(1-\alpha)$ confidence level if $\text{CL}_s(\mu = 1) < \alpha$. To compute $(1 - \alpha)$ confidence level upper limits on μ , the signal strength modifier is adjusted until $\text{CL}_s = \alpha$ is reached (the corresponding signal strength modifier is denoted $\mu^{1-\alpha}$).

To obtain expected limits, a large set of background-only pseudo-data is generated and $\mu^{1-\alpha}$ (in the present case, $\mu^{95\%}$) is calculated for each of them. A cumulative probability distribution can then be constructed based on the results obtained from the set of pseudo-datasets; the median is located at the point where the distribution reaches the 50% quantile, and the 1σ (and 2σ) bands can be determined similarly by finding the point at which the distribution attains the 16% and 84% quantiles (2.5% and 97.5% quantiles for $\pm 2\sigma$).

5.6.2 Limit Calculation Results

The fit results detailed in Sec. 5.5 are used to compute 95% confidence level upper limits on the signal yields N_S for the central and forward selection. The signal yields are left floating in the fit, but are constrained to positive values (since SUSY signals are not expected to interfere with SM backgrounds).

Upper limits are derived according to the procedure laid out in Sec. 5.6.1 for each mass hypothesis in $[50, 300]$ GeV. The observed and expected limits (computed based on approximately 8000 toy MC pseudo-datasets) are shown, along with $\pm 1\sigma$ and $\pm 2\sigma$ bands.

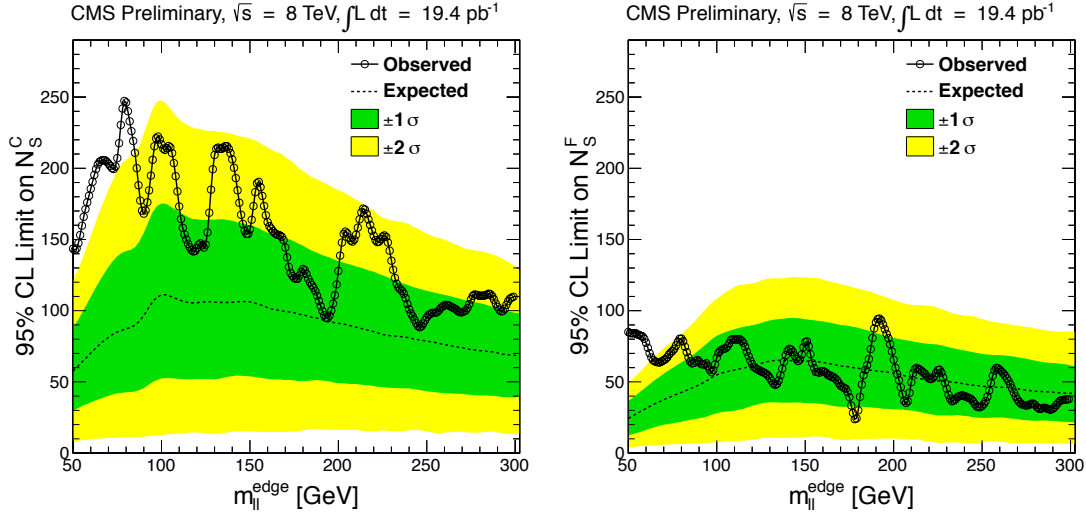


Figure 5.45: Observed and expected 95% confidence level upper limit on the signal yield as a function of the edge position for the central selection (left) and the forward selection (right). The 1σ band (green) and 2σ (yellow) band are also shown.

The upper limits are shown in Fig. 5.45 for the central (left) and forward (right) selection, as a function of the mass edge position $m_{\ell\ell}^{\text{edge}}$. The observed 95% confidence level upper limits vary between 90 and 250 for the central selection and 25 and 95 for the forward selection.

6

Summary and Conclusions

The LHC has pushed the high energy frontier well into the TeV range and will go even further in 2015 with a center-of-mass energy of 13-14 TeV. The physics programs at the LHC have been very successful in confirming various aspects of the Standard Model and completing its predicted particle spectrum with the discovery of the Higgs boson in 2012.

However, the Standard Model is not the ultimate answer; its shortcomings include a lack of dark matter candidates, parameter fine-tuning due to the mass of the Higgs particle, and non-inclusion of gravity, among others. The Standard Model can therefore only be a low energy approximation to a more fundamental theory. One proposed extension to the Standard Model consists of adding another symmetry to the model (the so-called “supersymmetry”), which leads to a supersymmetric partner for each Standard Model particle. This extension does not only provide a dark matter candidate, but it also resolves other open issues of the Standard Model, making it a particularly attractive candidate. The search for physics beyond the Standard Model is one of the core purposes of the Compact Muon Solenoid (CMS) detector at the Large Hadron Collider (LHC).

In this work, a search for physics beyond the Standard Model in the opposite-sign same-flavor dilepton final state has been presented, using a dataset of 19.4 fb^{-1} collected by the CMS detector. The search relied on two different approaches: a

counting experiment in the low invariant dilepton mass range was used to detect a generic signal in the same-flavor final state, whereas a fit to the dilepton mass spectrum was used to search for a kinematic edge (which is a typical feature of cascade decays with two correlated leptons originating from the same cascade).

The definition of signal and control regions was based on general considerations of processes beyond the Standard Model: events from such processes are expected to feature a large transverse momentum imbalance due to undetectable particles, and the new particles are expected to be very massive.

The main backgrounds were estimated using multiple methods (based on data control samples) for each background.

The dominating background stems from processes producing electrons and muons with equal probability, therefore leading to a flavor symmetric background, which was exploited by using the opposite-flavor control sample and deriving a transfer factor based on the combination of two independent methods: in one approach, the transfer factor was estimated in a signal-region-adjacent control region, and in the other the transfer factor was factorized using an alternative parametrization, with the first parameter being measured in a high statistics Drell-Yan enriched control region and the second in a data sample collected with independent triggers. The uncertainty on the combined estimate has been found to be 5% for the central region and 11% for the forward region, and very good agreement has been found in tests using Monte Carlo simulation.

The contribution from the Drell-Yan process is more than an order of magnitude less dominant in the low-mass region, and was also estimated based on the combination of two independent methods; one approach utilized the symmetry of the JZB variable for $Z + \text{jets}$ events, whereas the other made use of a similar final state to predict the $Z + \text{jets}$ background. Both $Z + \text{jets}$ prediction methods lead to a $Z + \text{jets}$ estimate in the Z window, which was related to the low mass region using extrapolation factors. The method was tested using Monte Carlo samples, where very good agreement was found.

Backgrounds with non-prompt leptons were also studied using an array of different methods, including the tight-to-loose method as well as same-sign events; the background from non-prompt leptons was found to be negligible.

Residual rare backgrounds have been assessed as well and lead to a contribution at the per mille level.

The kinematic edge search goes beyond the counting experiment in looking for a specific signal stemming from correlated leptons in a cascade decay. The edge search made use of the transfer factor and the Drell-Yan estimate of the counting

experiment, and used shapes to describe the backgrounds. While the counting experiment is advantageous to detect a generic signal, the edge search reveals more information about a given model by detecting the kinematic edge position characterizing the mass hierarchy of the particles involved in the cascade decay.

The estimates for the counting experiment were compared to the observed yields. While 733 ± 40 events were expected in the central region (and 157 ± 16 events in the forward region), a total of 860 events (163) events were observed, corresponding to a 2.5σ excess (0.2σ in the forward signal region). The search for a kinematic edge found a 2.96σ excess for an edge position at 78.7 ± 1.4 GeV. The present dataset does not permit to make any claims other than that an excess is observed. The results have been used to establish 95% confidence level upper limits on the event yields using a modified frequentist criterion CL_s . The expected limits on the signal yield vary between 60 and 110 (25 and 65) events for the central (forward) region, while the observed limits are between 90 and 250 (25 and 95) events for the central (forward) region.

Outlook

New physics was believed to be in reach of the high center-of-mass energy of the LHC but has turned out to be more elusive than anticipated. The search programs have excluded a broad range of candidate models and with the new data taking (after the long shutdown) on the horizon, the sensitivity frontier will advance even further, benefiting from the increase in cross-section due to the higher center-of-mass energy. If the 2.5σ excess in the present analysis is due to a new physics process, it should certainly show up in the new data, and will benefit from the increase in the center-of-mass energy. Assuming similar signal and control region acceptance and scaling the yields according to the top pair production cross-section to 14 TeV (and the excess according to the benchmark), a 3.6σ excess would already appear after 5 fb^{-1} of 14 TeV data, and 10 fb^{-1} would be sufficient to reach 5.0σ . With the present dataset, however, the observed excess is compatible with a statistical fluctuation.

List of Figures

2.1	One-loop quantum corrections to the Higgs squared mass parameter m_H^2 , due to (a) a Dirac fermion f , and (b) a scalar S . [11]	7
2.2	Evolution of the inverse gauge couplings α_i^{-1} as a function of the energy [11], computed in the Standard Model (dashed lines) and the MSSM case (red and blue lines); in the case of the MSSM, the sparticle masses were varied between 500 GeV and 1.5 TeV, and $\alpha_3(m_Z)$ is varied between 0.117 and 0.121. While the gauge couplings do not meet in the Standard Model, the unification is possible in the MSSM at very high energies.	11
2.3	LHC cross-sections [34] for sparticle production at $\sqrt{s} = 8$ TeV, calculated at next-to-leading order (NLO) by PROSPINO [35].	13
2.4	Lepton pair production in the decay of an $\tilde{\chi}_2^0$ into an $\tilde{\chi}_1^0$ via an on-shell Z boson or virtual Z/ γ^* boson (left) or via a slepton (right).	14
2.5	Particle mass spectrum and decay chains in the pMSSM benchmark point described by the parameter values summarized in Tab. 2.5. . .	17
2.6	Dilepton invariant mass distribution for the pMSSM benchmark point described by the parameters summarized in Tab. 2.5. A clear kinematic edge can be seen at the expected endpoint of 62.4 GeV.	18
3.1	Accelerator Complex at CERN [51].	21

3.2	Layout of the CMS detector: silicon tracker (a), crystal electromagnetic calorimeter (b), preshower (c), hadron calorimeter (d), superconducting solenoid (e), muon chambers (f), steel return yoke (g), and forward calorimeter (h) [57].	23
3.3	One quarter cross-sectional view of the CMS experiment with lines of constant pseudorapidity (η) superimposed and some dimensions (in mm) [56].	24
3.4	Schematic cross-section of the tracker, with each line representing a tracker module [6].	25
3.5	Layout of the electromagnetic calorimeter, indicating the arrangement of crystal modules, supermodules and endcaps, with the preshower in front [6].	26
3.6	Labeled layout of the muon system with lines of constant pseudorapidity [56].	29
4.1	Event display of a simple hadronic jet; dots represent cluster positions, dashed lines indicate simulated particles, and open markers stand for the position of their impact on the calorimeter surfaces [63].	34
4.2	Total jet energy correction factor, as a function of the pseudorapidity for two different p_T values. The bands indicate the corresponding uncertainty [74].	41
4.3	Total jet energy correction factor, as a function of the transverse momentum for two different η values. The bands indicate the corresponding uncertainty [74].	41
4.4	Total jet energy scale uncertainty as a function of the transverse momentum for two different η values [74].	42
4.5	Resolution of the particle-flow E_T^{miss} projection along the x axis (left) and y axis (right) as a function of $\sum E_T$ for events with a Z and a γ (blue circles represent $Z \rightarrow \mu^+ \mu^-$ events, red circles stand for $Z \rightarrow e^+ e^-$ events, and full green squares illustrate photon events). The response in data is shown in the top frame whereas the ratio between data and Monte Carlo simulation is shown in the bottom frame [86].	43
4.6	Mean number of interactions per bunch crossing [88].	44
4.7	Contributions entering the particle isolation calculation, including the average energy density ρ , shown as a function of the number of reconstructed primary vertices (left); the isolation with and without the effective area correction are also shown (right) [93].	47
5.1	Cumulative luminosity delivered (blue) to and recorded (orange) by CMS during stable beams, as a function of time [88].	53

5.2	Peak luminosity per day recorded by CMS during stable beams, as a function of time; the different data taking periods are visible: the first ranges from early to mid-April (2012A), the second from early May to mid-June (2012B), the third from July 1 to mid-September (2012C), and the last from late September to late December (2012D) [88].	53
5.3	Opposite-sign same-flavor (left) and opposite-sign opposite-flavor (right) dilepton mass distributions in data and Monte Carlo simulation, in events with ≥ 3 jets. The bottom plots show the ratio between data and Monte Carlo simulation, and the orange band represents the systematic uncertainty from Jet Energy Scale calibration, pile-up re-weighting, and the $t\bar{t}$ cross-section.	55
5.4	Jet multiplicity (left) and $E_{\text{T}}^{\text{miss}}$ (right) shape (normalized to unit area) in opposite-sign same-flavor dilepton events (without any jet multiplicity or $E_{\text{T}}^{\text{miss}}$ requirement) for the dominant backgrounds and a SUSY benchmark point; the Standard Model processes tend to have lower jet multiplicity and lower $E_{\text{T}}^{\text{miss}}$ than the SUSY benchmark model.	56
5.5	Illustration of the signal and control regions used in the analysis, with the signal region (green) occupying the region at high $E_{\text{T}}^{\text{miss}}$ and high jet multiplicity, the adjacent main control region (blue) having reduced jet multiplicity and $E_{\text{T}}^{\text{miss}}$, and the DY-enriched control region (orange) at low $E_{\text{T}}^{\text{miss}}$	58
5.6	Stability of $R(\text{SF}/\text{OF})$ with respect to $r_{\mu e}$. The effect of a 5% uncertainty on R_{T} is also shown.	62
5.7	Measured values of $R(\text{SF}/\text{OF})$ (top), $R(ee/\text{OF})$ (middle), and $R(\mu\mu/\text{OF})$ (bottom) in data and $t\bar{t}$ MC simulation in the control region, as a function of the dilepton invariant mass. The left plots correspond to the central region; the right plots correspond to the forward region.	65
5.8	$r_{\mu e}$ values in a mix of MC simulated samples (consisting of $t\bar{t}$ and DY + jets) as a function of the invariant mass, for the central (left) and forward (right) selection. The red points represent the values obtained in the signal region selection (without a cut on $m_{\ell\ell}$), whereas the blue points correspond to the DY-enriched control region (without the $m_{\ell\ell}$ requirement) in which $r_{\mu e}$ is measured. The green band is centered at the $r_{\mu e}$ value obtained in the DY-enriched control region in the mass range $60 < m_{\ell\ell} < 120$ GeV (black box), the width of the band corresponds to the 10% (20%) uncertainty for the central (forward) selection.	67

5.9	SF and OF yields as a function of $m_{\ell\ell}$ for $Z \rightarrow \tau\tau$ events, and the corresponding $R(\text{SF}/\text{OF})$ value, for events with $N_{\text{jets}} \geq 2$ and $E_{\text{T}}^{\text{miss}} > 50$ GeV.	71
5.10	Comparison of the dilepton mass of the uncorrelated lepton pair in WZ MC (left), a mixture of all MC samples (right).	73
5.11	Comparison of the dilepton mass of the uncorrelated lepton pair in data.	74
5.12	Data/MC comparison of the dilepton mass of the uncorrelated lepton pair for SF (left) and OF events (right)	74
5.13	Response measured in data (left) and Monte Carlo simulation (right). The points show the profile of the 2D histogram. The red curve shows the result of a flat line fit to the $[100,400]$ GeV region.	77
5.14	JZB distribution for several ranges in p_{T} of the Z boson candidate before the response correction (left) and after the response correction (right); the correction recovers the p_{T} invariance of the JZB peak position.	77
5.15	JZB distributions for a selection with at least three jets; one selection contains at least three jets from the hard collision (green) whereas the second contains less than three jets from the hard collision (red); events with less than three jets from the hard collision may still enter the selection due to additional jets present in the events. A clear shift between the distributions is visible.	78
5.16	Peak position of the JZB distribution as a function of the number of vertices in the event, in data (left) and Monte Carlo simulation (right).	78
5.17	Fit to the response and pile-up corrected JZB distribution for data (left) and Monte Carlo simulated samples (right) to extract the peak correction.	79
5.18	Illustration of the correlation between the raw JZB variable and $E_{\text{T}}^{\text{miss}}$: the raw JZB variable is bounded from above and below by $E_{\text{T}}^{\text{miss}}$	81
5.19	Illustration of the procedure to derive a Z prediction as a function of $E_{\text{T}}^{\text{miss}}$ using the JZB variable: the JZB variable permits an even division of events into two subsamples ("observed" sample and "prediction" sample) due to the symmetry of the JZB distribution. The "prediction" sample can then be used to derive an estimate of the Z content of the "observed" sample.	82

5.20	Comparisons of predicted and observed E_T^{miss} distribution in a sample of simulated Drell-Yan events for different values of the modification parameter λ : the different cases shown are $\lambda = -2$ (top left), $\lambda = -1$ (top right), $\lambda = 0$ (bottom left), and $\lambda = +1$ (bottom right). The best value is found to be $\lambda = -1$	84
5.21	Observed and predicted E_T^{miss} distribution in a sample of simulated Drell-Yan events, for events with two jets (left) and three jets (right).	85
5.22	Observed and predicted E_T^{miss} distribution in a full mix of Monte Carlo samples for events with two jets (left) and three jets (right).	86
5.23	Observed and predicted E_T^{miss} distribution in data for events with two jets (left) and three jets (right).	86
5.24	$m_{\ell\ell}$ distribution in SF events with at least 2 jets and $E_T^{\text{miss}} < 50$ GeV, after the central (left) and forward (right) lepton selections in data . The top, middle, and bottom plots show the e^+e^- , $\mu^+\mu^-$, and combined distributions. The corresponding opposite-flavor distribution is shown in red. The boundaries of the Z peak ($81 < m_{\ell\ell} < 101$ GeV) and signal ($20 < m_{\ell\ell} < 70$ GeV) mass regions are also shown.	89
5.25	$m_{\ell\ell}$ distribution in SF events with at least 2 jets and $E_T^{\text{miss}} < 50$ GeV, after the central (left) and forward (right) lepton selections in MC simulation . The top, middle, and bottom plots show the e^+e^- , $\mu^+\mu^-$, and combined distributions. The corresponding opposite-flavor distribution is shown in red. The boundaries of the Z peak ($81 < m_{\ell\ell} < 101$ GeV) and signal ($20 < m_{\ell\ell} < 70$ GeV) mass regions are also shown.	90
5.26	Shape comparison of the dilepton mass DY MC, for 2-jet events with $E_T^{\text{miss}} < 50$ GeV and 3-jet events with $E_T^{\text{miss}} > 50$ GeV.	91
5.27	Variation of the $R_{\text{in/out}}$ ratio as a function of E_T^{miss} requirement in data (top) and MC simulation (bottom), after the central (left) and forward (right) lepton selections.	92
5.28	Variation of the $R_{\text{in/out}}$ ratio as a function of the number of jets requirement in data (top) and MC simulation (bottom), after the central (left) and forward (right) lepton selections. The last jet multiplicity bin also includes all higher multiplicities.	93
5.29	Comparison of the $m_{\ell\ell}$ distributions in data and MC simulation after the central (left) and forward (right) lepton selections.	94

5.30	Same-flavor and opposite-flavor yields as a function of $m_{\ell\ell}$ for a sample of simulated $W + \text{jets}$ and $t\bar{t}$ events (1 prompt lepton + 1 fake lepton) with at least one of the reconstructed leptons to be matched to a generated non-prompt lepton (e.g., $B \rightarrow \ell\nu X$) or a fake lepton coming from mis-identification of hadrons (e.g., π^0 , ρ , $\pi^\pm K^\pm$); for the central signal region (left) and the forward signal region (right).	98
5.31	SF and OF yields as a function of $m_{\ell\ell}$ for $t\bar{t}$ (1 prompt lepton + 1 fake lepton) process reconstructed in the dilepton final state with at least one of the reconstructed leptons to be matched to a generated non-prompt lepton (e.g., $B \rightarrow \ell\nu X$) or a fake lepton coming from mis-identification of hadrons (e.g., π^0 , ρ , $\pi^\pm K^\pm$); for the central signal region (left) and the forward signal region (right).	99
5.32	Relative importance of the different background estimates: the flavor symmetric estimate ("FSE") is the most dominant contribution, followed by the Drell-Yan estimate ("DY") contributing at the 1% level, and rare backgrounds ("rare") contributing approximately 3 times less. Backgrounds from non-prompt leptons are not shown since they have been determined to be negligible.	103
5.33	Fit of the flavor symmetric shape to the opposite-flavor sample in Monte Carlo simulated samples for the central (left) and forward (right) region.	105
5.34	Fitted shape for backgrounds containing a Z for di-electron events (left) and di-muon events (right) for the central (top) and forward regions (bottom). The fitted shape consists of an exponential (green) and a peak model (red), the sum (blue) of which describes the backgrounds containing a Z . In the ratio plot, the blue line is located at 1.0, whereas a variation by 10% is indicated by the green lines and a variation by 20% by the yellow lines.	108
5.35	Illustration of the signal model (green) using a pMSSM point (described in Sec. 2.4.1); note that a small flavor symmetric contribution (black) also exists, while the Z model is not visible in this illustration.	109
5.36	Result of fit in signal region for same-flavor (left) and opposite-flavor (right) events in the central (top) and forward (bottom) region for Monte Carlo simulation without injected signal evaluating the null hypothesis	118
5.37	Result of fit in signal region for same-flavor (left) and opposite-flavor (right) events in the central (top) and forward (bottom) region for Monte Carlo simulation without injected signal evaluating the signal hypothesis	119

5.38	Result of fit in signal region for same-flavor (left) and opposite-flavor (right) events in the central (top) and forward (bottom) region for Monte Carlo simulation with an injected signal evaluating the null hypothesis	120
5.39	Result of fit in signal region for same-flavor (left) and opposite-flavor (right) events in the central (top) and forward (bottom) region for Monte Carlo simulation with an injected signal evaluating the signal hypothesis	121
5.40	Scan of the log likelihood as a function of the edge position $m_{\ell\ell}^{edge}$ in Monte Carlo simulation without (left) and with (right) an injected signal. The true edge position is at 62.4 GeV, the reconstructed edge position is at 62.3 ± 0.6 GeV.	122
5.41	Comparison between the estimated and observed mass distributions in the central (left) and forward (right) signal regions. The blue band shows the total uncertainty on the background estimate. The bottom plots show the ratio between estimated and observed distributions. The uncertainties on the data points are statistical only, and the systematic uncertainty is indicated as an orange band.	123
5.42	Result of fit in signal region for same-flavor (left) and opposite-flavor (right) events for data evaluating the null hypothesis in the central (top) and forward region (bottom).	126
5.43	Result of fit in signal region for same-flavor (left) and opposite-flavor (right) events for data evaluating the signal hypothesis in the central (top) and forward region (bottom).	127
5.44	Scan of negative log likelihood of signal hypothesis compared to best fitted value \hat{m}_{ll}^{edge} in the central region as a function of the edge position $m_{\ell\ell}^{edge}$ (left) and scan of the p-value (right).	128
5.45	Observed and expected 95% confidence level upper limit on the signal yield as a function of the edge position for the central selection (left) and the forward selection (right). The 1σ band (green) and 2σ (yellow) band are also shown.	131

List of Tables

2.1	Electric charges (in units of e) and masses (in MeV) of the fermions [7].	4
2.2	Electric charges (in units of e) and masses of the gauge bosons [7].	5
2.3	Standard Model particles and their supersymmetric partners in the minimal supersymmetric Standard Model (MSSM).	9
2.4	Supersymmetric particles in the MSSM: gauge eigenstates (left) mix to give experimentally measurable mass eigenstates (right). . .	9
2.5	Parameter values of pMSSM benchmark point.	16
3.1	Design and actual (2012) parameters of the LHC; the integrated luminosity is the one delivered to CMS and ATLAS.	22
5.1	Summary of object definitions and selections for the search and control regions (for a more detailed description of the different objects see Chap. 4).	51
5.2	Triggers used in the analysis (top) and for control samples (bottom), including their thresholds.	52
5.3	SM background yields expected for 19.4fb^{-1} from MC simulation after the event selection.	60
5.4	Measured values of ratios relating the transfer factor in the signal region to the transfer factor in the control region, using $t\bar{t}$ MC simulation; the values are indicated for the central (top) and forward (bottom) selection.	64
5.5	Summary table for the central control region and $m_{\ell\ell} \in [20, 70]\text{GeV}$.	66

5.6	Summary table for the forward control region and $m_{\ell\ell} \in [20, 70]$ GeV.	66
5.7	Measured values of the parameters of the alternative parametrization ($r_{\mu e}$, trigger efficiencies, R_T), and final values. The letters in brackets indicate the control sample(s) used for the measurements.	68
5.8	Transfer factors obtained for the central and forward regions by the two methods and their combination using a weighted average. The measured $r_{\mu e}$ and R_T values are also given.	69
5.9	Estimate of the flavor symmetric background yields in the signal regions. The top row shows the raw OF yields, the following rows show the estimates after correcting the raw yield with the appropriate transfer factor.	70
5.10	Number of SF and OF events in a WZ Monte Carlo sample and a subsample containing only correct combinations (i.e. first lepton from Z).	72
5.11	Typical values for the different corrections of the JZB distribution for data and Monte Carlo simulation.	80
5.12	Estimate of the Z background yields in the Z peak region and extrapolation to the signal mass region for the full dataset.	95
5.13	Number of events with fake dileptons in $W + \text{jets}$ ($W + \text{heavy flavor}$ included) and $t\bar{t}$ processes, after lepton preselection (no jets and E_T^{miss} cuts) and signal region selection, for 9.2 fb^{-1} .	97
5.14	Number of events passing the tight-tight, tight-loose, and loose-loose selections in the central and forward regions, and total fake estimates for different flavors including statistical uncertainty (first) and 50% systematic uncertainty.	100
5.15	Number of events with same sign leptons in the two signal regions.	101
5.16	Total expected yields in the central and forward region. The uncertainties in the prediction of the individual processes are statistical only while a 50% systematic uncertainty is applied to the total prediction. A factor of 0.5 is used to split between ee and $\mu\mu$. Differences in the factor are well covered by the 50% uncertainty.	102
5.17	Event yields estimated in the signal regions; statistical and systematic uncertainties are shown for the dominant flavor symmetric background; the uncertainties are added in quadrature for the subdominant backgrounds.	104

5.18	Overview of all floating parameters in the full fit in the signal region, including their status, initial value and parameter range. Note that the parameters pertaining to the Drell-Yan shape (summarized in Tab. 5.19) are fixed and that each parameter exists once for each region with the notable exception of $m_{\ell\ell}^{edge}$	113
5.19	Overview of all floating parameters in the fit in the Drell-Yan enriched control region, including their status, initial value and parameter range; each parameter is defined (and fitted) separately for the central and forward region.	114
5.20	Use of floating parameters for the different components; parameters used for the normalization are marked with an "n", parameters used for the shape are ticked ($\sqrt{}$). Note that parameters in \vec{p}_Z^i are frozen in the fit in the signal region.	115
5.21	Event yields measured and estimated in the signal regions. Significances are calculated using the profile likelihood method [121]. Statistical and systematic uncertainties on the sub-dominant backgrounds are added in quadrature.	124
5.22	Integrated yields of the different model components resulting from the unbinned maximum likelihood fit.	125
5.23	Integrated yields of the different model components of the unbinned maximum likelihood fit; the integration is restricted to the low-mass signal region to allow for a comparison with the estimates from the counting experiment listed in Tab. 5.21.	125

References

- [1] CMS Collaboration, “Observation of a new boson at a mass of 125 GeV with the CMS experiment at the LHC”, *Phys. Lett. B* **716** (2012), no. 1, 30 – 61, doi:10.1016/j.physletb.2012.08.021.
- [2] ATLAS Collaboration, “Observation of a new particle in the search for the Standard Model Higgs boson with the ATLAS detector at the LHC”, *Phys. Lett. B* **716** (2012), no. 1, 1 – 29, doi:10.1016/j.physletb.2012.08.020.
- [3] G. Bertone, “Particle Dark Matter: Observations, Models and Searches”. Cambridge University Press, 2010.
- [4] D. Cline, “Dark matter in the universe: proceedings of the International Symposium on Sources and Detection of Dark Matter in the Universe : Santa Monica, California, USA, 14-16 February 1996”. Nuclear physics. North-Holland, 1996.
- [5] G. Bertone, D. Hooper, and J. Silk, “Particle Dark Matter: Evidence, Candidates and Constraints”, arXiv:hep-ph/0404175.
- [6] CMS Collaboration, “The CMS experiment at the CERN LHC”, *JINST* **3** (2008) S08004, doi:10.1088/1748-0221/3/08/S08004.
- [7] Particle Data Group Collaboration, “Review of Particle Physics”, *Phys. Rev. D* **86** (2012) 010001, doi:10.1103/PhysRevD.86.010001.

- [8] E. Komatsu, K. Smith, J. Dunkley et al., “Seven-Year Wilkinson Microwave Anisotropy Probe (WMAP) Observations: Cosmological Interpretation”, arXiv:1001.4538.
- [9] C. J. Copi, D. N. Schramm, and M. S. Turner, “Big bang nucleosynthesis and the baryon density of the universe”, *Science* **267** (1995) 192–199, doi:10.1126/science.7809624.
- [10] L. Bergström, “Non-baryonic dark matter: observational evidence and detection methods”, *Reports on Progress in Physics* **63** (2000), no. 5, 793.
- [11] S. P. Matrin, “A Supersymmetry Primer”, arXiv:hep-ph/9709356.
- [12] F. Zwirner, “Observable Delta B=2 Transitions Without Nucleon Decay in a Minimal Supersymmetric Extension of the Standard Model”, *Phys.Lett. B* **132** (1983) 103–106, doi:10.1016/0370-2693(83)90230-7.
- [13] S. Dawson, “R-Parity Breaking in Supersymmetric Theories”, *Nucl.Phys. B* **261** (1985) 297, doi:10.1016/0550-3213(85)90577-2.
- [14] R. Barbieri and A. Masiero, “Supersymmetric Models with Low-Energy Baryon Number Violation”, *Nucl.Phys. B* **267** (1986) 679, doi:10.1016/0550-3213(86)90136-7.
- [15] S. Dimopoulos and L. J. Hall, “Lepton and Baryon Number Violating Collider Signatures from Supersymmetry”, *Phys.Lett. B* **207** (1988) 210, doi:10.1016/0370-2693(88)91418-9.
- [16] V. D. Barger, G. Giudice, and T. Han, “Some New Aspects of Supersymmetry R-Parity Violating Interactions”, *Phys.Rev. D* **40** (1989) 2987, doi:10.1103/PhysRevD.40.2987.
- [17] R. M. Godbole, P. Roy, and X. Tata, “Tau signals of R-parity breaking at LEP-200”, *Nucl.Phys. B* **401** (1993) 67–92, doi:10.1016/0550-3213(93)90298-4.
- [18] G. Bhattacharyya and D. Choudhury, “D and tau decays: Placing new bounds on R-parity violating supersymmetric coupling”, *Mod.Phys.Lett. A* **10** (1995) 1699–1704, doi:10.1142/S0217732395001812.
- [19] H. K. Dreiner, “An Introduction to explicit R-parity violation”, arXiv:hep-ph/9707435.

- [20] G. Bhattacharyya, “R-parity violating supersymmetric Yukawa couplings: A Minireview”, *Nucl.Phys.Proc.Suppl.* **52A** (1997) 83–88, doi:10.1016/S0920-5632(96)00539-7.
- [21] B. Allanach, A. Dedes, and H. Dreiner, “R parity violating minimal supergravity model”, *Phys.Rev.* **D69** (2004) 115002, doi:10.1103/PhysRevD.69.115002.
- [22] M. Chemtob, “Phenomenological constraints on broken R parity symmetry in supersymmetry models”, *Prog.Part.Nucl.Phys.* **54** (2005) 71–191, doi:10.1016/j.ppnp.2004.06.001.
- [23] R. Barbier et al., “R-parity violating supersymmetry”, *Phys.Rept.* **420** (2005) 1–202, doi:10.1016/j.physrep.2005.08.006.
- [24] G. Kane, “Perspectives on Supersymmetry II”. Advanced series on directions in high energy physics. World Scientific, 2010.
- [25] G. L. Kane, C. F. Kolda, L. Roszkowski, and J. D. Wells, “Study of constrained minimal supersymmetry”, *Phys.Rev.* **D49** (1994) 6173–6210, doi:10.1103/PhysRevD.49.6173.
- [26] MSSM Working Group Collaboration, A.Djouadi *et al.* (MSSM Working Group Collaboration), “The Minimal supersymmetric standard model: Group summary report”, 1998.
- [27] CMS Collaboration, “Phenomenological MSSM interpretation of the CMS 2011 5fb^{-1} results”, *CMS-PAS SUS-12-030* (2012).
- [28] CMS Collaboration, “Interpretation of searches for supersymmetry with simplified models”, *Phys. Rev. D* **88** (2013) 052017, doi:10.1103/PhysRevD.88.052017.
- [29] N. Arkani-Hamed et al., “MARMOSSET: The Path from LHC Data to the New Standard Model via On-Shell Effective Theories”, arXiv:hep-ph/0703088.
- [30] J. Alwall, P. C. Schuster, and N. Toro, “Simplified models for a first characterization of new physics at the LHC”, *Phys. Rev. D* **79** (2009) 075020, doi:10.1103/PhysRevD.79.075020.
- [31] J. Alwall, M.-P. Le, M. Lisanti, and J. G. Wacker, “Model-independent jets plus missing energy searches”, *Phys. Rev. D* **79** (2009) 015005, doi:10.1103/PhysRevD.79.015005.

- [32] D. Alves, E. Izaguirre, and J. Wacker, “Where the sidewalk ends: jets and missing energy search strategies for the 7 TeV LHC”, *JHEP* **2011** (2011), no. 10, 1–36, doi:10.1007/JHEP10(2011)012.
- [33] D. Alves et al., “Simplified models for LHC new physics searches”, *J. Phys. G* **39** (2012), no. 10, 105005.
- [34] T. Plehn, “PROSPINO2 Webpage”. <http://www.thphys.uni-heidelberg.de/~plehn/index.php?show=prospino>. Accessed: 2014-01-29.
- [35] W. Beenakker, R. Hoepker, and M. Spira, “PROSPINO: A Program for the Production of Supersymmetric Particles in Next-to-leading Order QCD”, arXiv:hep-ph/9611232.
- [36] A. Arbey, M. Battaglia, and F. Mahmoudi, “Implications of LHC Searches on SUSY Particle Spectra: The pMSSM Parameter Space with Neutralino Dark Matter”, *Eur. Phys. J.* **C72** (2012) 1847, doi:10.1140/epjc/s10052-011-1847-3.
- [37] L. Pape, “Reconstruction of sparticle masses from endpoints at LHC”, *CMS Internal Note* **2006/012** (2006).
- [38] Heavy Flavor Averaging Group Collaboration, “Averages of B-Hadron, C-Hadron, and tau-lepton properties as of early 2012”, arXiv:1207.1158.
- [39] M. Misiak et al., “Estimate of $\mathcal{B}(\bar{B} \rightarrow X_s \gamma)$ at $O(\alpha_s^2)$ ”, *Phys. Rev. Lett.* **98** (2007) 022002, doi:10.1103/PhysRevLett.98.022002.
- [40] Joint LEP2 SUSY Working Group, the Aleph, Delphi, L3 and Opal Collaborations, “Combined Results”, <http://lepsusy.web.cern.ch/lepsusy/> (2004).
- [41] G. Belanger, F. Boudjema, A. Pukhov, and A. Semenov, “MicrOMEGAs: A Program for calculating the relic density in the MSSM”, *Comput. Phys. Commun.* **149** (2002) 103–120, doi:10.1016/S0010-4655(02)00596-9.
- [42] G. Belanger, F. Boudjema, A. Pukhov, and A. Semenov, “micrOMEGAs: Version 1.3”, *Comput. Phys. Commun.* **174** (2006) 577–604, doi:10.1016/j.cpc.2005.12.005.
- [43] G. Belanger, F. Boudjema, A. Pukhov, and A. Semenov, “Dark matter direct detection rate in a generic model with micrOMEGAs 2.2”, *Comput. Phys. Commun.* **180** (2009) 747–767, doi:10.1016/j.cpc.2008.11.019.

- [44] S. Kraml et al., “SModelS: a tool for interpreting simplified-model results from the LHC and its application to supersymmetry”, *arXiv:1312.4175*.
- [45] D. Brandt, “Intermediate accelerator physics. Proceedings, CERN Accelerator School, Zeuthen, Germany, September 15–26, 2003”, doi:10.5170/CERN-2006-002.
- [46] O. Brüning et al., “LHC Design Report. 1. The LHC Main Ring”, *CMS-TDR CERN-2004-003-V-1* (2004) doi:10.5170/CERN-2004-003-V-1.
- [47] O. Brüning et al., “LHC Design Report. 2. The LHC infrastructure and general services”, *CMS-TDR CERN-2004-003-V-2* (2004) doi:10.5170/CERN-2004-003-V-2.
- [48] M. Benedikt et al., “LHC Design Report. 3. The LHC injector chain”, *CMS-TDR CERN-2004-002-V-3* (2004) doi:10.5170/CERN-2004-003-V-3.
- [49] L. Evans and P. Bryant, “LHC Machine”, *JINST* 3 (2008), no. 08, S08001.
- [50] S. Myers and E. Picasso, “The Design, construction and commissioning of the CERN Large Electron Positron collider”, *Contemp. Phys.* 31 (1990) 387–403, doi:10.1080/00107519008213789.
- [51] C. Lefèvre, “The CERN accelerator complex”, *CERN PhotoLab CERN-DI-0812015* (2008).
- [52] ATLAS Collaboration, “The ATLAS Experiment at the CERN Large Hadron Collider”, *JINST* 3 (2008), no. 08, S08003.
- [53] LHCb Collaboration, “The LHCb Detector at the LHC”, *JINST* 3 (2008) S08005, doi:10.1088/1748-0221/3/08/S08005.
- [54] ALICE Collaboration, “The ALICE experiment at the CERN LHC”, *JINST* 3 (2008) S08002, doi:10.1088/1748-0221/3/08/S08002.
- [55] CMS Collaboration, “CMS technical design report, volume II: Physics performance”, *J. Phys.* G34 (2007) 995–1579, doi:10.1088/0954-3899/34/6/S01.
- [56] CMS Collaboration, “CMS physics: Technical Design Report Volume 1: Detector Performance and Software”, *CMS-TDR CERN-LHCC-2006-001* (2006).

- [57] CMS Collaboration, "Detector Drawings", *CMS Photos* **CMS-PHO-GEN-2012-002** (2012).
- [58] CMS Collaboration, "Electromagnetic calorimeter calibration with 7 TeV data", *CMS-PAS* **EGM-10-003** (2010).
- [59] CMS Collaboration, "Performance of the CMS Hadron Calorimeter with Cosmic Ray Muons and LHC Beam Data", *JINST* **5** (2010) T03012, doi:10.1088/1748-0221/5/03/T03012.
- [60] CMS Collaboration, "The Compact Muon Solenoid Computing Technical Proposal", *CMS-TDR* **CERN-LHCC-1996-045** (1996).
- [61] CMS Collaboration, "CMS: The computing project. Technical design report", *CMS-TDR* **CERN-LHCC-2005-023** (2005).
- [62] M. Aderholz et al., "Models of networked analysis at regional centres for LHC experiments (MONARC). Phase 2 report", *CERN Preprint* **CERN-LCB-2000-001** (2000).
- [63] CMS Collaboration, "Particle-Flow Event Reconstruction in CMS and Performance for Jets, Taus, and MET", *CMS-PAS* **PFT-09-001** (2009).
- [64] CMS Collaboration, "Commissioning of the Particle-Flow reconstruction in Minimum-Bias and Jet Events from pp Collisions at 7 TeV", *CMS-PAS* **PFT-10-002** (2010).
- [65] CMS Collaboration, "Tracking and Vertexing Results from First Collisions", *CMS-PAS* **TRK-10-001** (2009).
- [66] CMS Collaboration, "Performance of muon identification in pp collisions at $\sqrt{s} = 7$ TeV", *CMS-PAS* **MUO-10-002** (2010).
- [67] CMS Collaboration, "Performance of CMS muon reconstruction in pp collision events at $\sqrt{s} = 7$ TeV", *JINST* **7** (2012) P10002, doi:10.1088/1748-0221/7/10/P10002.
- [68] CMS Collaboration, "The performance of the CMS muon detector in proton-proton collisions at $\sqrt{s} = 7$ TeV at the LHC", *JINST* **8** (2013) P11002, doi:10.1088/1748-0221/8/11/P11002.
- [69] W. Adam, R. Frühwirth, A. Strandlie, and T. Todorov, "Reconstruction of electrons with the Gaussian-sum filter in the CMS tracker at the LHC", *J. Phys. G* **31** (2005), no. 9, doi:10.1088/0954-3899/31/9/N01.

- [70] S. Baffioni et al., “Electron reconstruction in CMS”, *Eur. Phys. J.* **C49** (2007), no. 4, 1099–1116, doi:10.1140/epjc/s10052-006-0175-5.
- [71] CMS Collaboration, “Electron reconstruction and identification at $\sqrt{s} = 7$ TeV”, *CMS-PAS EGM-10-004* (2010).
- [72] CMS Collaboration, “Tau identification in CMS”, *CMS-PAS TAU-11-001* (2011).
- [73] CMS Collaboration, “Study of tau reconstruction algorithms using pp collisions data collected at $\sqrt{s} = 7$ TeV”, *CMS-PAS PFT-10-004* (2010).
- [74] CMS Collaboration, “Determination of Jet Energy Calibration and Transverse Momentum Resolution in CMS”, *JINST* **6** (2011) P11002, doi:10.1088/1748-0221/6/11/P11002.
- [75] M. Cacciari, G. P. Salam, and G. Soyez, “The anti- k_T jet clustering algorithm”, *JHEP* **0804** (2008) 063, doi:10.1088/1126-6708/2008/04/063.
- [76] S. D. Ellis and D. E. Soper, “Successive combination jet algorithm for hadron collisions”, *Phys. Rev.* **D48** (1993) 3160–3166, doi:10.1103/PhysRevD.48.3160.
- [77] Y. L. Dokshitzer, G. Leder, S. Moretti, and B. Webber, “Better jet clustering algorithms”, *JHEP* **9708** (1997) 001, doi:10.1088/1126-6708/1997/08/001.
- [78] M. Cacciari and G. P. Salam, “Dispelling the N^3 myth for the k_T jet-finder”, *Phys. Lett. B* **641** (2006) 57, doi:10.1016/j.physletb.2006.08.037.
- [79] M. Cacciari, G. Salam, and G. Soyez, “FastJet user manual”, 2011, arXiv:1111.6097.
- [80] CMS Collaboration, “Jet Performance in pp Collisions at 7 TeV”, *CMS-PAS JME-10-003* (2010).
- [81] S. Catani, Y. L. Dokshitzer, and B. Webber, “The k_\perp perpendicular clustering algorithm for jets in deep inelastic scattering and hadron collisions”, *Phys. Lett.* **B285** (1992) 291–299, doi:10.1016/0370-2693(92)91467-N.
- [82] S. Catani, Y. Dokshitzer, M. Seymour, and B. Webber, “Longitudinally-invariant k_\perp -clustering algorithms for hadron-hadron collisions”, *Nucl. Phys. B* **406** (1993), no. 12, 187 – 224, doi:10.1016/0550-3213(93)90166-M.

- [83] UA2 Collaboration, "Measurement of Production and Properties of Jets at the CERN anti-p p Collider", *Z. Phys.* **C20** (1983) 117–134, doi:10.1007/BF01573214.
- [84] DØ Collaboration, "Determination of the absolute jet energy scale in the DØ calorimeters", *Nucl. Instrum. Meth.* **A424** (1999) 352–394, doi:10.1016/S0168-9002(98)01368-0.
- [85] CDF Collaboration, "Determination of the jet energy scale at the collider detector at Fermilab", *Nucl. Instrum. Meth.* **A566** (2006) 375–412, doi:10.1016/j.nima.2006.05.269.
- [86] CMS Collaboration, "Performance of Missing Transverse Momentum Reconstruction Algorithms in Proton-Proton Collisions at $\sqrt{s} = 8$ TeV with the CMS Detector", *CMS-PAS JME-12-001* (2012).
- [87] CMS Collaboration, "Missing transverse energy performance of the CMS detector", *JINST* **6** (2011) P09001, doi:10.1088/1748-0221/6/09/P09001.
- [88] CMS Collaboration, "CMS Luminosity Information". <https://twiki.cern.ch/twiki/bin/view/CMSPublic/LumiPublicResults>. Accessed: 2014-03-25.
- [89] CMS Collaboration, "Performance of electron reconstruction and selection with the CMS detector at $\sqrt{s} = 8$ TeV", *CMS-PAS EGM-13-001* (2014).
- [90] M. Cacciari and G. P. Salam, "Pileup subtraction using jet areas", *Phys. Lett.* **B659** (2008) 119–126, doi:10.1016/j.physletb.2007.09.077.
- [91] M. Cacciari, G. P. Salam, and G. Soyez, "The Catchment Area of Jets", *JHEP* **0804** (2008) 005, doi:10.1088/1126-6708/2008/04/005.
- [92] M. Cacciari, G. P. Salam, and G. Soyez, "FastJet User Manual", *Eur.Phys.J.* **C72** (2012) 1896, doi:10.1140/epjc/s10052-012-1896-2.
- [93] CMS Collaboration, "Electron performance with 19.6 fb⁻¹ of data collected at $\sqrt{s} = 8$ TeV with the CMS detector", *CMS-DP DP-2013/003* (2013).
- [94] CMS Collaboration, "Search for neutral Higgs bosons decaying to τ pairs in pp collisions at $\sqrt{s} = 7$ TeV", *Phys.Lett.* **B713** (2012) 68–90, doi:10.1016/j.physletb.2012.05.028.

- [95] CMS Collaboration, "Search for Physics Beyond the Standard Model in opposite-sign same-flavour dilepton events in 8 TeV pp collisions ", *CMS-PAS SUS-12-019* (2014).
- [96] M. - A. Buchmann, P. Martinez, F. Ronga, K. Theofilatos, "Search for Physics Beyond the Standard Model in Opposite-Sign Same-Flavor Dilepton Events in 8TeV pp Collisions", *CMS-AN 2012/231* (2012).
- [97] C. Autermann, D. Böckenhoff, M. Edelhoff, L. Feld, N. Mohr, M. Schall, J.-F. Schulte, D. Sprenger, S. Tenberg, "Opposite sign di-lepton SUSY search at $\sqrt{s} = 8$ TeV using the 2012 dataset", *CMS-AN 2012/200* (2012).
- [98] CMS Collaboration, "CMS Luminosity Based on Pixel Cluster Counting - Summer 2013 Update", *CMS-PAS LUM-13-001* (2013).
- [99] CMS Collaboration, "CMS Luminosity Based on Pixel Cluster Counting - Summer 2012 Update", *CMS-PAS LUM-12-001* (2012).
- [100] CMS Collaboration, "Absolute Calibration of the Luminosity Measurement at CMS: Winter 2012 Update", *CMS-PAS SMP-12-008* (2012).
- [101] CMS Collaboration, "Absolute Calibration of Luminosity Measurement at CMS: Summer 2011 Update", *CMS-PAS EWK-11-001* (2011).
- [102] CMS Collaboration, "Measurement of CMS Luminosity", *CMS-PAS EWK-10-004* (2010).
- [103] J. Alwall, "MadGraph/MadEvent v4: The New Web Generation", *JHEP* **2007** (2007) 028, doi:10.1088/1126-6708/2007/09/028.
- [104] T. Sjostrand, S. Mrenna, and P. Z. Skands, "PYTHIA 6.4 Physics and Manual", *JHEP* **0605** (2006) 026, doi:10.1088/1126-6708/2006/05/026.
- [105] GEANT4 Collaboration, "GEANT4: A Simulation toolkit", *Nucl. Instrum. Meth. A* **506** (2003) 250–303, doi:10.1016/S0168-9002(03)01368-8.
- [106] CMS Collaboration, "Search for new physics in events with opposite-sign leptons, jets, and missing transverse energy in pp collisions at $\sqrt{s} = 7$ TeV", *Phys. Lett. B* **718** (2013), no. 3, 815, doi:10.1016/j.physletb.2012.11.036.
- [107] CMS Collaboration, "Search for physics beyond the standard model in events with a Z boson, jets, and missing transverse energy in pp collisions at $\sqrt{s} = 7$ TeV", *Phys. Lett. B* **716** (2012), no. 2, 260, doi:10.1016/j.physletb.2012.08.026.

- [108] C. Berger et al., “Next-to-Leading Order QCD Predictions for W+3-Jet Distributions at Hadron Colliders”, *Phys. Rev.* **D80** (2009) 074036, doi:10.1103/PhysRevD.80.074036.
- [109] K. Theofilatos, “Supersymmetric particle detection techniques and electromagnetic calorimeter testbeam analysis with the CMS detector”. PhD thesis, National Tech. University of Athens and N.C.S.R. Demokritos, 2009.
- [110] CMS Collaboration, “Search for Physics Beyond the Standard Model in $Z + \text{jets} + E_{\text{T}}^{\text{miss}}$ events at the LHC”, *CMS-PAS SUS-10-010* (2010).
- [111] CMS Collaboration, “Search for Physics Beyond the Standard Model in $Z + \text{jets} + E_{\text{T}}^{\text{miss}}$ events at the LHC”, *CMS-PAS SUS-11-012* (2011).
- [112] CMS Collaboration, “Search for Physics Beyond the Standard Model in $Z + \text{jets} + E_{\text{T}}^{\text{miss}}$ events at the LHC”, *CMS-PAS SUS-11-019* (2011).
- [113] D. Barge et al., “ $E_{\text{T}}^{\text{miss}}$ Templates Results and Additional Cross-checks for the Opposite-sign Same-flavor (“Edge”) Dilepton Analysis”, *CMS-AN* **2012/359** (2012).
- [114] P. Milenovic et al., “Computing the contamination from fakes in leptonic final states”, *CMS-AN* **2010/261** (2010).
- [115] M. Dunser et al., “Search for New Physics in the Same-Sign Di-Lepton Channel at 8 TeV”, *CMS-AN* **2012/199** (2012).
- [116] I. Galon and Y. Shadmi, “Kinematic edges with flavor splitting and mixing”, *Phys. Rev. D* **85** (2012) 015010, doi:10.1103/PhysRevD.85.015010.
- [117] Y. Grossman, M. Martone, and D. J. Robinson, “Kinematic Edges with Flavor Oscillation and Non-Zero Widths”, *JHEP* **1110** (2011) 127, doi:10.1007/JHEP10(2011)127.
- [118] N. Amapane et al., “Measurement of the production and decay of a Higgs boson in the four-lepton final state”, *CMS-AN* **2013/108** (2013).
- [119] N. Mohr, “Search for Supersymmetry in Opposite-sign Dilepton Final States with the CMS Experiment”. PhD thesis, RWTH Aachen, 2011.
- [120] D. Sprenger, “Search for Supersymmetry in Opposite-sign Dilepton Final States with the CMS Experiment”. PhD thesis, RWTH Aachen, 2012.
- [121] ATLAS Collaboration, CMS Collaboration, LHC Higgs Combination Group Collaboration, “Procedure for the LHC Higgs boson search combination in summer 2011”, *CMS-NOTE-2011-005 ATL-PHYS-PUB-2011-11* (2011).

- [122] T. Junk, “Confidence level computation for combining searches with small statistics”, *Nucl. Instrum. Meth.* **A434** (1999) 435–443, doi:10.1016/S0168-9002(99)00498-2.
- [123] A. L. Read, “Presentation of search results: The CL(s) technique”, *J. Phys.* **G28** (2002) 2693–2704, doi:10.1088/0954-3899/28/10/313.
- [124] G. Cowan, K. Cranmer, E. Gross, and O. Vitells, “Asymptotic formulae for likelihood-based tests of new physics”, *Eur. Phys. J.* **C71** (2011) 1554, doi:10.1140/epjc/s10052-011-1554-0.